High resolution simulations of mode-2 internal waves: transport, shoaling, and the influence of rotation

by

David Deepwell

A thesis
presented to the University of Waterloo
in fulfillment of the
thesis requirement for the degree of
Doctor of Philosophy
in
Applied Mathematics

Waterloo, Ontario, Canada, 2018

Examining Committee Membership

The following served on the Examining Committee for this thesis. The decision of the Examining Committee is by majority vote.

Supervisor:	Marek Stastna Professor, Dept. of Applied Mathematics University of Waterloo
Internal Members:	Francis Poulin Associate Professor, Dept. of Applied Mathematics University of Waterloo
	Mohammad Kohandel Associate Professor, Dept. of Applied Mathematics University of Waterloo
Internal-External Member:	Chris Fletcher Associate Professor Dept. of Geography and Environment Management University of Waterloo
External Examiner:	Daniel Bourgault Professor, Institut des sciences de la mer de Rimouski Université du Québec à Rimouski

I hereby declare that I am the sole author of this thesis. This is a true copy of the thesis, including any required final revisions, as accepted by my examiners.

I understand that my thesis may be made electronically available to the public.

Abstract

Internal waves are a universal feature in stratified flows. Of particular interest are Internal Solitary and Solitary-like Waves (ISWs) which may persist for long periods of time and travel great distances. In the ocean, ISWs are energetically dominated by mode-1 waves. The literature on higher modes, the second mode in particular, is less developed than that for the first mode. However, over the last decade multiple observations of the mode-2 ISWs have been made throughout the world's oceans which has lead to a renewed interest in studying the second mode in theoretical and practical applications.

We present high resolution numerical simulations of mode-2 ISWs on a laboratory scale. We have used the pseudo-spectral model SPINS on the high-performance computing cluster SHARCNET. We have added diagnostics (specifically, energy budgets) into this model to help in reporting the accuracy and efficacy of an individual simulation. Laboratory experiments were also completed to make a comparison to particular numerical results.

We are the first to use full three-dimensional numerical domains to study the generation and evolution of mode-2 ISWs in laboratory environments under various conditions. We present results for three specific experiments: the mass transport efficiency of a mode-2 ISW in a variety of stratifications, the adjustment of a mode-2 ISW in a channel influenced by rotation, and the interaction with topography during the propagation of mode-2 ISWs over an isolated ridge.

Specifically, mass transport is primarily impacted by instabilities in the lee side of a mode-2 ISW which act to destroy the trapped core. However, specific stratification and Schmidt numbers are found to exist which can maintain the presence of the trapped core by inhibiting the lee instabilities.

Rotation modifies the ISW into Kelvin waves and Poincaré waves while also creating a highly localized shear instability along the focusing wall. The first has been presented for mode-1 ISWs while the second is novel. The transit of a mode-2 ISW over a ridge is capable of inducting the loss of material from the core of the ISW when the interaction is strong while also inducing cross-boundary layer transport. In general, it appears that it is quite easy to perturb mode-2 ISWs such that their longevity is reduced.

Acknowledgements

Here it is, the culmination of 5 years of work. I would not have made it here without the help of so many.

This work was supported through multiple Ontario Graduate Scholarships (OGS) and Queen Elizabeth II Graduate Scholarships in Science and Technology (QEII-GSST).

Thank you to Magda Carr and Peter Davies for hosting me at the University of Dundee and the University of St Andrews in 2016. This work has been greatly improved by the addition of the laboratory experiments presented within.

To my officemates: Ben Storer, William Xu, Laura Chandler, Lauren Burnett, Xiaolin Bai, Sandhya Harnanan, Robbie Irwin, and Eric Bembenek. You have been such a joy to be around. Discussions with you have been both insightful and silly.

Aaron Coutino, four years of being roommates has gone by fast. Discussions with you have been thought-provoking. And I will not forget Romulus with his cuddly, fury, little pug face.

To those at Radiant City Church, you have nurtured me spiritually while I grew academically. I needed both, and for that I am thankful.

Lastly, thank you to my supervisor Marek Stastna. You have taught me much about research and academia, and have been an excellent mentor. Thank you for 5 great years.

Dedication

To Mom and Dad, love you always

Table of Contents

List of Tables

List of Figures

Nomenclature

Δx	Grid resolution along the x-dimension
Δy	Grid resolution along the y-dimension
Δz	Grid resolution along the z-dimension
ϵ	Viscous dissipation rate
Γ	Numerical energy removal rate
κ	Molecular diffusivity of density
λ_a	Aft mode-2 wavelength
λ_f	Fore mode-2 wavelength
μ	Dynamic viscosity
ν	Kinematic viscosity
Ω	Enstrophy
ϕ_d	Rate of change of BPE
ϕ_i	Energy flux rate from internal energy to BPE
ϕ_m	Mixing flux rate from APE to BPE
ϕ_z	Reversible vertical buoyancy flux rate (rate from KE to APE)
Re	Reynolds number
ρ	Density

ρ_0	Reference density
Ro	Rossby number
Sc	Schmidt number
σ_{ij}	Deviatoric stress tensor
$\vec{\omega}$	Vorticity vector with components $(\omega_x, \omega_y, \omega_z)$
$\vec{u}$	Velocity vector with components (u, v, w)
a	Mode-2 wave amplitude
c	Mode-2 wave speed
c_0	Linear, long wave, mode-2 wave speed
c_g	Group speed
c_p	Phase speed
E_a	Available energy (AE) which is the sum of KE and APE
E_k	Kinetic energy (KE)
E_p	Potential energy (PE)
E_t	Total energy which is the sum of KE and PE
E_{ap}	Available potential energy (APE)
E_{bp}	Background potential energy (BPE)
e_{ij}	Strain rate tensor
f	Coriolis parameter
L_x	Length of x domain
L_y	Length of y domain
L_z	Length of z domain
N	Buoyancy frequency

N_x	Number of grid points along the x-dimension
N_y	Number of grid points along the y-dimension
N_z	Number of grid points along the z-dimension
T	Tracer field

Chapter 1

Introduction

1.1 Internal waves

Internal waves (IWs) are waves that exist within a density stratified medium which have gravity as the primary restoring force. They are common [Global Ocean Associates, 2004]and have important implications for environmental processes within the ocean and in the atmosphere because of their ability to transport large amounts of energy over vast distances [Helfrich and Melville, 2006]. In this work, we will focus on oceanic internal waves.

An internal solitary wave (ISW), in differentiation from an internal wave, is a single wave of permanent form resulting from a balance of non-linear steepening and dispersion. ISWs travel horizontally along the pycnocline, the region of strong vertical stratification. In the open ocean, and in the right conditions, an ISW may travel for thousands of kilometres until either reaching a coast or encountering a change to other local environmental conditions.

When ISWs reach shallow waters in coastal regions, the waves break releasing internal wave energy by inducing high levels of local turbulence [Lamb, 2014]. This breaking process may interact with the bottom boundary layer (BBL) to cause mixing between the BBL and the main water column [Stastna and Lamb, 2008] which can cause resuspension of bottom boundary material [Bourgault et al., 2014]. Often this matter is nutrient rich and is beneficial for the ecosystem when dispersed [Corbett, 2010].

ISWs are a well-studied natural phenomenon with a long, rich, and extensive literature (see Helfrich and Melville [2006], Ostrovsky and Stepanyants [1989] for just two reviews). Observations in nature make it very clear that internal waves are highly non-linear because

of their large amplitudes compared to the vertical scale of the stratification they exist within [Helfrich and Melville, 2006].

Internal solitary waves come in a variety of types, called modes (Figure 1.1), which describe the vertical structure of the ISW. Section 1.3 will give a mathematical introduction to where these modes come from, but the general idea of a mode is that it describes the number of oscillations in the vertical structure of a wave. The first mode, or mode-1, is the primary expression and describes a wave that displaces all isopycnals in the same vertical direction (Figure 1.1a). The second mode ISW has isopycnals that separate away from or contract towards a fixed depth (Figure 1.1b). Until recently, mode-2 ISWs have not been observed as much as mode-1 ISWs. These recent observations have caused a resurgence of interest in the second mode and warrant further detailed investigation into them. Observation of mode-2 ISWs have been made in the Andaman Sea [Magalhaes and da Silva, 2018], New Jersey shelf [Shroyer et al., 2010], South China Sea [Yang et al., 2010, Ramp et al., 2012, 2015, Dong et al., 2016], Knight Inlet [Farmer and Smith, 1980], Georges Bank [Bogucki et al., 2005], and the Mascarene Ridge in the Indian Ocean [Konyaev et al., 1995, da Silva et al., 2011, 2015].

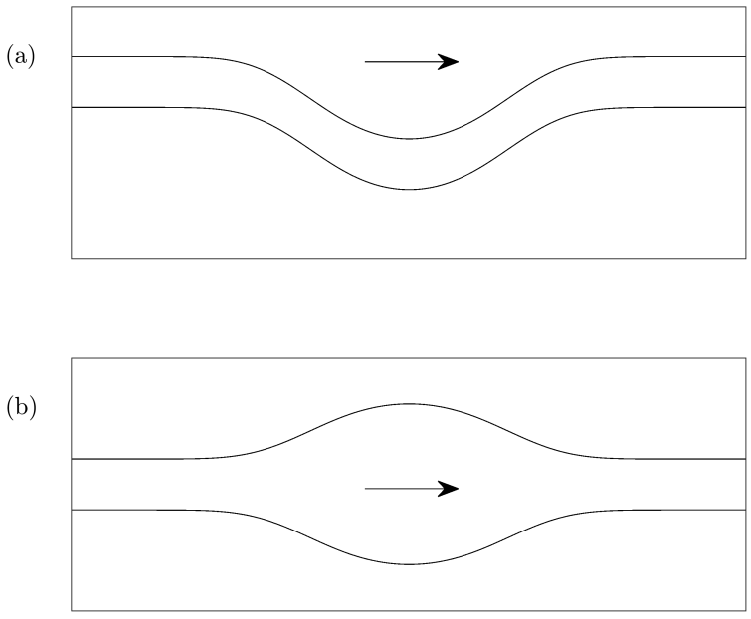

Figure 1.1: Schematics of the displacement of isopycnals of a rightward moving (a) mode-1 ISW of depression, (b) convex mode-2 ISW.

Many of the oceanic observations are made on or near the coastal shelf [Yang et al., 2010, Shroyer et al., 2010], or in a region with a large ridge [Ramp et al., 2012, 2015, da Silva et al., 2015]. Though all of these observations have been made in regions with large variations in topography, nearly all of the numerical and laboratory experiments to date have used a constant fluid depth. We will look at both the flat bottom topography case to study the mass transport efficiency of a mode-2 ISW (chapter 3), as well as the interaction of a ISW with a ridge to analyze resuspension capabilities (chapter 5). Chapter 4 will then look at the effect of a rotating reference frame on the development of the mode-2 ISW. These three chapters have been published in peer-reviewed journals.

1.2 Governing equations

Under the Boussinesq approximation, the governing equations for a fluid in a rotating reference frame are the Navier-Stokes equations [Kundu et al., 2012],

$$\frac{D\vec{u}}{Dt} + 2\vec{\Omega} \times \vec{u} = -\frac{1}{\rho_0}\nabla p + \frac{\rho}{\rho_0}\vec{g} + \nu\nabla^2\vec{u}, \tag{1.1a}$$

$$\nabla \cdot \vec{u} = 0, \tag{1.1b}$$

$$\frac{D\rho}{Dt} = \kappa\nabla^2\rho, \tag{1.1c}$$

where $\vec{u}$ is the velocity, p is the pressure, $\vec{g}$ is the gravitational acceleration, ν is the kinematic viscosity, $\frac{D}{Dt} = \frac{\partial}{\partial t} + \vec{u}\cdot\nabla$ is the material derivative, κ is the molecular diffusivity of the density, and ρ, ρ_0 are the density and reference density, respectively. (1.1) does not include the centripetal acceleration as this is often unimportant in comparison to the other terms.

The boundary conditions vary between different cases and will ultimately depend on whether boundary layer effects are important. The numerical implementation of the free-slip boundary condition is significantly faster than that with a no-slip conditions because the use of a Chebyshev grid in the latter results in a restrictive Courant-Friedrichs-Lewy (CFL) condition due to small grids near the boundaries. The no-slip condition is used precisely when the clustering of the grid near the boundary is desirable, such as when and ISW interacts with the bathymetry.

Specifically, the no-slip boundary condition sets all flow tangential to a boundary to zero ($\vec{u}\cdot\hat{t} = 0$), while the free-slip condition (in SPINS) sets the gradient of the flow to zero at the boundary ($\nabla\vec{u}\cdot\hat{n} = 0$). No-flux boundary conditions ($\vec{u}\cdot\hat{n} = 0$ and $\nabla\rho\cdot\hat{n} = 0$)

are always used. That is, there is no normal flow and no diffusive flux of density across the boundary of the domain.

1.3 Simplistic theoretical introduction to IWs

To gain a better theoretical understanding of the structure of internal waves we will simplify (1.1). Let us assume that the flow is two dimensional, inviscid, and is not rotating. Linearizing about a null mean velocity state gives,

$$u'_t = -\frac{1}{\rho_0} p'_x, \tag{1.2a}$$

$$w'_t = -\frac{1}{\rho_0} p'_z + \frac{\rho'}{\rho_0} g, \tag{1.2b}$$

$$u'_x + w'_z = 0, \tag{1.2c}$$

$$\rho'_t + w\overline{\rho}_z = 0, \tag{1.2d}$$

where primes denote perturbed variables, subscripts denote derivatives, and $\overline{\rho}$ is the background stratification (ie. $\rho = \overline{\rho}(z) + \rho'(x,z)$). The vertical momentum equation has been adjusted to cancel the hydrostatic component of the pressure with the background stratification. The continuity equation enables the use of a stream-function, ψ, where $u' = \psi_z$ and $w' = -\psi_x$. Substituting this into the other equations, dropping primes and taking a few derivatives gives,

$$\psi_{ttzz} = -\frac{1}{\rho_0} p_{txz}, \tag{1.3a}$$

$$-\psi_{ttxx} = -\frac{1}{\rho_0} p_{txz} + \frac{g}{\rho_0} \rho_{tx}, \tag{1.3b}$$

$$\rho_{tx} - \psi_{xx}\overline{\rho}_z = 0, \tag{1.3c}$$

Subtracting equation (1.3b) from (1.3a) and using equation (1.3c) gives,

$$\left(\nabla^2 \psi\right)_{tt} + N^2(z)\psi_{xx} = 0, \tag{1.4}$$

where,

$$N^2(z) = -\frac{g}{\rho_0}\frac{d\overline{\rho}}{dz}, \tag{1.5}$$

is the square of the buoyancy frequency which describes the oscillation rate of a particle infinitesimally displaced from its equilibrium position. Thus far we have not mentioned

anything about boundary conditions, but if we assume the rigid lid approximation (which is done within our numerical model) at $z = L_z$ and have a flat bottom at $z = 0$, then the boundary conditions are $w = -\psi_x = 0$ at those depths. Assuming the wave ansatz, $\psi = \exp(i(kx - \sigma t))\,\phi(z)$, where k is a horizontal wavenumber and σ is the dispersion relation, gives the ordinary differential equation,

$$\phi_{zz} + \left(\frac{N^2 k^2}{\sigma^2} - k^2\right)\phi = 0, \tag{1.6}$$

with boundary conditions $\phi = 0$ at $z = 0, L_z$. A simple, analytic solution exists for a linear stratification (or equivalently a constant buoyancy frequency). In this case the quantity within the brackets can be treated as a single quantity, which we label, m^2. Solutions that satisfy these boundary conditions are,

$$\phi(z) = \sin(mz), \tag{1.7}$$

where $m = n\pi/L_z$. Note that this implies that the enforcement of the boundary condition at $z = L_z$ quantizes the vertical wavenumber. This is the origin of the vertical modal structure of internal waves (Figure 1.2a). For $n = 1$, the isopycnals rise and fall together in unison at all depths. In contrast, the second mode has isopycnals converge and diverge upon the mid-depth in a linear stratification. If the stratification is two layers with a smooth, thin, transition region between the two layers (the pycnocline), then the isopycnals expand and contract about the centre of the pycnocline, though the modal structure must be solved numerically. This configuration enables the formation of a trapped core within the expanded pycnocline region when the wave amplitude is large and no longer adequately described by linear theory.

For the linear stratification the dispersion relation, σ, phase speed, c_p, and group speed, c_g, are found by substituting the vertical structure function (1.7) into (1.6). After some rearrangement we find,

$$\sigma^2 = \frac{k^2 N^2}{k^2 + m^2}, \tag{1.8a}$$

$$c_p = \frac{\sigma}{k} = \frac{N}{\sqrt{k^2 + m^2}}, \tag{1.8b}$$

$$c_g = \frac{\partial \sigma}{\partial k} = \frac{m^2 N}{(k^2 + m^2)^{3/2}}. \tag{1.8c}$$

All $n > 1$ mode waves have phase speeds which are slower than the long-wave mode-1 phase speed (Figure 1.2b). More importantly, the energy travels at the group speed, which again

is slower for higher modes than a long-wave mode-1 wave (Figures 1.2c). However, there exists a wavenumber for which the group speed is the same for two different modes. This means that the long wave speed of a wave of mode greater than one will always correspond to a mode-1 wave of some wavelength. This enables higher mode waves to radiate energy into lower modes since the lower mode is more stable than the higher, ultimately all this energy will be transferred to a mode-1 wave since it is the most stable. Higher mode waves (mode number greater than unity) have no mechanism for regaining this energy and will eventually deteriorate.

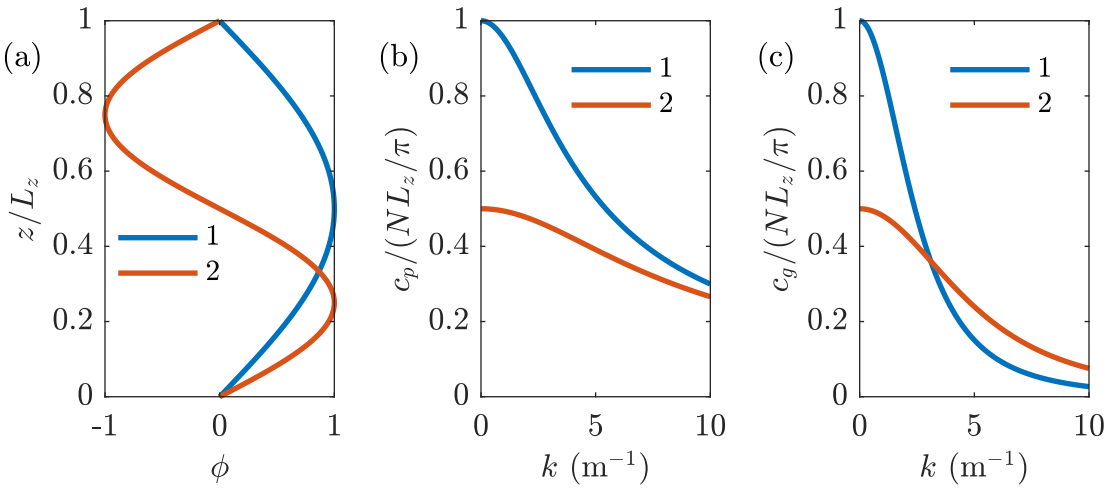

Figure 1.2: (a) Vertical structure function, (b) phase speed, and (c) group speed for the first two modes of linear internal waves in a linear stratification. The horizontal axis in (b) and (c) is the wavenumber.

1.4 Mode-2 ISWs

Mode-2 ISWs exist in two varieties: convex and concave (figure 1.3). The vast majority of mode-2 ISWs reported are convex (or varicose) waves, characterized by the expansion of isopycnals away from the pycnocline centre. Due to this bulbous-like shape, large-amplitude solitary-like waves have the ability to form trapped cores which may transport mass [Salloum et al., 2012, Brandt and Shipley, 2014, Stamp and Jacka, 1995, Terez and

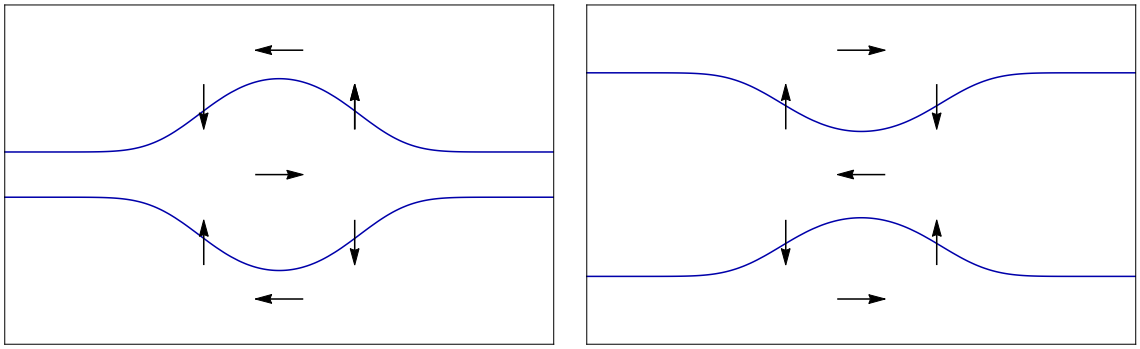

(a) Convex wave. (b) Concave wave.

Figure 1.3: Types of mode-2 ISWs. Blue lines are the edges of a pycnocline. Arrows indicate fluid velocities for rightward propagating waves.

Knio, 1998]. Concave mode-2 ISWs are the inverse of convex waves in that they are identified by a pinching of the pycnocline [Yang et al., 2010]. Due to their structure, concave waves do not form trapped cores and are therefore ineffective at transporting material [Mehta et al., 2002]. Yang et al. [2010] found that only concave waves are able to form when the middle-layer thickness (of a three-layer system) was greater than half the total water depth. If the middle layer is less than half the total water depth then the authors found that a convex wave is more likely to form.

The long distance transport of material, whether it be nutrients, contaminants, plankton, or larger aquatic animals, has great implications on the environmental sustainability of an ecosystem. For example, internal waves have been associated with the accumulation of predators due to a high concentration of prey at wave crests [Stevick et al., 2008]. Throughout this thesis, a focus will be made on the internal (wave-core) dynamics of convex mode-2 ISWs with a view to the implications on environmental impacts.

Chapter 2

Numerical Methods

Each year, the resolutions of numerical simulations continue to increase since computational power increases and more resources become available. The majority of this work uses numerical methods to solve and analyze phenomena related to mode-2 internal solitary waves. Some experimental work is also compared to the numerical results in Chapter 5. Before discussing the results of these simulations and experiments a description of some numerical projects will be presented. This is work that has been done to improve our numerical model.

The Spectral Parallel Incompressible Navier-Stokes Solver (SPINS) is used throughout as the numerical model. Details of the construction and validation of SPINS are described in Subich et al. [2013]. SPINS is a pseudo-spectral model capable of solving the Navier-Stokes equations to a high degree of accuracy in rectilinear geometry and a particular class of curvilinear geometries. It is a unique model because of the spectral accuracy in conjunction with geometry that is not solely restricted to a rectilinear domain.

Some limitations, however, are required on the boundaries. The main constraints are: 1) curved boundaries can only be present along one dimension (such as the upper, $z_l = \min(z)$, and/or the lower, $z_u = \max(z)$, boundaries) and be a function of one dimension (for example $z(x)$), 2) curved boundaries must be continuous to the number of points along the varying dimension, and 3) all other boundaries must be planar with their normal along one of the primary axes. In regard to a bottom boundary, the spatial variations would result in a span-wise invariant ridge or shelf break. SPINS uses a third-order multi-step method with an adaptive time step to evolve the flow. Time dependent simulations were completed on the high-performance computer cluster Shared Hierarchical Academic Research Computing Network (SHARCNET, www.sharcnet.ca).

Other numerical methods such as finite difference, finite volume, or spectral finite elements methods exist. But these methods are typically highly diffusive, while SPINS is not. Finite difference methods are generally highly parallelizable, while SPINS is sufficiently parallel to be applicable on high performance computing (see scaling analysis in Appendix A).

2.1 Schmidt number

One discussion that will arise in each of the results chapters is the issue of Schmidt number. The Schmidt number, $\mathrm{Sc} = \nu/\kappa$, is the non-dimensional quantity comparing the rates of momentum diffusion to molecular diffusion. A high Schmidt number corresponds to high momentum diffusion compared to molecular diffusion and can easily result in steepening of tracer or density gradients. These gradients do not diffuse quickly (compared to the momentum) and are thus advected by the flow, possibly forming thin filaments. Physical quantities of the Schmidt number are ~ 7 for a thermally-stratified fluid and ~ 700 for a salt-stratified fluid. Schmidt numbers on the order of a thermally-stratification are numerically attainable, whereas those for salt-stratification are not.

The Schmidt number originates from the non-dimensionalization of the density equation in (1.1). Explicitly, (1.1c) when non-dimensionalized becomes

$$\frac{D\rho^*}{Dt} = \frac{1}{\mathrm{Re}}\frac{1}{\mathrm{Sc}}\nabla^2\rho^* \tag{2.1}$$

where ρ^* is the non-dimensionalized density, and $\mathrm{Re} = ul/\nu$ is the Reynolds number using a suitable characteristic velocity, u, and length scale, l.

In general, high Schmidt number flows are numerically very difficult for any scheme since the dynamically small-scale features require extremely high resolutions. It should be mentioned that the flow must be sufficiently dynamic to result in stretching of the tracer to increase the gradient with which diffusivity does not then play an important role on at high Sc.

An estimate of the numerical resolution can be calculated from the Kolmogorov scale [Kolmogorov, 1941] and Batchelor scales [Batchelor, 1959] when based on the maximum

local dissipation rate. These are defined as

$$\eta = \left(\frac{\nu^3}{\epsilon_{\max}}\right)^{1/4}, \tag{2.2}$$

$$\lambda_B = \left(\frac{\nu\kappa^2}{\epsilon_{\max}}\right)^{1/4} = \eta \mathrm{Sc}^{-1/2}. \tag{2.3}$$

A key component in Kolmogorov's theory is that of local isotropy of small-scale motions. However, this hypothesis has been questioned, even not so long after its initial publication. In spite of these questions, Kolmogorov's theory has been incredibly successful and thus will be used for computing the smallest energy containing length scales.

For example, a numerical simulation of a three-dimensional gravity current with $\mathrm{Sc} = 10$ in a domain of size $0.2\mathrm{m} \times 0.02\mathrm{m} \times 0.02\mathrm{m}$ is estimated to require $10^4 \times 10^3 \times 10^3 \approx 80 \cdot 512^3$ points. Currently the highest attainable resolutions use $\sim 8 \cdot 512^3$ which is an order of magnitude below the estimated requirement. This estimate comes from using Taylor's theorem to make an estimate of the viscous dissipation which is then used to calculate the Kolmogorov microscale and thus the maximum grid spacing.

This is the main difficulty with high resolution direct numerical simulations of physically relevant Schmidt numbers: the resolutions required are unattainable. In the literature, a good majority of simulations use Schmidt numbers well below correct physical values simply because they are numerically stable. A standard choice is $\mathrm{Sc} = 1$.

Other numerical methods, such as finite difference schemes, can have inaccuracies arise in high Schmidt number flows because the effective diffusivity caused by the numerical scheme is higher than the physical diffusivity, which reduces the effective Schmidt number. SPINS and other spectral methods do not have any implicit diffusivity, but rather only a prescribed numerical filter to ensure that energy does not build at small-scales. For spectral methods, this containment of small-scale growth is explicitly specified and can be adjusted for an individual problem or simulation. This is not the case for other methods which have an implicit numerical diffusivity.

2.2 SPINS energy diagnostics

2.2.1 Energy budget

Recent work on SPINS has included the implementation of a full energy budget and energy conversion rates. Though (1.1) describes a non-inertial reference frame, the analysis of

Winters et al. [1995] is unchanged as the additional term does not impact the kinetic or potential energy equations. Should the centripetal acceleration be included (which is not done here) then an additional term will need to be added to the potential energy equation (2.9). The following is primarily based on the work of Winters et al. [1995].

The kinetic energy (KE, or E_k) within a volume, V, is

$$E_k = \frac{\rho_0}{2} \int_V (u^2 + v^2 + w^2) dV. \tag{2.4}$$

Taking the volume integral of the dot product of (1.1a) with $\rho_0 \vec{u}$ gives the rate of change of kinetic energy as

$$\frac{dE_k}{dt} = -\phi_z - \epsilon - \phi_{ks}, \tag{2.5}$$

where ϕ_z is the reversible vertical buoyancy flux rate (energy conversion rate from KE to PE), ϵ is the viscous dissipation rate, and ϕ_{ks} is the flux of energy across the boundary of the domain. These are defined as

$$\phi_z = \int_V \rho g w dV, \tag{2.6}$$

$$\epsilon = \int_V 2\mu e_{ij} e_{ij} dV, \tag{2.7}$$

$$\phi_{ks} = \int_S \left(p\vec{u} + \frac{\rho_0}{2} |\vec{u}|^2 \vec{u} - \vec{u} \cdot \vec{\sigma} \right) \cdot \hat{n} dS, \tag{2.8}$$

where $e_{ij} = \frac{1}{2}(\frac{du_i}{dx_j} + \frac{du_j}{dx_i})$ is the strain rate tensor, and $\vec{\sigma} = 2\mu e_{ij}$ is the deviatoric stress tensor.

The potential energy (PE, or E_p) is

$$E_p = \int_V \rho g z dV. \tag{2.9}$$

The rate of change of PE is

$$\frac{dE_p}{dt} = \phi_i + \phi_z + \phi_{ps}, \tag{2.10}$$

where ϕ_i is the rate of conversion from internal energy to potential energy through diffusion and ϕ_{ps} is the flux of energy across the boundary of the domain. They are defined as

$$\phi_i = -g\kappa \int_A \rho(z = z_u) - \rho(z = z_l) dA, \tag{2.11}$$

$$\phi_{ps} = -g \oint_S z\rho\vec{u} \cdot \hat{n} dS + g\kappa \oint_S z \nabla\rho \cdot \hat{n} dS, \tag{2.12}$$

where $\int_A dA = \int_{y_1}^{y_2}\int_{x_1}^{x_2} dxdy$ is the integral over both horizontal extents (assuming that the side walls are vertical at $x = x_1, x_2$ and $y = y_1, y_2$). z_u and z_l are the positions of the upper and lower boundaries respectively and can be a function of either x or y.

If we define a closed system as one in which the boundaries are solid (i.e. no flow or diffusion through the boundary), or the domain is periodic, then all the surface integral terms in (2.5) and (2.10) are zero. That is $\phi_{ks} = \phi_{ps} = 0$. Since the numerical model used in this research (SPINS) only uses closed domains we will ignore these surface terms for the remainder of this work.

The total energy is $E_t = E_k + E_p$, where the rate of change of which is the sum of (2.5) and (2.10),

$$\frac{dE_t}{dt} = \phi_i - \epsilon. \tag{2.13}$$

Numerically, energy can be introduced or removed at any point as a result of the numerical method or because of numerical filtering. Supposing that the rate of energy removed by the filter is Γ, (2.13) becomes,

$$\frac{dE_t}{dt} = \phi_i - \epsilon - \Gamma. \tag{2.14}$$

Since all terms but the numerical energy rate term can be calculated, this gives a means of solving for the energy removed or added by the numerical method,

$$\Gamma = -\frac{dE_t}{dt} + \phi_i - \epsilon = -\frac{d}{dt}\left(E_k + E_p\right) + \phi_i - \epsilon. \tag{2.15}$$

The total energy removed by the numerical method is simply the time integral of (2.15),

$$\widetilde{\Gamma} = -\Delta E_k - \Delta E_p + \widetilde{\phi_i} - \widetilde{\epsilon}. \tag{2.16}$$

where $\widetilde{\cdot} = \int_0^T \cdot dt$ is the cumulative effect of a given quantity. The first two terms of (2.16) are easily determined from the KE and PE at the start and end of a simulation. The latter two terms require the constant evaluation of the rates over the entire simulation. Fortunately, ϕ_i is a simple double integral. The heaviest computation is required to calculate the dissipation which is a product of multiple derivatives. Though, it requires the most work, it is still highly efficient in SPINS due to the effective parallelization of the derivative calculation.

The potential energy can also be broken down into the available potential energy (APE or E_{ap}) and the background potential energy (BPE or E_{bp}). The available energy (that which is available to be used to do mechanical work) is therefore defined as

$$E_a = E_k + E_{ap} = E_t - E_{bp}. \tag{2.17}$$

Combining (2.17) and (2.14) gives

$$\frac{dE_a}{dt} = -\frac{dE_{bp}}{dt} + \phi_i - \epsilon - \Gamma \tag{2.18}$$

$$= -\phi_d + \phi_i - \epsilon - \Gamma \tag{2.19}$$

$$= -\phi_m - \epsilon - \Gamma \tag{2.20}$$

where ϕ_d is the rate of change of the background potential energy, $\phi_d = \frac{dE_{bp}}{dt}$, and $\phi_m = \phi_d - \phi_i$ is the rate of conversion of APE to BPE. Clearly, the available energy is lost in one of three ways: through mixing into the background potential energy, through viscous dissipation into internal energy, or through the numerical scheme.

Should one be interested in the instantaneous mixing efficiency of a process, the rates ϕ_m and ϵ can be used in an appropriate way.

If a body force, F, is applied throughout the fluid (such as tidal forcing) any equation dependent upon the rate of change of KE gains the additional term

$$\phi_f = \int_V \rho_0 \vec{u} \cdot \vec{F} dV, \tag{2.21}$$

where $\vec{F}$ is the body force in question.

The previous analysis is valid for a density stratified fluid. If the fluid is stratified with a combination of the temperature or salinity, then the equation of state must be used within the definition for potential energy. Since SPINS uses a nonlinear equation of state [Brydon et al., 1999] (2.10) will contain far more terms which will need to be tracked.

SPINS now calculates the following fields: ϵ, ϕ_i, E_k, E_p, E_{bp}. From these the remaining terms in the budgets can be calculated in post-processing by either taking a derivative, integral, or difference.

2.2.2 Diagnostics in MATLAB

In this section, an example of the implementation of the energy budget in SPINS is presented. The chosen case is the generation of a three-dimensional Kelvin-Helmholtz (KH)

billows from a stratified shear flow. Though this document is not a detailed study of shear instabilities, this particular case demonstrates effectively the utility of these diagnostics. Furthermore, the authors of SPINS used this case in validating the model [Subich et al., 2013].

SPINS writes all diagnostics into the file `diagnostics.txt` from which any program can access the data. The MATLAB (The MathWorks Inc., Nantick, Massechusetts, USA) function `plot_diagnos.m` has been created to calculate the additional energy budget terms and to present the results in meaningful text and plots. This function is available in the SPINSmatlab package described in section 2.4.

Assuming all flags for energy diagnostics were set to true, `plot_diagnos.m` prints to screen the following information:

```
---- Timings ----
Most recent sim. time: 200.00 s
Total clock time:      01:00:23 (D:H:M)
Average write time:    1.511 s
Avg. sim. step time:   5.614 ms
Avg. clock step time:  2.462 s
Avg. clock time per sim. sec.: 00:00:07:18 (D:H:M:S)
Est. clock time remaining:     00:00:00:00 (D:H:M:S)

---- Kolmogorov and Batchelor Scales ----
dx/eta =      40.1811
dx/lambda_B = 40.1811

---- Energy ----
As a percentage of the initial available energy
Available energy lost:   24.15 %
  > through mixing:         7.75 %
  > through dissipation:    7.07 %
  > through numerics:       9.33 %
Total energy lost:       16.25 %
  > through diffusion:     -0.15 %
  > through dissipation:    7.07 %
  > through numerics:       9.33 %
Change in BPE:            7.90 %
```

```
---- Mixing efficiency ----
Change in BPE / |change in AE|:   0.33
Cumulative mixing eff.:           0.32
Max inst. mixing eff.:            0.63
Max inst. mixing coeff.:          1.72
```

The first section (Timings) lists temporal information of the SPINS run. Such information includes how far the simulation has progressed (Most recent sim. time), how long it took to get there (Total clock time), and then averages of time stepping quantities. In this case the average simulation step time was 5.6 ms which took an average of 2.5 s to compute. Should the simulation be incomplete, the last line lists the estimated time remaining for the simulation based on the 50 most recent steps.

The second section lists the maximum grid spacing (dx) as a factor of the Kolmogorov (eta) and Batchelor scales (lambda_B) (2.2). Though this simulation (and most presented in this work) do not fall under the classification of traditional homogeneous turbulence [Pope, 2000], within which these are usually applied, we shall utilize the standard definitions to compute an estimate for the smallest dynamically important length scale.

For the presented simulation, the largest grid spacing was roughly 40 times larger than the Kolmogorov and Batchelor scales. The factor is the same since a Schmidt number of 1 was used. In laboratory settings, the Schmidt number is typically greater than 1 which would reduce the Batchelor scale and increase the ratio. A factor of 40 is not ideal since a direct numerical simulation (DNS) should have this factor be approximately unity so that all energy can be cascaded into the dissipative range. Though not ideal, this simulation is still reasonably resolved in that it captures all the primary features of the Kelvin-Helmholtz billow.

The third section lists the amount of energy lost into different energy components as a percentage of the initial available energy. The available energy lost, $-\Delta E_a$, was 24% and consists of the total energy lost, $-\Delta E_t$, (16%) and the energy lost to the BPE, ΔE_{bp} (8%) (see (2.17)). The available energy lost can be broken down further (see (2.14)) into that lost through mixing (8%), viscous dissipation (7%), and the numerics (9%) which most often corresponds to the numerical filter. The total energy loses energy in two of the same pathways as the available energy (dissipation and numerics) but gains energy through diffusion (-0.15%). This value is negative to match the notation of energy being "lost" (see (2.12)). This pathway only converts energy in one direction and thus will always be negative; that is energy will only flow from internal energy to BPE and not vice versa.

The use of the word numerics here does not imply that the model is inaccurate, but rather that the resolution has been inadequate. Poor resolution leads to problems such as

aliasing which leads to blow-up [Boyd, 2001]. The numerical filter is our primary solution (one of many; section 2.5 covers another) to mitigate these issues. The large percentage of energy converted into the numerics is a result of the relatively low resolution which has forced the numerical filter to fulfill the role of the viscous dissipation. Should the resolution be increased substantially, the energy given to numerics will be transferred to energy given to the dissipation. A DNS using a filter can be considered comparable to an implicit large eddy simulations (ILES) scheme (see [Adams and Hickel, 2009] for a review of ILES).

The final section lists the mixing efficiency in a variety of ways (see Gregg et al. [2018] for a recent review). These are listed explicitly in terms of energy flux rate variables in table 2.1. The mixing efficiencies used here include the energy conversion rate to numerics, Γ. A properly resolved simulation will not be affected by this addition as the numerical scheme should have a negligible impact on the energetics. However, if the simulation is only marginally resolved then the numerical filter will be required to act as viscous dissipation to remove energy at the smallest resolved scales. If this is done properly, this will be indistinguishable and thus we should include it in the mixing efficiency calculation as the most basic definition of mixing efficiency is the ratio of the change in BPE due to mixing to all the energy lost [Gregg et al., 2018]. Lastly, if Γ is large then there may be other problems with the simulation and care should be taken. Though Γ is the largest of the three components used in the mixing efficiency calculation, the simulation is reasonably well-behaved even during the turbulent breakdown of the KH billows. That said, reasonably well-behaved does not make this simulation worthy of publication as an in-depth DNS of the turbulence of KH billows since other issues exist, examples of which are: the unphysical local fluctuations of the density field that surpass the initial density extrema due to insufficient filtering (to be seen shortly) and the large grid spacing to Kolmogorov scale. This simulation is, however, suitable for investigating the initialization of the KH billow.

The first two items in table 2.1 (ratio of the change in BPE and AE, and the cumulative mixing efficiency) will generally be similar values since the denominators are equivalent and the numerators are almost equivalent. ΔE_{bp} contains one more term, $\Delta E_{bp} = \int \phi_m + \phi_i dt$, where ϕ_i is often small enough to be ignored. The first is easier to calculate as only the initial and final KE, APE, and BPE are needed. The cumulative mixing efficiency requires the continued calculation of the diffusive energy flux, ϕ_i, but this is not difficult.

The maximum instantaneous mixing efficiency and mixing coefficient show the effectiveness of the mixing during the most energetic period. The mixing coefficient is just the ratio of the energy being converted into BPE and energy being converted into internal energy (and numerics). For this simulation the maximum instantaneous mixing efficiency of 0.63 is reasonable for the energetics of the chaotic breakdown of the Kelvin-Helmholtz

Table 2.1: Description of mixing efficiencies.

Printed form	Equation form
`Change in BPE / |change in AE|`	$\frac{\Delta E_{bp}}{\lvert\Delta E_a\rvert}$
`Cumulative mixing eff.`	$\frac{\int \phi_m dt}{\int \epsilon + \Gamma + \phi_m dt}$
`Max inst.  mixing eff.`	$\max_t \frac{\phi_m}{\epsilon + \Gamma + \phi_m}$
`Max inst.  mixing coeff.`	$\max_t \frac{\phi_m}{\epsilon + \Gamma}$

billow. Gregg et al. [2018] recently suggested that the mixing efficiency for global models should be chosen to be 0.2 since this is most accurate despite the unknowns surrounding the many processes inherent in ocean mixing.

In addition to the information listed above being printed to screen, a variety of useful diagnostic plots are made (Figure 2.1). Figure 2.1a presents a per iteration overview of when the the wall clock time per step (ΔT_c) or the simulation time (ΔT_s) step varied. The ratio of these, $\Delta T_c/\Delta T_s$, gives a good estimate of when the simulation requires more time. The higher the ratio the longer the time between saved outputs.

Figure 2.1b plots the maximum of the absolute value of the velocity and each component of velocity (upper panel) and the components of the kinetic energy. The KE components are defined as the kinetic energy associated with a particular velocity component (i.e. $\text{KE}_x = \frac{\rho_0}{2}\int u^2 dV$). For this Kelvin-Helmholtz billow case the majority of the kinetic energy and velocity for the duration of the simulation is along the channel (in the x-dimension). Vertical, and span-wise velocity components (which occur later), eventually grow in size, highlighting the growth of the initial instability and then the full breakdown into three-dimensional motion.

Figure 2.1c and 2.1d show the energy diagnostics from the previous section. The upper panels show either the energy within each energy component (2.1c) or the amount of energy converted through a particular pathway (2.1d). The lower panels display the rates of change of the values in the upper panel. The earliest non-trivial feature is the conversion of KE into APE around $t = 75$ s. Only once the flow becomes three-dimensional does energy transfer between other pathways (KE to internal energy through dissipation, APE to BPE, or into numerics). Though the energy into the numerics is quite large, it is primarily energy that would be dissipated and is not unphysical. The internal energy into BPE pathway is always

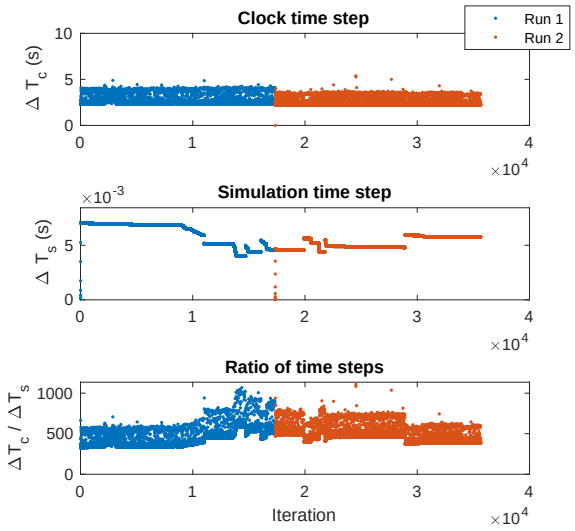

(a) Simulation timings.

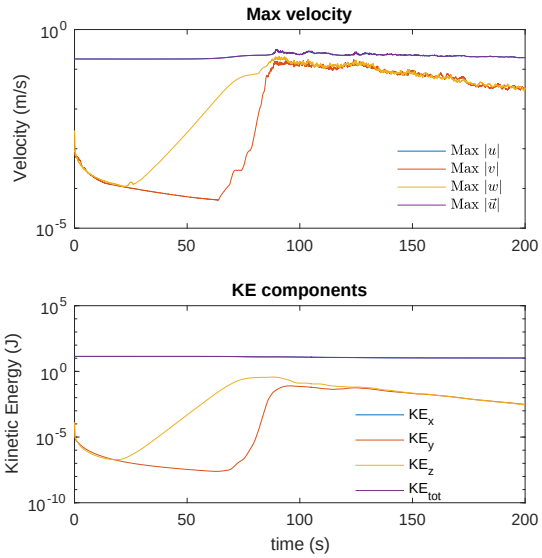

(b) Maximum velocity components, and kinetic energy components.

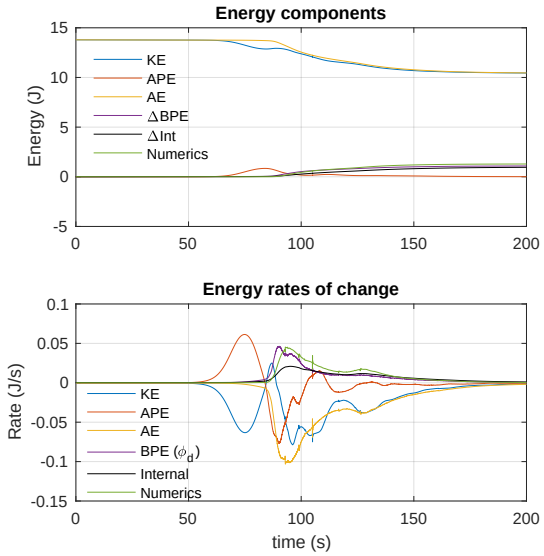

(c) Energy components and their rates of change.

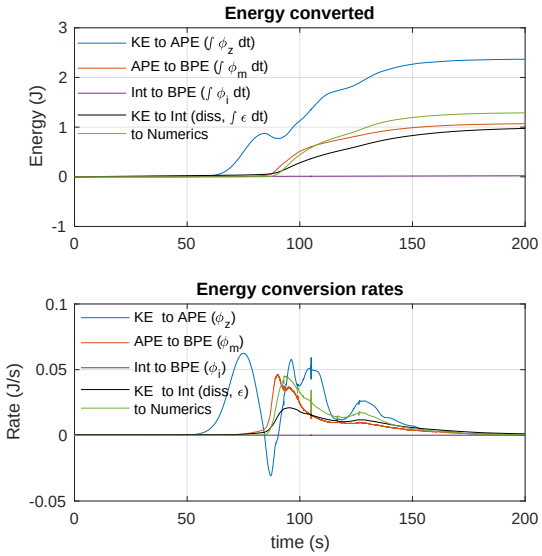

(d) Total energy converted and the energy conversion rates.

Figure 2.1: Simulation diagnostics.

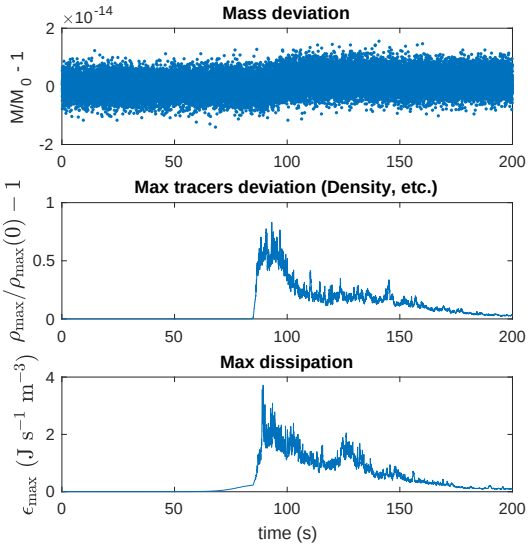

(e) Mass, maximum density deviation, and maximum local dissipation.

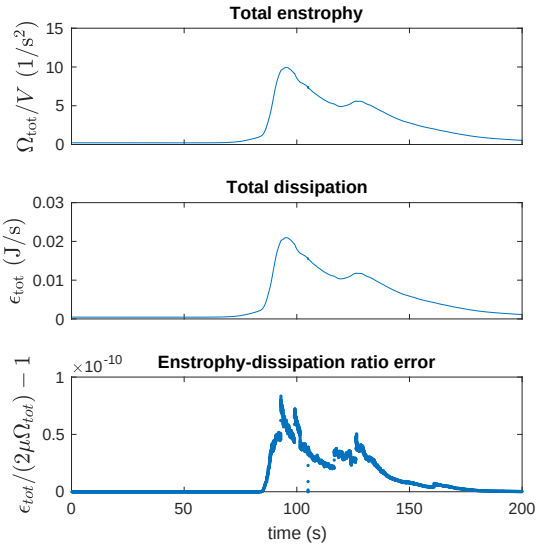

(f) Enstrophy, total dissipation, and the error of the scaled ratio.

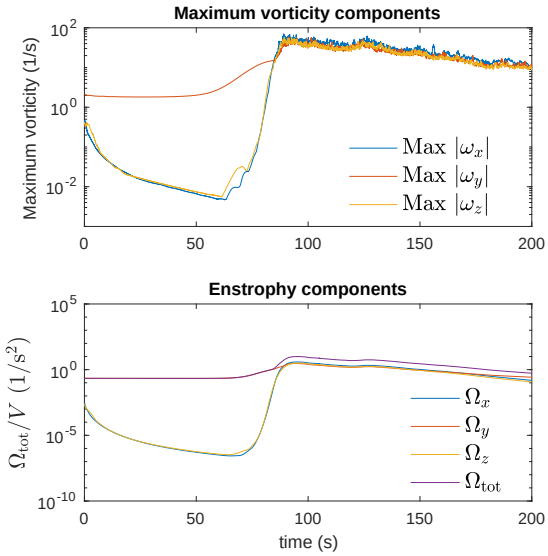

(g) Maximum vorticity components, and enstrophy components.

Figure 2.1: Simulation diagnostics.

negligible.

Figure 2.1e shows the deviation of the total mass (upper panel) the maximum of the absolute value of the density anomaly (middle panel), and the maximum of the local viscous dissipation rate (lower panel). The mass is essentially conserved throughout this simulation even though there is a growth of the maximum of density. The density should remain below its initial maximum value since cabbeling is prohibited because no equation of state is utilized. This is not the case here as the turbulent breakdown of the KH billow has been too vigorous for the chosen resolution and spectral aliasing has occurred. There is a correlation between when the flow is most turbulent and when the density reaches unphysical values.

Figure 2.1f displays the total enstrophy defined as $\int_V \frac{1}{2} |\vec{\omega}|^2 \, dV$ (upper panel), the total dissipation (middle panel), and the deviation of the scaled ratio from the expected value of zero (lower panel). The enstrophy and dissipation are scalar multiples of each other to very good precision in accordance with theory.

Lastly, figure 2.1g shows the maximum of the absolute value of each vorticity component (upper panel) and the enstrophy components (lower panel). This is quite similar to figure 2.1b but shows that there is equal enstrophy in each direction once the flow has fully developed three-dimensionally.

2.3 SPINS improvements

In addition to the computation of the full energy budget, a couple of other improvements have been made to SPINS. These have been done to increase functionality and ease of use. Most of these have been completed in coordination with fellow student Benjamin Storer (as was the BPE calculation).

2.3.1 Safety dump

One of the first things implemented was a safety write (or safety dump) when a compute allocation is nearing an end. This is extremely handy for large simulations which have a low checkpoint frequency and are run on a distributed system with limited run times. Previously a job would need to restart from a checkpoint even if substantial time had passed. Now, when SPINS nears the end of the allocated compute time all necessary fields (specified by the user) are written to disk. The flag `compute_time` in the configuration file specifies the allocated time.

2.3.2 Surface stress

SPINS solves the Navier-Stokes equations on a bounded domain, the flow within which can interact with the boundary of that domain. When a no-slip boundary condition is used, a surface shear stress exists which then forms a boundary layer. Measuring the surface stress provides a measure of the strength and location of the interaction with the surface. This is particularly useful for studying flow past a bump or hill such as in chapter 5.

For a bottom boundary that is dependent on a single dimension, $h(x)$, the tangential components of the surface stress are,

$$t_x = \frac{\mu}{1+h'(x)^2}\left[2h'(x)\left(w_z - u_x\right) + \left(1-h'(x)^2\right)\left(u_z + w_x\right)\right], \tag{2.22}$$

$$t_y = \frac{\mu}{\sqrt{1+h'(x)^2}}\left[v_z - h'(x)v_x\right]. \tag{2.23}$$

where t_x and t_y are the along channel and across channel stresses, respectively. Subscripts and primes denote derivatives. Further details on the origin of this result can be found in Xu [2015].

The following surface integrals are calculated:

$$t_{x1} = \int t_x \qquad \sqrt{1+h'(x)^2}dA \tag{2.24a}$$

$$t_{x2} = \int |t_x| \qquad \sqrt{1+h'(x)^2}dA \tag{2.24b}$$

$$t_{y1} = \int t_y \qquad \sqrt{1+h'(x)^2}dA \tag{2.24c}$$

$$t_{y2} = \int |t_y| \qquad \sqrt{1+h'(x)^2}dA \tag{2.24d}$$

$$t_{\text{tot}} = \int \sqrt{t_x^2+t_y^2}\sqrt{1+h'(x)^2}dA \tag{2.24e}$$

These bring the number of dimensions down to zero, providing a simple qualitative number. As with the diagnostics in the previous section, the MATLAB function `plot_stress` plots all values of (2.24) over time.

2.3.3 Case file standardization and clean-up

To ensure that the energy budget, surface stress, and other diagnostics are easily available, a variety of case files have been created or updated to include these features. Some cases

updated include: the vortex dipole, Kelvin-Helmholtz billows, and internal wave generation (each of which were described in the original publication of SPINS [Subich et al., 2013]). To improve case readability, these cases also had generic case independent code blocks moved to a more discrete location.

Lastly, a SPINS case file was written to compute derivatives and secondary fields such as vorticity and viscous dissipation. These fields, though not necessary for evolving the flow, are useful in analyzing the simulation when finished. It is possible to compute these fields with another software such as MATLAB, but that would not be as efficient since SPINS is an optimized parallel code, and each field is then available to be read at any further time without re-computation.

2.4 SPINSmatlab

Throughout this project, MATLAB has been the primary tool for analyzing results of each simulation. Much work has been put into creating a library, called SPINSmatlab, of functions to plot, compute, and provide details of a given simulation. One function, `plot_diagnos`, has already been described. A few others are described here.

An extremely useful function is `spins_plot2d` which plots a two-dimensional cross-section. Many optional arguments exist, such as the dimension and value to take the cross-section at. The plotting function automatically labels the axes, adds a colour bar, and creates a title of the field and time so that the figure is as descriptive as possible. This allows the user to not have to remember what is plotted. All this is done with a single command, speeding up analysis. The code is fast as only the needed information for the requested cross-section is loaded and/or computed.

Since the majority of this project follows the generation and propagation of internal waves, the function `characterize_wave` tracks the position, amplitude, and wavelength of the developing wave by following a particular, or a variety of, isopycnals. `plot_wave_char` will then plot the results of this characterization. Accurate measurements of these values are critical to properly describing the ISW.

We have begun to use perceptively uniform colour maps, so as to present results in as unbiased way possible. A variety of those that appear in this work have been created by Thyng et al. [2016] and are included in the SPINSmatlab package.

The last MATLAB function is described in the following section. The SPINSmatlab package is freely available and is stored on GitHub at `https://github.com/ddeepwel/SPINSmatlab.git`.

2.5 Spectral refinement

It is not uncommon for a simulation to develop short-lived regions of turbulence or for this turbulence to form well into a simulation (see figure 2.1 and discussion in section 2.2.2). In either case the initial resolution, which is sufficient for the majority of the simulation, might be insufficient during the period of heightened activity. If this occurs, the numerical filter will likely be inadequate due to the high energy flux to small scales. One could increase the strength of the filter to account for this, but that only solves the problem of blow-up and does not increase the accuracy of the simulation. To fully trust the simulation, the resolution needs to be increased. Once the turbulence dissipates (though, this isn't a necessity) the increased resolution might not be needed and we can coarsen the resolution. Here, the theory and implementation of refinement or coarsening will be presented for our numerical model SPINS.

2.5.1 Fourier theory

The theory will be presented in one dimension as it is simple and applicable to the code in practice. The Fourier series for a real, integrable function A on the interval $x \in [-\pi, \pi]$ is

$$A(x) = \sum_{n=-\infty}^{\infty} a_n e^{inx} \tag{2.25}$$

where a_n are the Fourier coefficients. Numerically, functions must be discretized onto a grid with a finite number of points. This can alternatively be thought of as limiting the number of modes used in the Fourier representation. For smooth functions which have Fourier series that converge quickly, this is not a problem as only a small number of modes are required to accurately represent the function. However, as has been mentioned, a time dependent simulation might require a greater number of modes to faithfully represent a function at some point in time.

If the Fourier series for A is truncated to keep only the lowest N modes, (2.25) then becomes,

$$A(x) \approx \sum_{n=-N/2+1}^{N/2} a_n e^{inx}. \tag{2.26}$$

The Nyquist frequency is the highest resolved frequency and corresponds to the highest resolved mode through the relation,

$$k_N = \frac{\pi}{\Delta x} = \frac{\pi N}{L_x} \tag{2.27}$$

All modes with frequency higher than the Nyquist frequency will be aliased to modes less than N and will contaminate the representation of the function. To maintain the accuracy of the simulation this must not be allowed.

To increase the resolution (2.26) will be adjusted to include more modes. To maintain accuracy, these additional modes will be initialized to have zero power. To reduce the resolution (2.26) will be truncated to keep fewer modes. Formally, if the resolution of the simulation is to be changed to use M modes, (2.26) become

$$A(x) \approx \sum_{n=-M/2+1}^{M/2} a_n^* e^{inx} \tag{2.28}$$

where

$$a_n^* = \begin{cases} a_n & -N/2+1 \leq n \leq N/2 \\ 0 & \text{otherwise} \end{cases} \tag{2.29}$$

if $M > N$ and

$$a_n^* = a_n \tag{2.30}$$

if $M < N$.

SPINS is a collocation method that places grid points at "cell" centers for Fourier grids. In physical space the grid points on the original grid are

$$x_j = a + (j + 1/2)\Delta x \tag{2.31}$$

for $j \in 0, 1, 2, ..., N-1$, and where a is the left most physical end point. The left most computational grid point is $x_0 = a + \Delta x/2$ and is dependent on the resolution. Therefore, a change in resolution must also change the grid and the data associated with those grid points. Fortunately this is easily accomplished with a phase correction in Fourier space by including

$$\phi = -ik(\Delta x_{\text{old}}/2 - \Delta x_{\text{new}}/2) \tag{2.32}$$

in the exponential in (2.28).

Therefore, increasing or decreasing the resolution of a given simulation consists of the following steps:

1. take the FFT of a field (velocity component, density, tracer, etc.)
2. pad with zeros or truncate the spectra to the desired length

3. apply the phase correction to recenter the grid

4. take the inverse FFT of the new field

This works for multidimensional data as well. Just extend or contract each dimension one after the other. Normally, the multidimensional Fourier coefficients would need to be dealt with as a whole, but since the Fourier coefficients are either changed to be zero or coefficients of value zero are added each dimension is essentially independent of the others.

The desired effect of no energy being created or destroyed occurs only when the resolution increases ($M > N$). This necessarily cannot occur when the resolution decreases since some non-zero energy will always remain in high frequency modes. It can be shown using Parseval's theorem that both potential and kinetic energy is lost. However, a reduction in the resolution will generally be made when there is no energy present in modes greater than the Mth mode.

If the grid is not periodic, but uses a free-slip condition instead, one additional change must be made. Depending on the field being adjusted the Fourier series will be replaced with a discrete sine or discrete cosine series. This then changes the FFT to a discrete sine transform (DST) or discrete cosine transform (DCT).

2.5.2 Chebyshev theory

The other possible grid in SPINS is the Chebyshev grid which clusters grid points near the boundaries. This is especially convenient when a no-slip condition is applied and sufficient resolution in the boundary layer is needed. The following description for adjusting the resolution is essentially the same as that for the Fourier grid in the previous section.

Rather than using a Fourier basis which requires that a given field have periodic, or one of Neumann or Dirichlet boundary conditions, the Chebyshev basis can be applied to any boundary condition, regardless of the field.

The Chebyshev series for a real, integrable function A defined on the interval $x \in [-1, 1]$ is

$$A(x) = \sum_{n=0}^{\infty} a_n T_n(x) \tag{2.33}$$

where a_n are the Chebyshev coefficients, and $T_n(x)$ are the Chebyshev polynomials of the first kind.

Again as with the Fourier series, only a finite number of modes, N, can be retained, so (2.33) becomes,

$$A(x) \approx \sum_{n=0}^{N-1} a_n T_n(x). \tag{2.34}$$

The endpoints of the Chebyshev grid are always on the boundary of the physical domain and will not change with the resolution. The steps to adjust the resolution of a Chebyshev grid are:

1. calculate the Chebyshev coefficients (the package Chebfun (http://www.chebfun.org/) exists to do this in MATLAB)
2. pad with zeros or truncate the spectra to the desired length
3. calculate the Chebyshev series

Similar to Fourier series there exists a Parseval-type theorem for Chebyshev series which can be used to show that the kinetic and potential energy are conserved when the resolution is increased.

2.5.3 Application

Now that is has been shown *how* to adjust the resolution, the difficulty comes in knowing *when* to adjust the resolution.

Specific methods such as Adaptive Mesh Refinement (AMR) are fundamentally linked to criteria for refinement and de-refinement. From these we can learn some standard criteria for when refinement is needed. Some example criteria [Tomasz Plewa, 2005, Löhner, 2008, Iapichino et al., 2008] are based on the:

- velocity
- vorticity
- vorticity gradient
- gradient of a tracer (such as density)
- Q-criterion (see section 4.6 for the definition of this)

- normalized second derivative of an important quantity (see (2.35))

Many of these criteria, especially their critical values, are problem dependent and are not applicable to a wide variety of situations. An early attempt at a general refinement condition used a normalized second derivative computed using finite differences of some quantity, u [Löhner, 1987]. In one dimension this criterion is explicitly written as

$$E_i = \frac{|U_{i+1} - 2U_i + U_{i-1}|}{|U_{i+1} - U_i| + |U_i - U_{i-1}| + \varepsilon\left(|U_{i+1}| + 2\,|U_i| + |U_{i-1}|\right)} \tag{2.35}$$

which is normalized and bounded, allowing a particular critical value to be applied for multiple problems. (2.35) originates from assuming that the error is proportional to the second derivative (this is like Taylor's remainder theorem since Löhner [1987] used linear shape functions in their finite element scheme). The normalization is chosen to avoid extreme refinement at sharp gradients, while the term with ε is chosen to ensure that unphysical oscillations (those caused by loss of monotonicity) are not refined [Löhner, 1987].

We focus on the magnitude of the vorticity, and the gradient of the density field as our primary criteria, in addition to some of the diagnostics presented in section 2.2.2. The former is a natural choice since strong, small-scale vortex filaments are correlated with turbulent motion. Fully developed turbulence produces a peak in the power spectra of the enstrophy near the Kolmogorov scale [Davidson, 2006]. Though the simulations of this thesis will not progress into fully-developed turbulence, the principle still applies for weaker mixing events.

Another choice is to measure the energy or energy flux rate near the Nyquist frequency by looking at the kinetic energy spectra. Refinement will be necessary if substantial energy is being transferred into small scales.

A variety of cases are analyzed to deduce the impact that spectral refinement has on the performance and accuracy of each simulation. These are: Kelvin-Helmholtz billows in two and three dimensions, and the mode-2 internal Kelvin wave experiment of chapter 4.

The KH billows are a good case study since the shear instability takes some time to develop. The first cases we ran did not force any particular mode of the instability; rather they were initialized with a random white-noise perturbation to the velocity field. This has the unintended consequence that the shear instability forms at a time which is partly dependent on the strength of the velocity perturbation and partly on the resolution (figure 2.2). Three of the four cases in figure 2.2 used the same perturbation, yet the coarsest

resolution never developed a shear instability. The instability did not form even after increasing the perturbation by an order of magnitude, such that the velocity perturbation is an order of magnitude smaller than the background velocity. The cases with the coarsest resolution are thus unable to generate shear instability without specifically forcing it directly. In general, many simulations will have an instability that is unknown *a priori* to running. Thus, even though the simulation does not require the resolution to remain stable, it does require sufficient resolution to form particular instabilities.

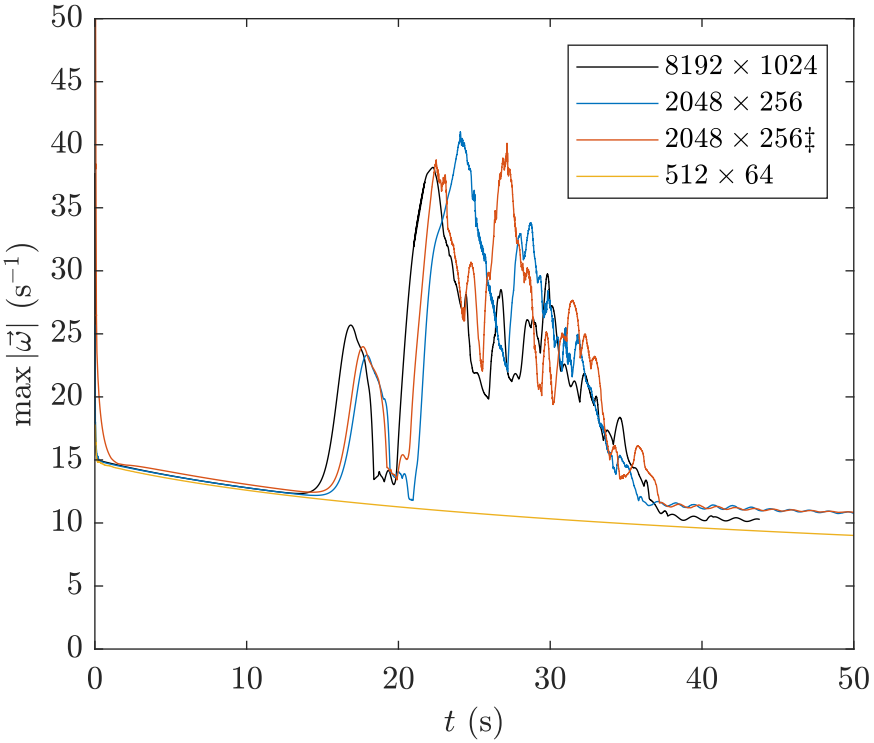

Figure 2.2: Maximum vorticity for two dimensional KH billows of various resolutions. The legend gives the grid resolution. ‡ corresponds to the case with large initial velocity perturbation.

Next we initialized with a density perturbation in addition to the same weak velocity perturbation (figure 2.3). This density perturbation was sinusoidal with wavelength equal to the most unstable mode as calculated from the Taylor-Goldstein equation [Kundu et al., 2012]. Here the Kelvin-Helmholtz billow forms earlier than when there was no density perturbation (the black line) and the billows form coincident in time regardless of the

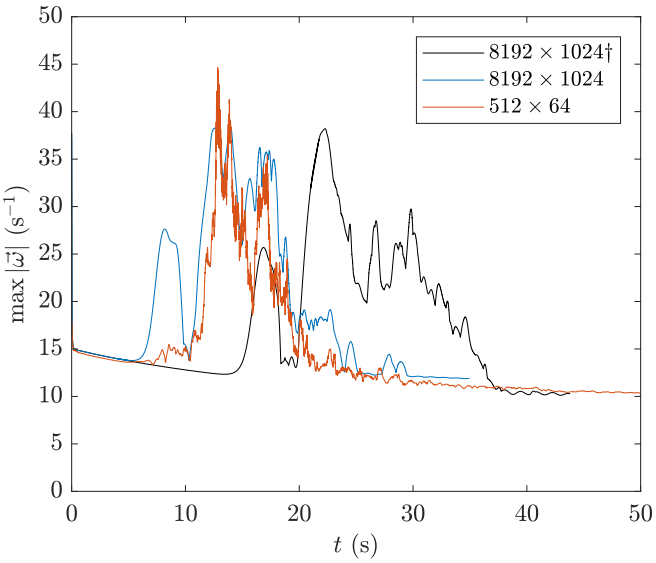

(a) Maximum vorticity.

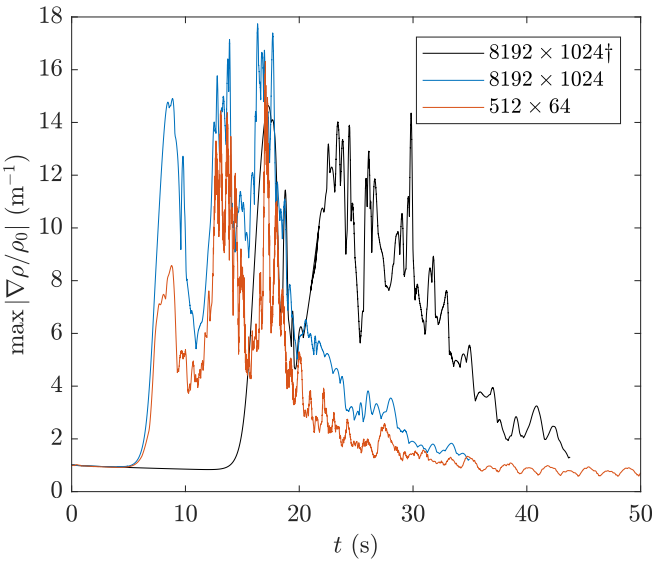

(b) Maximum density gradient.

Figure 2.3: a) Maximum vorticity and b) maximum density gradient for two dimensional KH billows of various resolutions. Coloured lines were initialized with a small sinusoidal adjustment to the density field. † is the same as the black line in figure 2.2.

resolution. This is most clear in the density gradient plot rather than the vorticity since the resolution is not large enough to accurately represent the growth in that field.

Disregarding the temporal delay in the formation of the KH billows of the first cases, the spectral refinement can still be applied. Figure 2.4 shows the impact due to refinement. Solid lines are the high resolution cases, and the case with a superscript r indicates refinement from the presented resolution onto that of the higher. The upper row of figures 2.4 and 2.5 corresponds to cases with the velocity perturbation only, while the lower row corresponds to the velocity and density perturbation cases. The velocity perturbation case is refined at $t = 16$ s, the density and velocity perturbation case is refined at $t = 6$ s.

All variables ($\max|\vec{\omega}|$, $\max|\nabla\rho/\rho_0|$, and $\max\epsilon$) of the refined cases match those of the high resolution (while also ignoring the phase delay for the velocity perturbation cases). This is quite good, but also expected since the refinement took place early enough in the billow formation.

The maximum of the density field (right column of figure 2.5) gives a measure of when insufficient resolution was used. As described in section 2.2.2 the maximum density should not grow over time, yet the weakest resolution shows this to the be case. The higher resolution and refined cases do not have this density growth and hence are much more accurate solutions.

An estimate for the computational savings can be made based on the required time step and the computational cost. The lower resolutions will have a more relaxed CFL condition while also requiring fewer numerical resources because of the smaller grid. Using similar computing resources, the 2048 resolution ran approximately 40 times faster than the 8192×1024 resolution, while the 512×64 resolution ran approximately 5000 times faster than the 8192×1024 resolution! The latter value is a substantial increase in productivity.

We must keep in mind that this speed up is only usable before the simulation forms the shear instability (or after it has calmed down); otherwise the higher resolution is needed. Still, this duration isn't long as the increased resolution is only needed from $t = [16, 36]$ s and $t = [6, 21]$ s for the velocity perturbation and density perturbation cases, respectively. That is, for 40% and 30% of the simulation duration, respectively. Therefore, depending on the case, more than 60% of the simulation can be run with a speed-up of 40 or even 5000 times.

Three dimensional simulations comparable to those of the velocity perturbed cases were run with resolutions of $128\times64\times64$, $512\times256\times256$, and $1024\times512\times512$. The same delay in the formation (or non-formation) of the instability exists here as in the two-dimensional case. Refinement from the medium ($512 \times 256 \times 256$) to the high ($1024 \times 512 \times 512$) resolution occurred at $t = 16$ s.

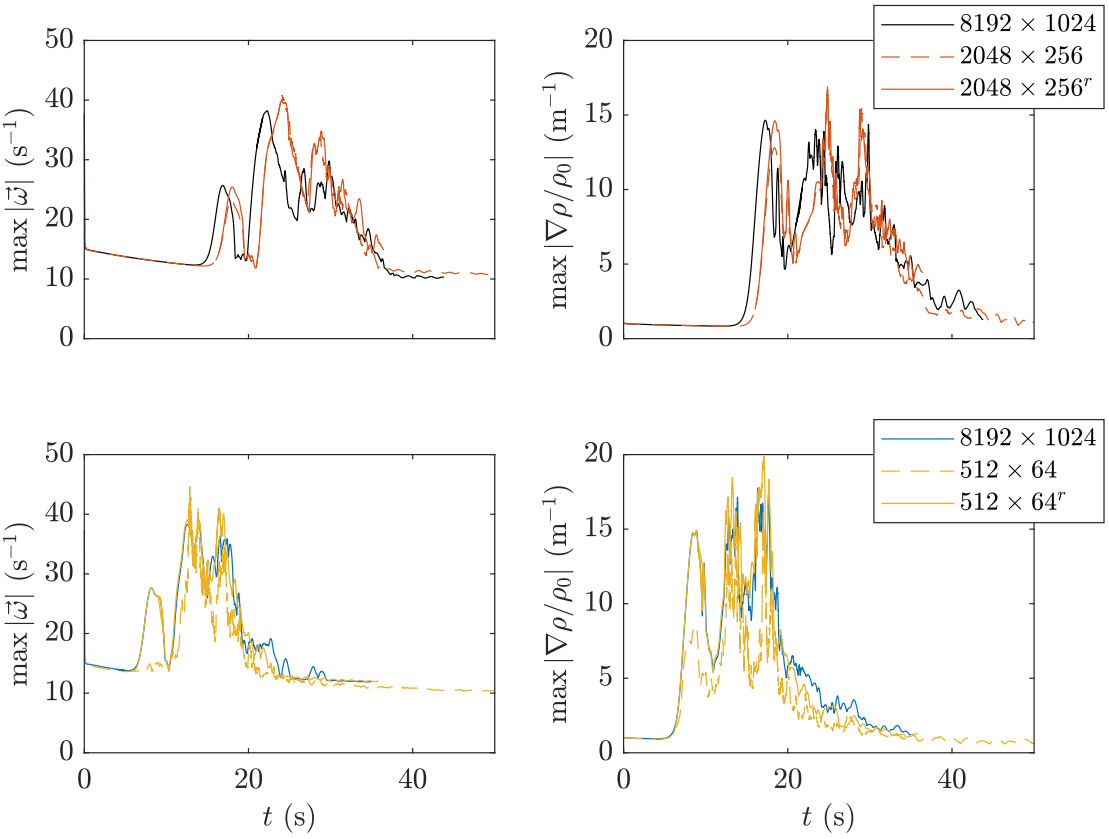

Figure 2.4: Maximum magnitude of vorticity (left column) and maximum magnitude of the density gradient (right column). Upper (lower) row is for cases initialized with velocity (velocity and density) perturbation. Superscript r is for the refined case.

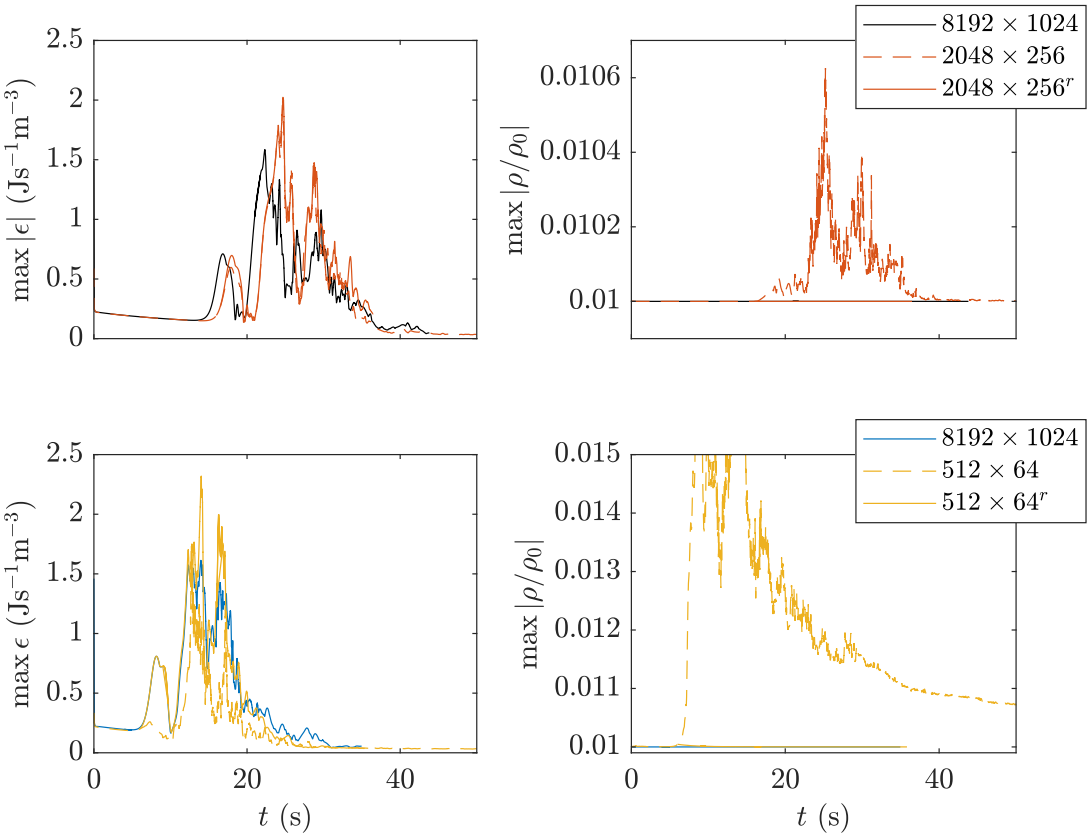

Figure 2.5: Maximum magnitude of dissipation (left column) and maximum density (right column). Upper (lower) row is for cases initialized with velocity (velocity and density) perturbation. Superscript r is for the refined case.

The initial formation of the billow ($t = [15, 20]$) is well resolved by the high resolution and the refined case, while being slightly under-resolved for the medium resolution. After $t = 21$ s the shear instability requires yet higher resolution. Another refinement is needed, though this has not been completed. The fact that multiple refinements or coarsenings might be needed should be remembered for future use.

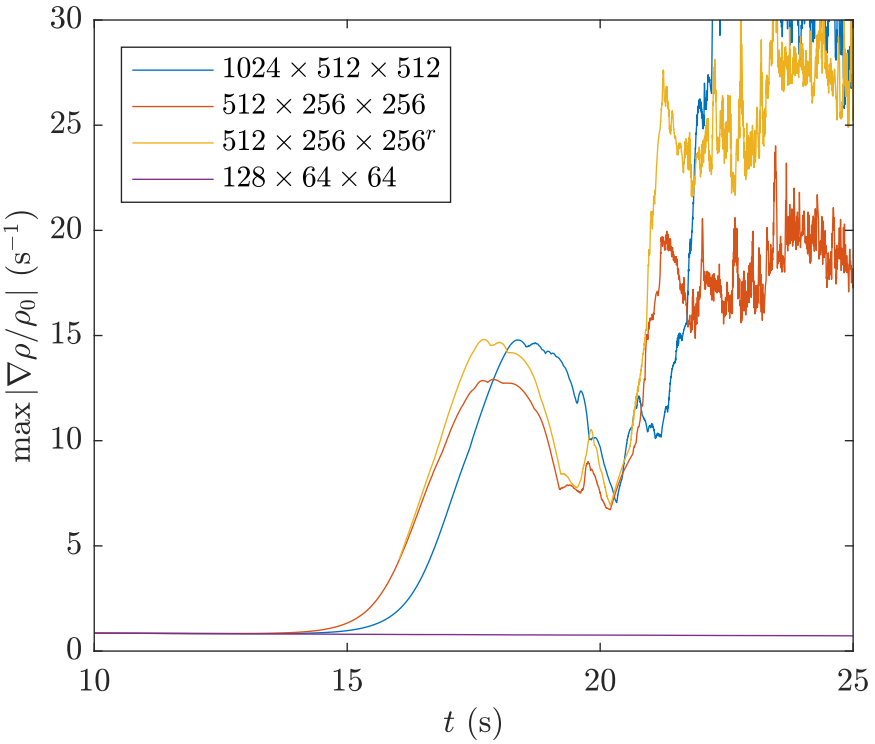

Figure 2.6: Maximum density gradient for three dimensional KH billows of various resolutions. The legend gives the grid resolution.

Lastly, we will look at the impact of refinement on a case studied in chapter 4. Two cases were run, one at resolution $8192 \times 512 \times 512$, the other at $2048 \times 256 \times 256$. The case is not important at this time, but rather the comparisons of the density fields some time after refinement at $t = 17$ s. The low resolution case (bottom panel) is only marginally resolving the smallest scales behind the mode-2 ISW. The high resolution and refined cases clearly resolve the density gradients in the aft of the wave. The refinement is quite suitable here.

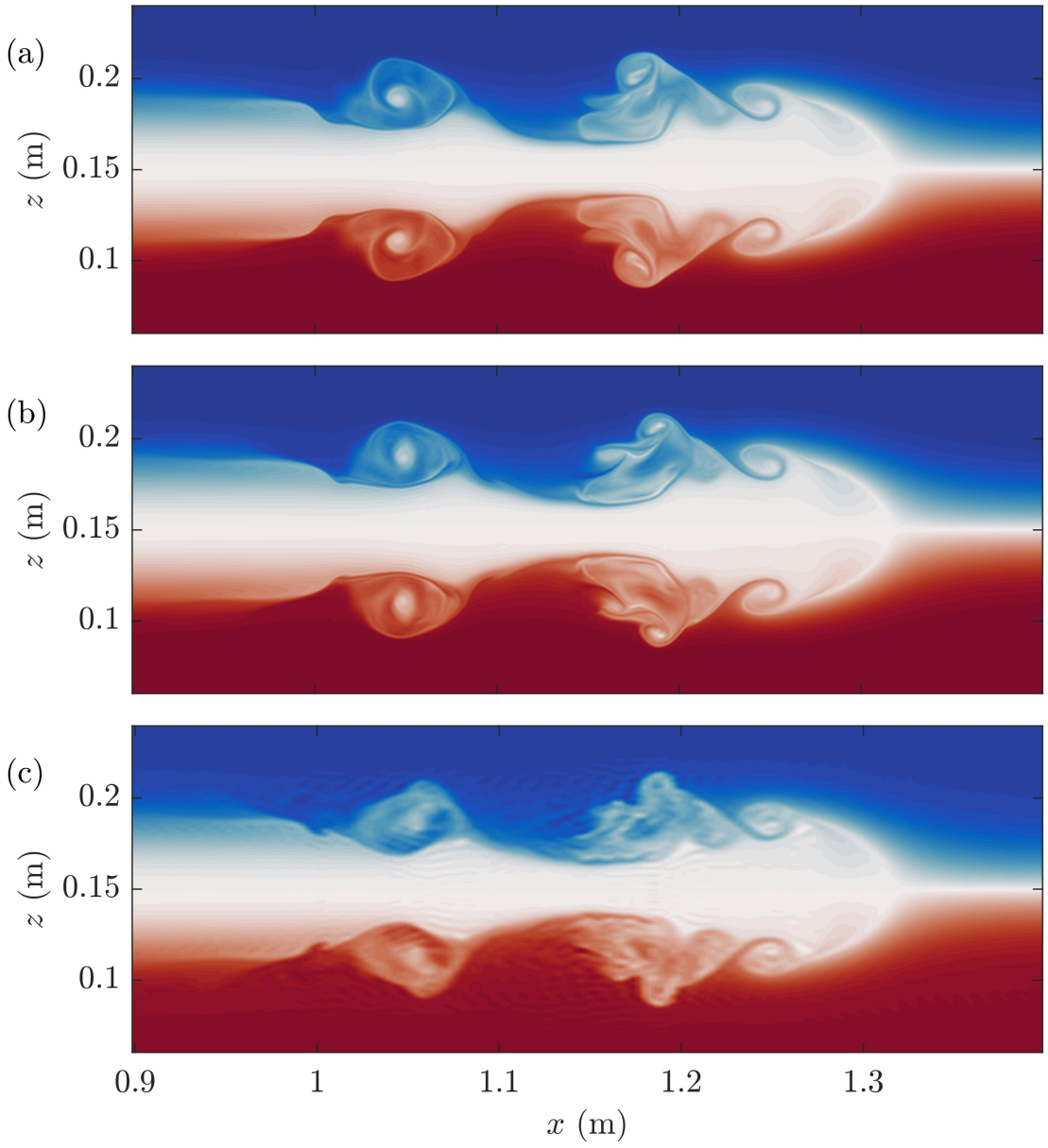

Figure 2.7: Density field at $t = 21$ s if cross-section $y = 0$ for a) high resolution b) refined low resolution, and c) low resolution.

There is no clear critical value that indicates when refinement or coarsening should occur for every type of simulation. Rather, the collective use of the diagnostics presented above gives a collection of hints for when this is needed. Sudden changes or random-appearing fluctuations, rather than reaching a particular value in these quantities, are good indicators for refinement.

The most vigorous cases of chapter 5 are ideal situations for the application of this refinement technique since the wave is calm for the majority of the simulation except for a short while during the interaction of the ISW with the topography. At the time of that study (and for all following results), the refinement code had not yet been written. The wave-hill interaction cases where a leading cause in the motivation for this refinement which was completed after (or nearly after) most simulations had been run. Though refinement has not been used in any of the following results, we have included it for the sake of documentation and proving it's applicability.

The refinement discussed in this section has been written in MATLAB and is capable of adjusting Fourier-type grids (those with periodic or free-slip boundary conditions). Though not difficult, refinement of Chebyshev grids has not been completed as of the writing of this thesis. If the grid is mapped (z-grid points are dependent on x) then refinement of Chebyshev grids, as described above, is possible in the vertical (z) and span (y) dimensions only. Along channel refinement, while possible, is complicated by the depth dependence along the horizontal grid. Refining in the vertical does not have this complication because there is only a scalar factor caused by the change in depth.

Chapter 3

Mass transport and core structure

The following chapter, except for section 3.7, has appeared as a publication in *Physics of Fluids* [Deepwell and Stastna, 2016]. Numerical simulations, analysis, and writing was completed by D. Deepwell with valuable guidance provided by M. Stastna.

3.1 Introduction

Two dimensional simulations give a good representation of the bulk properties of mode-2 internal solitary waves. However they are limited in the dynamics they describe because of the limitation on the degrees of freedom. Three dimensional simulations properly support the development of turbulence because of the ability for vortex stretching and tilting. This turbulence will change the interior of the wave core, possibly changing the mass transport.

Recently, Brandt and Shipley [2014] measured the mass transport of mode-2 ISWs under various forcing magnitudes. They classified the large amplitude waves into three categories: lower amplitude, large amplitude, and very-large amplitude. The lower amplitude waves were similar to those previously studied [Salloum et al., 2012, Terez and Knio, 1998] whereas the large amplitude waves experienced a "splitting" of the passive tracer within the core, and the very large amplitude had a smooth front with a turbulent aft. They found that the mass transport and wave amplitude were correlated with the forcing of the wave and the pycnocline thickness. It should be noted that in the context of finite depth experiments very large amplitude waves might be better described as a gravity current [Mehta et al., 2002], especially initially, though we continue with past tradition and refer to both as mode-2 ISWs, no matter how large or active the trapped core is, as "waves".

Two-dimensional, numerical simulations [Salloum et al., 2012] comparable to the experiments conducted by Brandt and Shipley [2014] have shown that the efficiency of transport increases with wave amplitude until the large amplitude waves begin to exhibit Kelvin-Helmholtz-like (KH) instabilities within their wakes. The presence of the KH instability disrupts the internal dynamics of the wave, reducing the transport of Eulerian tracers. This suggests that there exists an optimal transport regime upon which we shall shed additional light. It should be noted that the authors of Salloum et al. [2012] assumed symmetry across the mid-depth of the tank and hence simulated only half a tank, thereby forcing a particular type of wave core to exist. A correct interpretation of their results is that of transport by a mode-1 wave into a thin, stratified lower layer.

The remainder of this chapter is organized as follows. Section 3.2 describes the numerical techniques used to create and quantify a mode-2 ISW. Section 3.3 will investigate the wave generation with an emphasis on the instabilities within the wave. Section 3.4 will discuss the evolution of a small mode-2 ISW and its relation to observations made in the work of Brandt and Shipley [2014]. Section 3.5 will quantitatively discuss mass transport with a view to optimize it by changing the background stratification into a double pycnocline configuration. This focus on stratification dependence of mode-2 wave stability and efficiency of transport has not been explored in the literature in the past. Finally, section 3.7 will look at the impacts of moving the pycnocline away from the mid-depth.

3.2 Numerical methods and experimental configuration

In addition to the Navier-Stokes equations (1.1), a few passive tracers, T_i, where $i \in \{1, 1b, 2\}$, were included to measure transport of fluid parcels within the wave core. The associated partial differential equation to close the system is,

$$\frac{DT_i}{Dt} = \kappa_i \nabla^2 T_i, \tag{3.1}$$

where κ_i is the diffusivity of each passive tracer. The diffusivities, which remains unchanged between all simulations, are given in Table 3.1. The diffusivity of the active field, density, defines the Schmidt number, $Sc = \nu/\kappa_\rho$, and was allowed to vary. All simulations had a fixed viscosity of 2×10^{-6} m^2/s and the majority of simulations used $Sc = 1$. This is well below the physical value of 700 for a salt stratified fluid, but is more representative of a thermally stratified fluid ($Sc = 7$)

Table 3.1: Tracer diffusivities.

Tracer	T_1	T_{1b}	T_2
Diffusivity ($\times 10^{-6}$ m^2/s)	2	2	0.2

The formation of a mode-2 ISW is a result of the collapse of a region of constant intermediate density placed at one end of the channel (Figure 3.1). The width of this mixed region, L_m, controls the amplitude and wavelength of the resulting solitary-like wave. This generation mechanism is a common laboratory technique [Carr et al., 2015, Brandt and Shipley, 2014, Mehta et al., 2002, Sutherland, 2002] and is often used in numerical simulations [Salloum et al., 2012, Olsthoorn et al., 2013, Terez and Knio, 1998] as a comparison to physical experiments. While other techniques for inducing wave motion are accessible to simulations, such as adding fictitious forcing terms [Winters and Riley, 1992, Abdilghanie and Diamessis, 2011, Dohan and Sutherland, 2005], internal solitary and solitary-like waves are better represented through exact solutions of inviscid theory (i.e. the Dubreil-Jacotin-Long equation) or by situations in which they are allowed to dynamically develop from initial conditions (private communication with P. Diamessis).

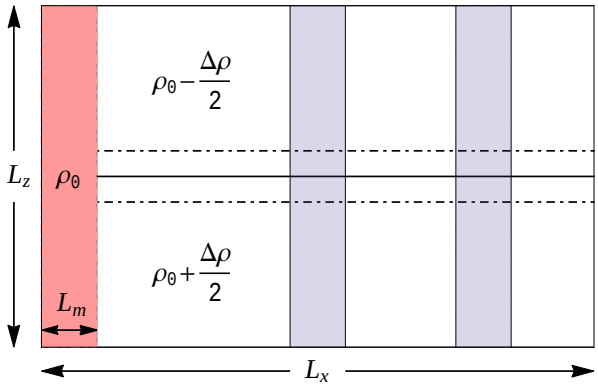

Figure 3.1: Initial tank configuration. Horizontal lines denote the location of the pycnocline centre (solid line) and pycnocline half-width (semi-dashed lines). One tracer field (T_{1b}, blue) is initialized as two vertical bands spanning the water column while two other tracers (T_1, T_2, both red) are initialized within the intermediate region at the far left of the channel.

The tracer fields, T_1 and T_2, of different molecular diffusivities were placed in the intermediate region to be encapsulated by the forming mode-2 wave (red band in Figure 3.1). Both tracers were placed at the same location to investigate the effect of a material's diffusivity on its transport. To the best of our knowledge, the use of multiple, diffusive

tracers in mass transport experiments has not yet been examined. The impact on transport due to a material's diffusivity is still an open question with possible implications within both biological and chemical oceanography.

The tracer T_{1b} was initialized as two vertical bands further down the tank with centres at $x = 0.5$ m and $x = 2$ m and a width of 10 cm each. These columns provide a meaningful description of the impact a mode-2 wave has on the water-column and acts as a means to measure the trapping capability of the developing wave. They are the numerical equivalent of the use of potassium permanganate tracers in physical experiments.

The computational domain was a long, narrow, rectangular channel with the dimensions and resolution given in Table 3.2. Since the stratification and instabilities form preferably in the span-wise and vertical dimensions, the resolution in these dimensions is approximately twice that of the along channel (x). Ideally, all dimensions would have similar resolution, but the along channel dimension was reduced for efficiency of computation. All simulations are three-dimensional with free-slip boundary conditions and constant grid spacing through the use of cosine transforms on account of the spectral method. Other grid spacings and tank dimensions, such as Chebyshev grids in the vertical in conjunction with a no-slip boundary condition, have been tested but we have found that the combination reported in this work provide a reasonable CFL restraint while resolving all the small-scale dynamics. The internal dynamics of the mode-2 wave were comparable whether the boundary conditions were no-slip or free-slip.

Table 3.2: Tank dimensions.

L_x (m)	L_y (m)	L_z (m)	N_x	N_y	N_z	Δx (mm)	Δy (mm)	Δz (mm)
4	0.1	0.3	4096	192	512	0.98	0.52	0.59

We have tested our resolution by comparing the grid spacing to the smallest structures in each field. Since the ISW is generated via the collapse of an intermediate fluid, the finest structures exist for a short period only during the emergence of the mode-2 wave from the collapse. During this time, the lowest diffusivity field (usually T_2 since most cases have low Schmidt number) has the smallest structures: we have ensured that each structure is well resolved. For low Schmidt number cases, the smallest structures in T_2 have approximately 20 grid points across them. For $Sc = 40$, the density and T_2 both have approximately 10 points per fine structure. This is more than enough for the spectral method to resolve the features. As the flow continues to develop, these small structures eventually surpass twice the resolution during the collapse. Therefore, for the majority of the simulation time and

for nearly all the fields we are over-resolving the structures because of these short-lived features which exist primarily in the T_2 field.

In contrast to most previous numerical simulations [Salloum et al., 2012, Terez and Knio, 1998], we have used a three-dimensional domain without making the symmetry argument at the mid-plane. The three-dimensionality allows turbulent mixing processes to develop realistically while the exclusion of the symmetry argument enables the core the freedom to form without the presence of a restricting boundary. Observation of mode-2 ISWs are often associated with mode-1 ISWs and wave-trains [Shroyer et al., 2010], which often lead to a destruction of the wave core and cause an energy transfer to the lower wave mode. In laboratory experiments, symmetry is broken by moving the pycnocline centre away from the mid-depth [Carr et al., 2015, Olsthoorn et al., 2013].

The three-dimensionality is especially important in the aft instabilities seen by Carr et al. [2015], Brandt and Shipley [2014] and Salloum et al. [2012]. Over-turning caused by the generation mechanism leads to turbulence which may have a profound impact on the mass transport capabilities of the wave. Overall, the absence of these simplifying assumptions result in a longer computation time due to the greater number of grid points necessary to maintain a high resolution of the smallest features. To break symmetry and enable span-wise instabilities to form, the flow is initialized with a white noise perturbation to an otherwise motionless velocity field with a maximum speed on the order of a millimetre per second.

The initial background stratification consisted of one of two types: a single pycnocline consisting of a typical hyperbolic tangent profile or a double pycnocline consisting of two hyperbolic tangent profiles. The single hyperbolic tangent profile is given by

$$\bar{\rho}(z) = \rho_0 - \frac{\Delta\rho}{2} \tanh\left(\frac{z - L_z/2}{h}\right), \tag{3.2}$$

where $\Delta\rho$ is the density difference between the top and bottom layers of the stratification, and h is the pycnocline half-width. The double pycnocline is given by

$$\bar{\rho}(z) = \rho_0 - \frac{\Delta\rho}{4} \tanh\left(\frac{z - (1-\zeta)L_z/2}{h}\right) - \frac{\Delta\rho}{4} \tanh\left(\frac{z - (1+\zeta)L_z/2}{h}\right), \tag{3.3}$$

where ζ denotes the separation of the pycnoclines. When $\zeta = 0$ equation (3.2) and (3.3) are equivalent. Stratifications given by equation (3.3) arise from the repeated use of a single pycnocline in physical mode-2 wave experiments [Sutherland, 2002].

Generalizing from previous studies [Salloum et al., 2012, Stamp and Jacka, 1995, Carr et al., 2015] for double pycnoclines, the characteristics describing the wave were calculated

from the displacement of the $\bar{\rho}(L_z/2 \pm h^*)$ isopycnals from their original depth, where $h^* = \zeta L_z/2 + h$ (Figure 3.2). We refer to the $+h^*$ and $-h^*$ isopycnals as the upper and lower isopycnals, respectively. The amplitude, a, is the average of the maximum displacement of these isopycnals.

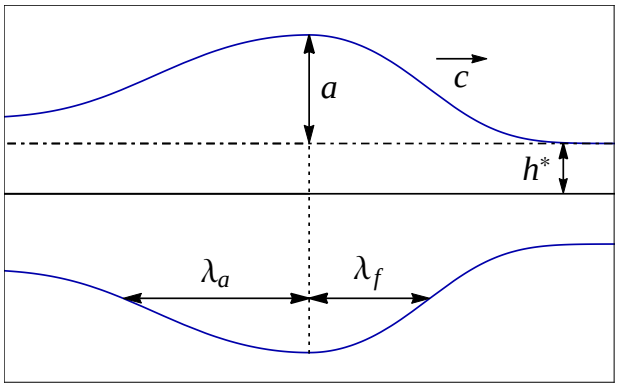

Figure 3.2: Schematic of parameters for a rightward moving mode-2 wave.

Because of KH billows and mixing, mode-2 waves do not necessarily display fore-aft symmetry and so two different wavelengths were defined: the fore (λ_f) and aft (λ_a) wavelengths. Respectively, these are the distances from the location of maximum amplitude to half-maximum at the front and rear of the mode-2 wave. This was done on both the upper and lower isopycnals to define the area on which to measure the tracers carried by the wave, the accurate measurement of which is crucial to correctly quantifying the mass transport capabilities of the wave. No asymmetry exists in the vertical when the pycnocline is at the mid-depth. However, when the layers are of unequal depths, the amplitudes above and below the pycnocline are no longer equal (see section 3.7). Though not investigated, changing the stratification to be asymmetric across the mid-depth (such as changing h^* above and below the pycnocline) will also break vertical symmetry of the wave.

Consistent with previous literature [Salloum et al., 2012, Stamp and Jacka, 1995, Carr et al., 2015], we define the characteristic length and velocity scales as the pycnocline half-width, h, and the mode-2 linear long wave speed [Benjamin, 1967],

$$c_0 = \frac{1}{2}\left(\frac{gh\Delta\rho}{\rho_0}\right)^{1/2},$$

respectively. Therefore, the Reynolds number is $Re = c_0 h/\nu$, though we note that this estimate does not account for the wave amplitude. The parameters of the three-dimensional

simulations conducted in this work are listed in Table 3.3. Three principal parameters were varied: the Schmidt number, the width of the collapse region, L_m, and the separation of the double pycnocline, ζ.

Table 3.3: Simulations parameters.

Case	Description	L_m (cm)	ζ	$\Delta\rho/\rho_0$	h/L_z	Sc	Re
1	$Sc = 1$	6	0	0.005	0.05	1	102
2	$Sc = 2$	6	0	0.005	0.05	2	102
3	$Sc = 20$	6	0	0.005	0.05	20	102
4	$Sc = 40$	6	0	0.005	0.05	40	102
5	$L_m = 3$ cm	3	0	0.005	0.05	1	102
6	$L_m = 9$ cm	9	0	0.005	0.05	1	102
7	Wide pyc.	6	0	0.005	0.10	1	288
8	$\zeta = 0.10$	6	0.10	0.005	0.05	1	102
9	$\zeta = 0.12$	6	0.12	0.005	0.05	1	102
10	$\zeta = 0.12$ $Sc = 20$	6	0.12	0.005	0.05	20	102
11	$\zeta = 0.15$	6	0.15	0.005	0.05	1	102
12	$\zeta = 0.20$	6	0.20	0.005	0.05	1	102

3.3 Mode-2 ISW generation

Before varying the parameters of the experimental configuration, we begin with a brief investigation into the generation and progression of the mode-2 ISW in the base case (Case 1). We will also make a comparison to a high Schmidt number case (Case 4, $Sc = 40$). This will allow us to extrapolate the results of other configurations to their high Schmidt number equivalents.

The non-dimensional depth of the intermediate fluid, $L_z/h = 20$, is comparable to a couple of cases discussed in Brandt and Shipley [2014]. The vertically narrow aspect ratio of the intermediate region forms a large area over which baroclinic vorticity is produced compared to previous studies [Brandt and Shipley, 2014, Olsthoorn et al., 2013, Carr et al., 2015]. The implications of this fact have, until now, not been examined in depth since previous studies typically had wide aspect ratios for the intermediate region and in laboratory experiments the gate release likely dominates local vorticity dynamics.

Figure 3.3 displays the formation of a single mode-2 ISW from the lock-release method for a six centimetre wide intermediate region. The red and yellow region represents the concentration of tracer T_1, with a value of 1 being the maximum concentration. The behaviour of tracer T_2 is qualitatively similar and so has not been plotted. The white contours are the upper and lower isopycnals and the black line is the pycnocline centre.

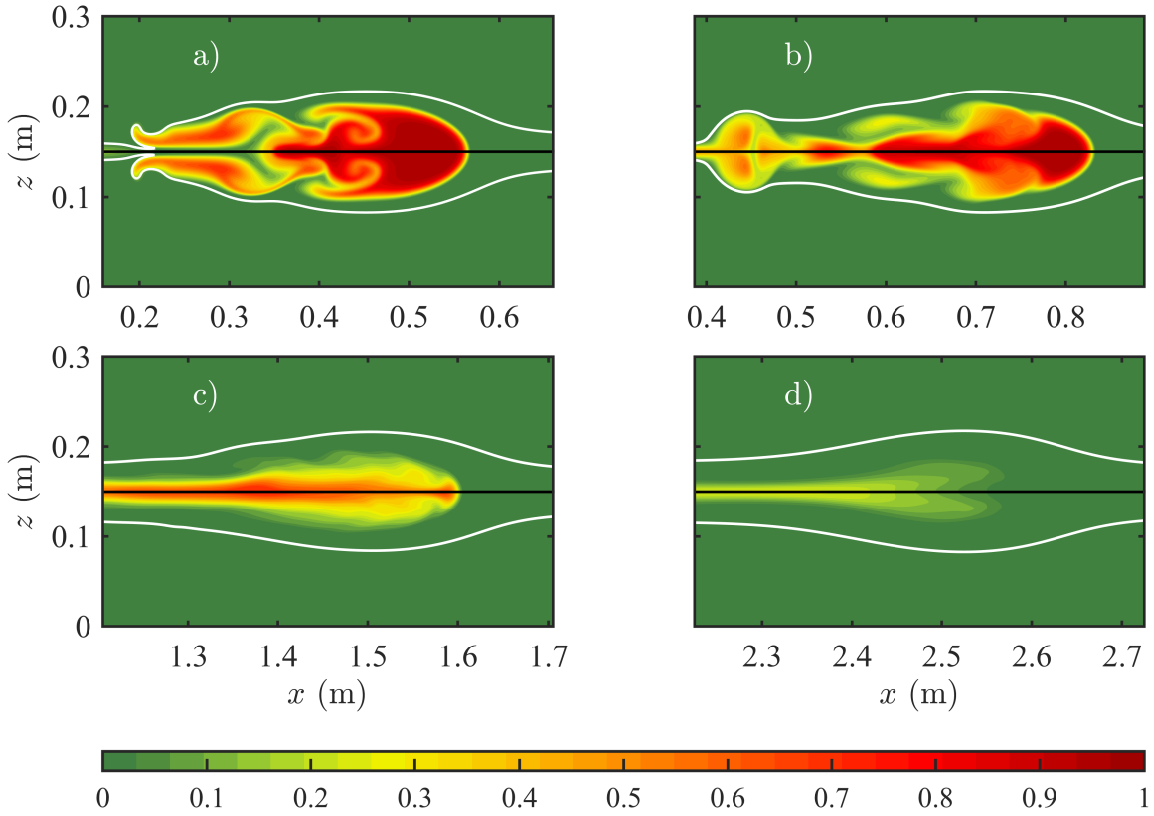

Figure 3.3: Evolution of tracer T_1 for Case 1 at $t =$ a) 20 s b) 30 s c) 60 s d) 100 s. White contour lines show pycnocline half-width contours and the black line is the pycnocline centre.

Initially the gravity current intrusion contains all of the tracer. However, the high vorticity generated by the collapse soon forms a vortex dipole in the aft of the gravity intrusion leading to overturning, strong turbulence, and ultimately a reduction in the tracer transport. We call this the external vortex pair because it leaves the wave carrying a fraction of T_1 ($x \approx 0.3$ m and $x \approx 0.45$ m in Figure 3.3(a) and (b), respectively). While within the wave, this vorticity creates a vortex pair of opposite orientation which remains

in the wave ($x \approx 0.45$ m and $x \approx 0.7$ m in Figure 3.3(a) and (b), respectively). We call this the interior vortex pair as it remains within the wave throughout the simulation. Further discussion on the role of this interior vorticity on mass transport will follow in section 3.4.

During the wave formation, the front of the gravity intrusion remains span-wise invariant. The turbulence within the wave aft slowly grows in magnitude and areal extent, until it encompasses the entire interior of the wave at approximately $t = 60$ s at which time the transients of formation have decayed away. From then on, the non-dimensional amplitude and wavelengths both decrease smoothly, indicating that the wave is not in the weakly non-linear regime.

Figure 3.4 shows the trapping of tracer T_{1b} by the mode-2 wave. As the wave travels through the column, the majority of the dye flows around and past the wave. A small portion reaches the wave interior by either advection (near the aft) or diffusion (near the front). Once in the core, the dye is transported for some time before eventually leaving out the aft of the wave. Figure 3.4 (b) and (d) clearly show the shear in the water-column associated with the passage of the mode-2 wave.

The three-dimensionality of the simulations enable the study of the span-wise structure of the waves. Figure 3.5 (a) shows isosurfaces of density and T_1 at $t = 26$ s, roughly midway through the mode-2 formation. The blue isosurface shows the density contours at $\rho = \rho_0 \pm \Delta\rho/4$, while the red isosurface is half the initial maximum of tracer 1, ie. $T_1 = 0.5$. The ISW exhibits a smooth wavefront with an unstable lee at this time. The exterior vortex dipole generated during the wave formation is clearly seen near $x = 0.375$ m and there is overturning at the aft of the mode-2 wave at $x = 0.5$ m.

Tracer T_2, also initialized within the intermediate region but with a lower diffusivity, reveals finer structures within the wave (Figure 3.5 (b)). T_2 has the same general features as T_1, but the variability within the dye at the rear of the wave is much more chaotic. T_2 also reveals the interior vortex pair at $x \approx 0.65$ that travels forward through the mode-2 core, seeding the lee instability. This can partly be seen in Figure 3.3(a) before it degrades in Figure 3.3(b). This added motion disturbs the structure of the interior of the mode-2 wave core and eventually reaches the front of the wave around $t = 60$ s, whereby destroying all span-wise symmetry of the wave. We suggest that removing this vortex pair will lead to increased transport. Section 3.5 discusses the use of a double pycnocline stratification which accomplishes this purpose.

The impact of the interior vortex pair is clearly seen in the cross-section of the density and tracers at $x = 0.6$ m at $t = 26$ s (Figure 3.6). The $Sc = 1$ case (first row) displays plumes which resulted from overturning caused by the interior vortex pair. The $Sc = 40$ case (second row) has no such plumes, but rather has more chaotic features. This

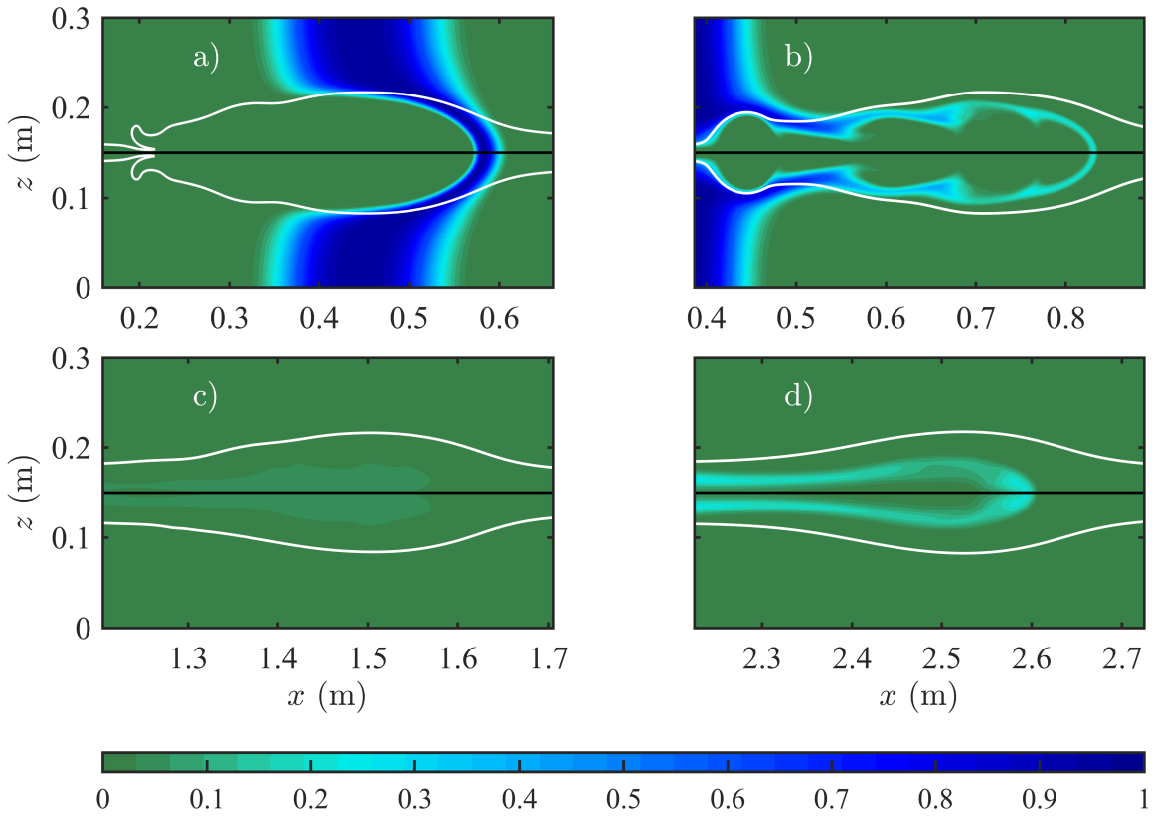

Figure 3.4: Evolution of tracer T_{1b} at t = a) 20 s b) 30 s c) 60 s d) 100 s. Two bands spanning the entire water-column are centred at $x = 0.5, 2$ m. Black and white contour lines are equivalent to those in Figure 3.3.

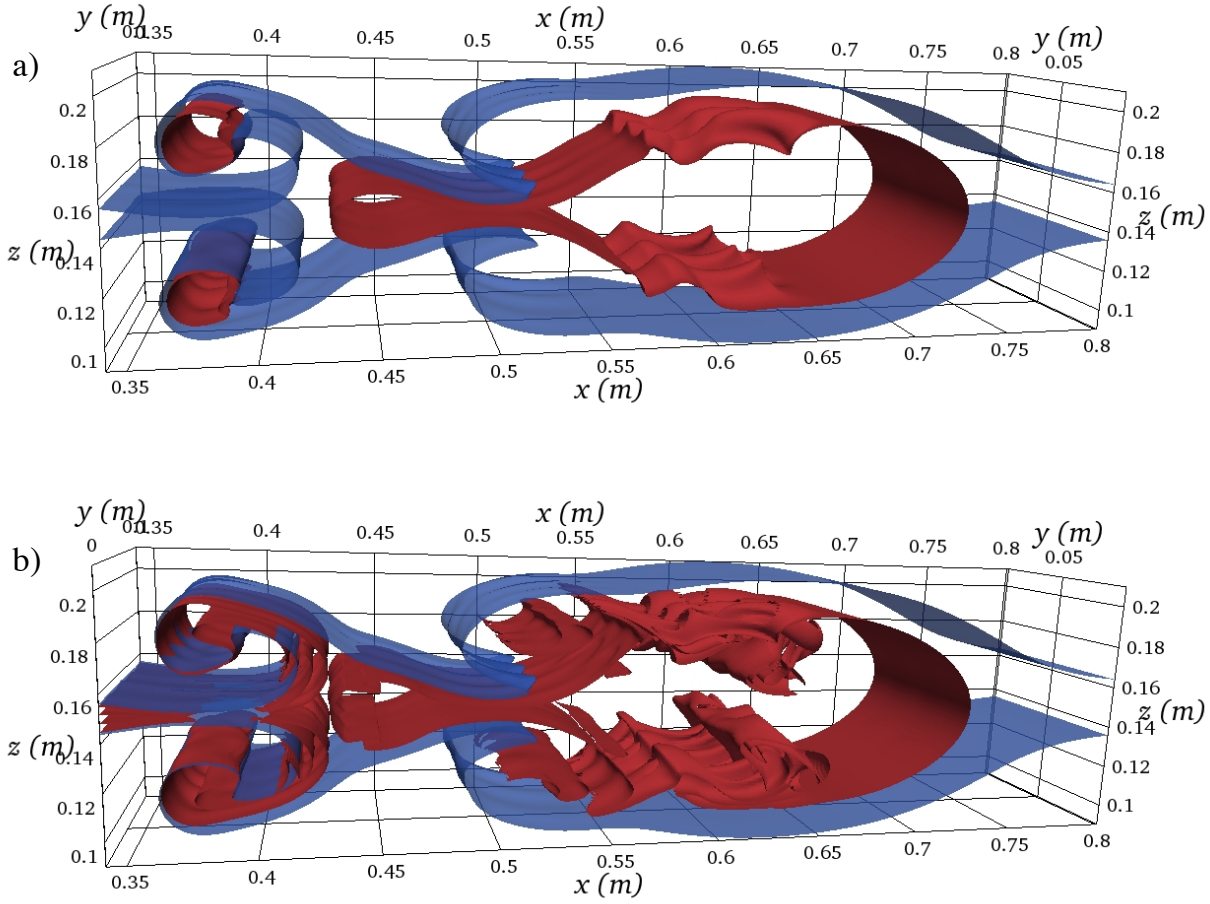

Figure 3.5: Isosurfaces of density (blue) and a) T_1 (red) and b) T_2 (red) at $t = 26$ s. Contours are at $\rho = \rho_0 \pm \Delta\rho/4$, $T_1 = 1/2$, and $T_2 = 1/2$.

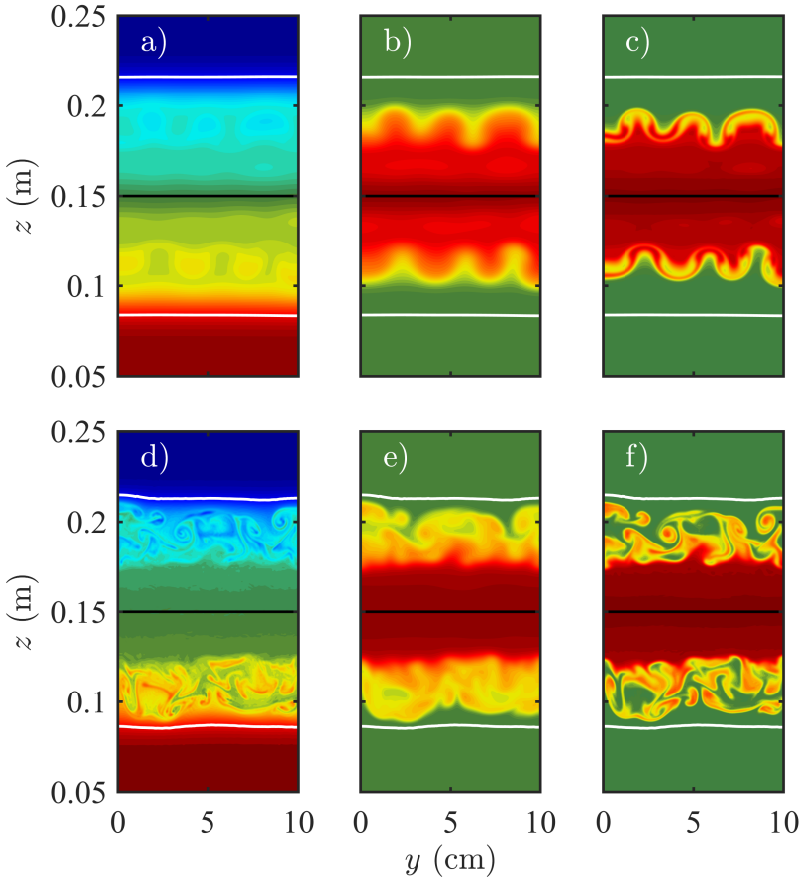

Figure 3.6: Span-wise distribution of density and tracers at $t = 26$ s and $x = 0.6$ m for $Sc = 1$ (top row), and $Sc = 40$ (bottom row). The columns are (a,d) density, (b,e) T_1, and (c,f) T_2. White lines show upper and lower isopycnals and the black line is the pycnocline centre.

decoherence weakens the interior vortex dipole responsible for core degeneration. The mass transport will thus increase with Schmidt number because the dipole strength weakens with Schmidt number. We reserve the proof of this assertion to section 3.5 which discusses the mass transport of all cases in greater detail.

Though not presented, structures in the velocity fields are always comparable in size to those in T_1 since the viscosity and T_1 diffusivity are equivalent. We repeat then that the finest structures exist within T_2 and in the density field for high Schmidt number. There are 192 points which span the width of the tank and provide approximately 10 points per feature in these fields for the $Sc = 40$ case. The vertical has 512 points and is therefore better resolved.

3.4 'Pac-man' and wave core dynamics

The width of the intermediate region is directly associated with the size of the resulting mode-2 ISW. Here we will contrast the previously discussed case of a 6 cm wide mixed region with a smaller 3 cm wide region. This smaller amplitude case will highlight the internal dynamics of the wave and the impact this has on the mass transport.

Compared to the wave formed by a six centimetre mixed region, the wave is now considerably smaller (Figure 3.7). The exterior vortex dipole is therefore much more dominant and remains within the wave longer (cf. Figure 3.3 (a)). This vortex pair leaves around $t = 38$ s, more than double the duration of the $L_m = 6$ cm case ($t = 14$ s). The composition of the core has been drastically altered by this vortex pair. A very noticeable impact is a large reduction of the trapped tracer, especially as the external vortex pair leaves the core. Later on, at $t = 100$ s, having travelled less than 2.5 m, the core is essentially void of T_1.

In this case we find features of a different type of mode-2 wave which has been called the 'Pac-man' wave (Figure 3.7(c)). First emphasized by Brandt and Shipley [2014], the 'Pac-man' derives it's name from the tracer having a distinct open 'mouth' structure similar to the classic arcade character. The 'Pac-man' structure had previously been seen by Schmidt [1998], Maxworthy [1980], and Terez and Knio [1998] (while also containing a tongue), but was not given any special consideration since most experiments showed the same structure.

A few distinctions should be made about the current 'Pac-man' and the one seen by Brandt and Shipley [2014]. First, the form seen by Brandt and Shipley [2014] displayed a much narrower and deeper 'mouth', as opposed to the fairly wide 'mouth' seen here. Second, the present 'mouth' does not have a sharp perimeter clearly marking the edge of the tracer field. Both of these differences are attributed to the large diffusivity compared

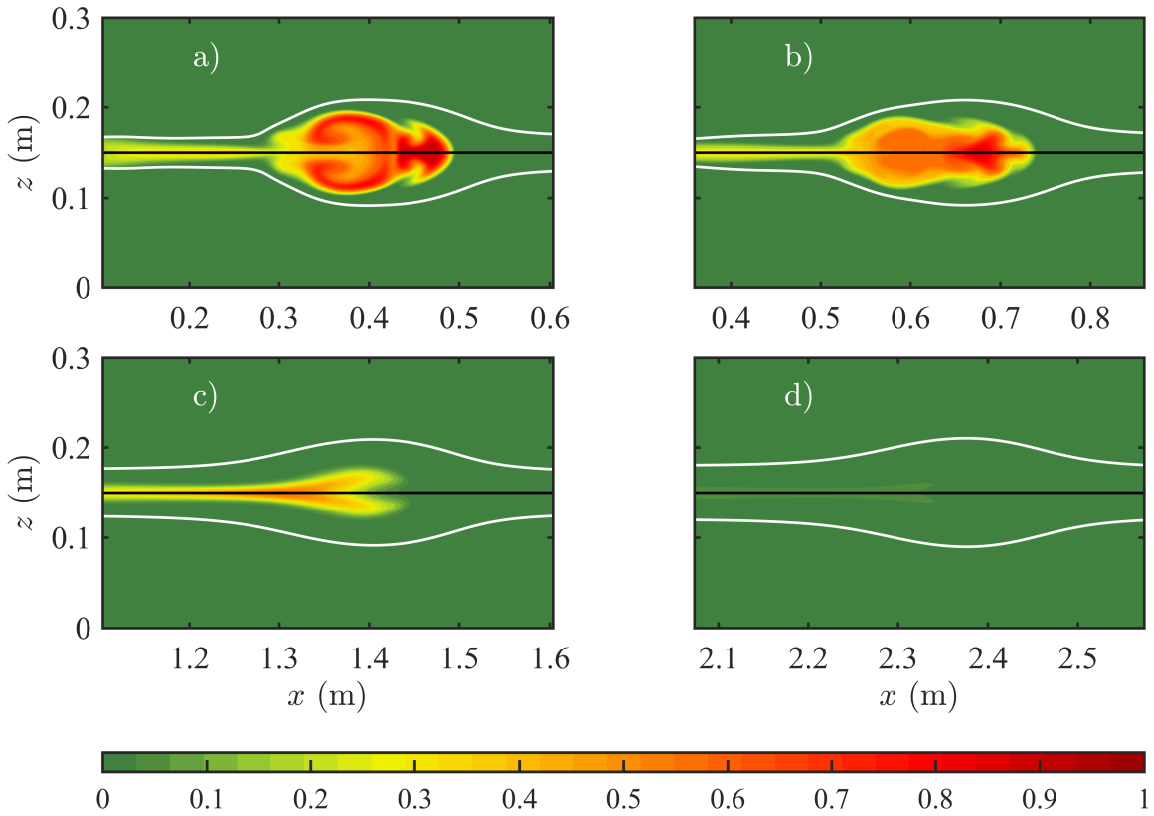

Figure 3.7: Evolution of tracer T_1 for $L_m = 3$ cm at $t =$ a) 20 s b) 30 s c) 60 s d) 100 s. White contour lines show pycnocline half-width contours and the black line is the pycnocline centre.

to the physical value. A closer approximation to the physical value is realized in the T_2 field (Figure 3.8(f)), with a diffusivity an order of magnitude smaller than T_1.

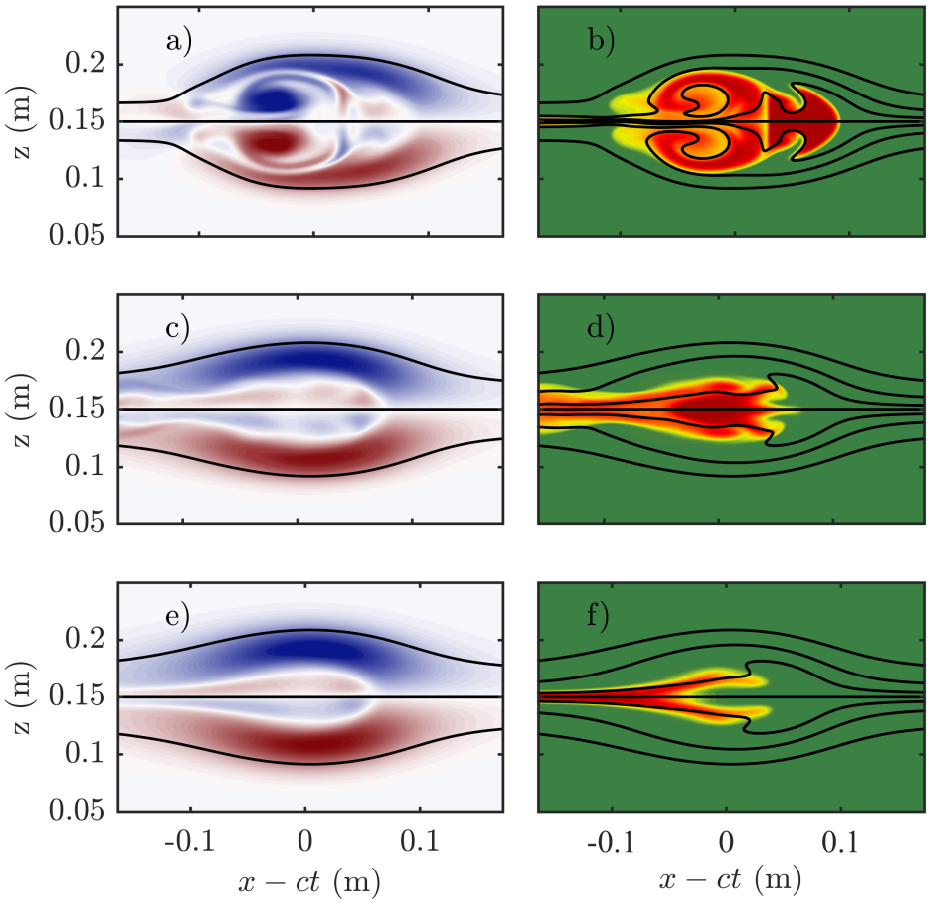

Figure 3.8: Span-wise vorticity (left column) and T_2 (right column) for Case 9 at $t =$ (a,b) 20 s, (c,d) 40 s, and (e,f) 60 s. Outermost black lines are the upper and lower isopycnals. Vorticity colour scheme ranges between [-2.5,2.5] s^{-1} in a) and [-1.25,1.25] s^{-1} in c) and e).

The span-wise vorticity field (Figure 3.8) reveals that the distinctive open mouth shape in the tracer field is a result of the internal vortex pair. Since the intermediate region was quite small in volume, the resulting exterior vortex dipole (rear half of the mode-2 wave in Figure 3.8(a)) was quite large compared to the size of the wave. As before, while present within the wave the exterior vortex dipole created the interior vortex pair of opposite orientation (front half of the mode-2 wave in Figure 3.8(a)).

This opposing interior vorticity pair acted to slow the forward horizontal motion of fluid along the pycnocline while partially increasing the forward velocity slightly away from the pycnocline centre. A vertical transect through the wave centre (not shown) clearly shows a local minimum in the horizontal velocity. Once the exterior dipole has left the wave, the opposing vorticity occupies the entire centre portion of the wave, further enhancing the loss of material from the pycnocline centre (Figure 3.8(c)-(f)). Later (Figure 3.8(f)), the 'Pac-man' is fully formed with a wide, deep mouth.

This leads to the twin questions, 'is this vorticity structure consistent for all amplitudes?', and 'how much does this affect the mass transport?'. The work by Schmidt [1998] and Terez and Knio [1998] demonstrates that the velocity distribution like that of Figure 3.8 is predominant. A review of our work with single pycnoclines has also shown a prevalence of these features. For example, Figure 3.3(d) shows the 'mouth' beginning to form, even though the colour scale does not make it clear due to the small extent of the tracer concentration. However, changing the colour scale to highlight the difference from the background produces a figure similar to Figure 3.8(f).

A two-dimensional simulation with $L_m = 12$ cm (not presented) also clearly shows the 'Pac-man' configuration even though the wave is of very large amplitude. This indicates that the internal dynamics are not strongly tied to the amplitude of the wave but to some other mechanism. Changing the mechanism will also likely change the transport efficiency: see the discussion of theoretical conceptions of trapped cores for mode-1 waves below. For example, Terez and Knio [1998] commented on the differences in the vorticity structure of waves formed by separate laboratory generation techniques. Stamp and Jacka [1995] formed mode-2 waves by forcing fluid through an opening in a wall located at the pycnocline. Since no collapse occurs, no vortex dipole forms and the opposing vorticity might be avoided.

Our numerical model, however, is unable to replicate complex geometries and therefore the most realistic generation mechanism that is realizable is a lock-release. As the lock-release technique is very common in the literature [Brandt and Shipley, 2014, Schmidt, 1998, Maxworthy, 1980, Terez and Knio, 1998, Carr et al., 2015], we are describing the internal wave dynamics of these experiments so that they can be improved upon in the future. The lock-release method results in substantial vorticity generation (Figure 3.8), which should be minimized to form a more transport-promoting ISW. This is achieved by reducing the density difference between the two layers, using a thicker pycnocline, or changing the aspect ratio of the intermediate region.

Before exploring an adjustment to the stratification, we will make a few comments on tracers. In this case we saw that the tracer quickly depleted from the wave. Brandt and

Shipley [2014] separated their mode-2 wave types based upon the dimensionless amplitude of tracer. Using the tracer is likely valid only for idealized experiments using a short tank, when the diffusivity is small (this is natural in experiments, but simulations with the true value of Sc are, to the best of our knowledge, unavailable), and when the pycnocline is sufficiently small to sustain mass transport. Only then is it possible that the tracer will give an accurate representation of the dynamics within the waves. Sutherland [2002] qualitatively found that even with small diffusivities the mass transport was greatly reduced as the pycnocline grew (see also Mehta et al. [2002]). We suggest that caution be taken when using tracers as a metric to describe mode-2 waves.

That said, the dye may still provide qualitative insight into the structure of the core region. In particular, if a coherent, trapped core exists in a stable, semi-steady state, the transport can be expected to be the most efficient. On the other hand, trapping of material by the core requires a means for material from outside of the core to move into it. This is impossible if the core is perfectly steady, as in the original conception of mode-1 waves with cores [Derzho and Grimshaw, 1997], but may occur in the aft region of an active core (see Figure 3.4(b)).

3.5 Mass transport

Thus far we have discussed the formation process of a single, solitary mode-2 wave in a variety of different configurations with a single pycnocline. We have stressed the qualitative features of mass transport but have said nothing quantitative. To do so, we define the amount of tracer within the core to be

$$T_{\text{core}} = \frac{1}{|V^*|} \int_{V^*} T_i dV,$$

where V^* is the volume bounded by the upper and lower isopycnals and the fore and aft wavelengths defined in section 3.2, and $|V^*|$ is the volume of this region.

The scaled core mass, $\widetilde{T}_{\text{core}} = T_{\text{core}}/T_{\max}$, for single pycnocline configurations (Figure 3.9(a) and (b)) are qualitatively different from double pycnocline configurations (Figure 3.9(c)). Single pycnocline cases have an approximately constant rate of mass loss, while double pycnoclines may experience a change in the discharge rate.

Three separate groups of results are represented in Figure 3.9, they are: a) the base simulation with varying Schmidt number, b) various intermediate widths, and c) double pycnoclines. Solid and dashed lines represent the scaled core mass for T_1 and T_2, respectively.

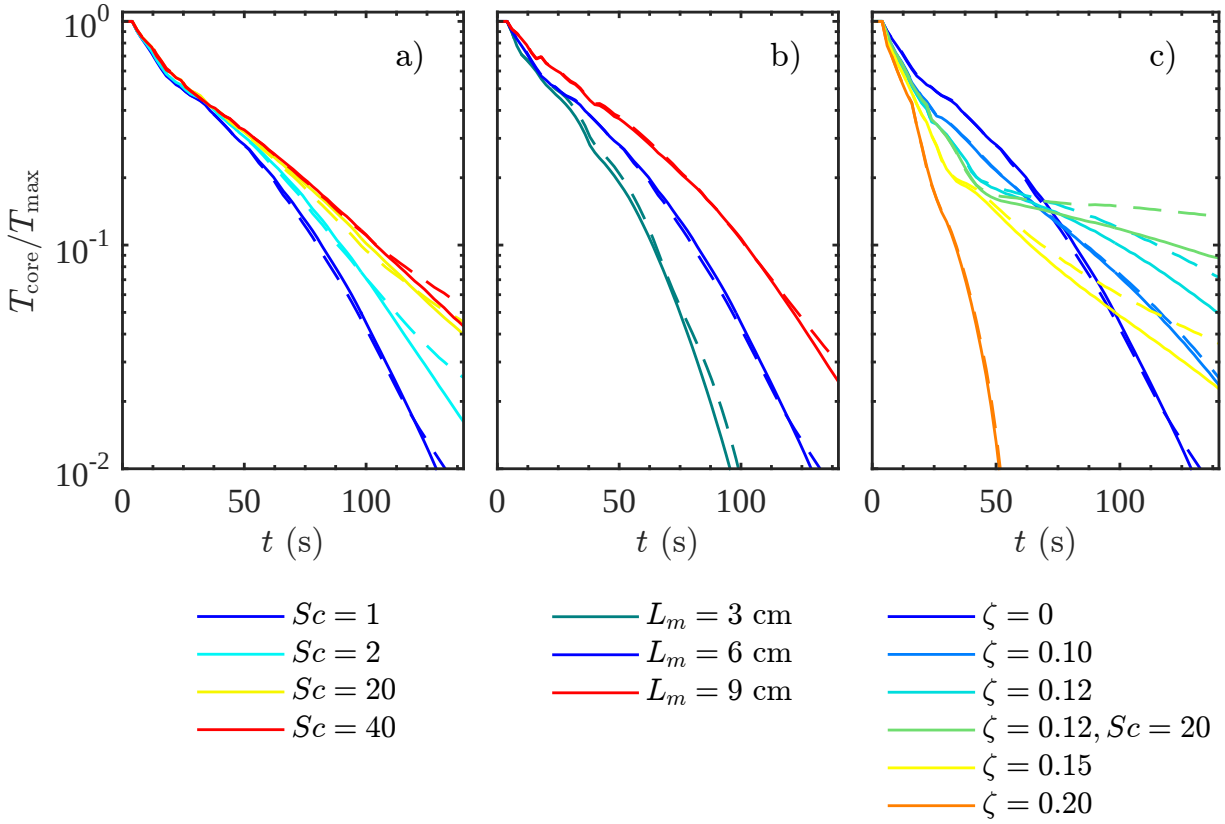

Figure 3.9: $T_{\mathrm{core}}/T_{\mathrm{max}}$ for a) the base simulation with various Schmidt numbers, b) single pycnoclines, and c) double pycnoclines. Dashed lines are $T_{\mathrm{core}}/T_{\mathrm{max}}$ for T_2, and legends describes the primary descriptor of each case. The dark blue line in each subplot is the same simulation (Case 1).

Overall, the mass transport is quite poor. This is surprising since the wave amplitude is greater than the critical amplitude for transport in all cases [Terez and Knio, 1998]. The poor transport efficiency is also evident in the higher decay rates of $\widetilde{T}_{\text{core}}$ compared to those often seen by Brandt and Shipley [2014] and Salloum et al. [2012]. Part of the discrepancy is in the differing definitions of mass within the wave core. Plots of T_{core} with a linear axis, however, match well to high Reynolds number cases in Salloum et al. [2012]. Therefore, we suggest that our Reynolds number estimate yields lower values than those seen by Salloum et al. [2012].

As alluded to in section 3.3, the mass transport increases with Schmidt number since a smaller density diffusivity causes finer structures to persist which causes a decoherence of the instability-inducing vortex pair. There is a reasonable increase in transport efficiency between $Sc = 1$, $Sc = 2$, and $Sc = 20$. The $Sc = 40$ case is only marginally more efficient than $Sc = 20$, indicating a limit to the strength in which the decoherence from a smaller diffusivity affects the interior vortex pair.

The mass transport also increases with the width of the intermediate region, which is a proxy for the wave amplitude (Figure 3.9(b)). The weakest transport for a single pycnocline occurred in the 3 cm wide intermediate region (Case 9, green line). The core tracer smoothly decays to 1% within 100 s. This expeditious discharge is a result of the dominant interior vorticity pair associated with the 'Pac-man' formation (section 3.4). Larger waves, such as those from $L_m = 6$ and 9 cm, also have this adverse interior vorticity, but since the ratio of vortex dipole size to wave size is smaller, the transport is affected to a lesser extent.

In these two parameter studies the mass transport has not simply been explained by the magnitude of the wave amplitude but rather the strength and type of internal dynamics within the wave core in comparison to the wave as a whole. This prevailing trends leads us to believe that double-pycnocline stratification can optimize mass transport since it will result in calmer internal dynamics.

In contrast to single pycnoclines, double pycnoclines may have two distinct mass discharge phases. The first is the release of all excess fluid which is not within the wave core, while the second is the release of fluid from within the core due to the imperfect nature of the trapped core (further discussion below with Figure 3.10). The first discharge phase is experienced by all stratifications, regardless of whether a single or double pycnocline is present; the second exists only when the wave contains a trapped core.

Figure 3.9(c) indicates that the second discharge phase exists when the pycnocline separation is within some finite intermediate range. The $\zeta = 0, 0.10$ and 0.20 cases show no drastic change within their discharge rates, whereas those with $\zeta = 0.12$ and 0.15 have

a sudden change around $t = 40 - 50$ s. The ratio of pycnocline separation to width, which we call the separation number $N_s = \zeta L_z/2h$, decides the particular discharge phenomenon that is expressed.

When $N_s \ll 1$, the double pycnocline stratification can be shown to be approximated by a single pycnocline and therefore experiences similar mass transport properties. For $\zeta = 0.10$ in Figure 3.9(c) the separation number is $N_s = 1$ yet the mass transport curve is nearly identical in form to that of a wide single pycnocline (Case 7, $h/L_z = 0.10$; not plotted). Relative difference in $\widetilde{T}_{\text{core}}$ is less than 8% between the two cases for the duration of the simulations. In reality, the stratification of each pycnocline is not tightly constrained within the pycnocline half-width length scale. Rather, it has an effective range close to two or three times the pycnocline half-width. This allows some intermediate stratification between the two pycnoclines that acts to mimic a single, continuous pycnocline.

At intermediate pycnocline separation values, the second discharge phase has a much lower discharge rate than the first phase. One case of particular interest has near lossless transport (T_2 for $\zeta = 0.12, Sc = 20$ in Figure 3.9(c)). Clearly this is a regime where the internal dynamics of the wave are substantially different from small and large separation values.

The final regime occurs when $N_s \gg 1$, where a near immediate discharge of tracer occurs. The pycnoclines are separated to such an extent that no stratification exists between the two. The buoyancy is far too weak to act upon the tracers, causing a rapid emission from the wave. The reduction in transport with increasing pycnocline separation in the first discharge phase is also explained by this reasoning. This agrees well with Sutherland [2002] where wide double pycnoclines experienced very weak transport. Complimentary results exist for surface trapped mode-1 waves in the presence of a mixed layer at the surface [Lamb, 2002].

Efficient mass transport relies upon the stratification to act upon the wave core to force some form of recirculation. If the forcing is too strong, the wave core deteriorates due to instabilities initiated at its edges [Carr et al., 2012]. On the other hand, no core forms when the forcing is too weak. In between is the regime in which the forcing is appropriately balanced to sustain transport. For double pycnoclines the optimal transport occurs when the separation number is moderate. This can be attributed to a non-zero local minima of the buoyancy frequency in the background density field which acts to create a calm environment within which the recirculating core can exist.

To further expound upon this we focus on the generation of the wave in the optimal transport case ($\zeta = 0.12$ and $Sc = 20$). The evolution of the trapped tracer (Figure 3.10) is initially qualitatively similar to Case 1. As before, a pair of vortex dipoles form when the

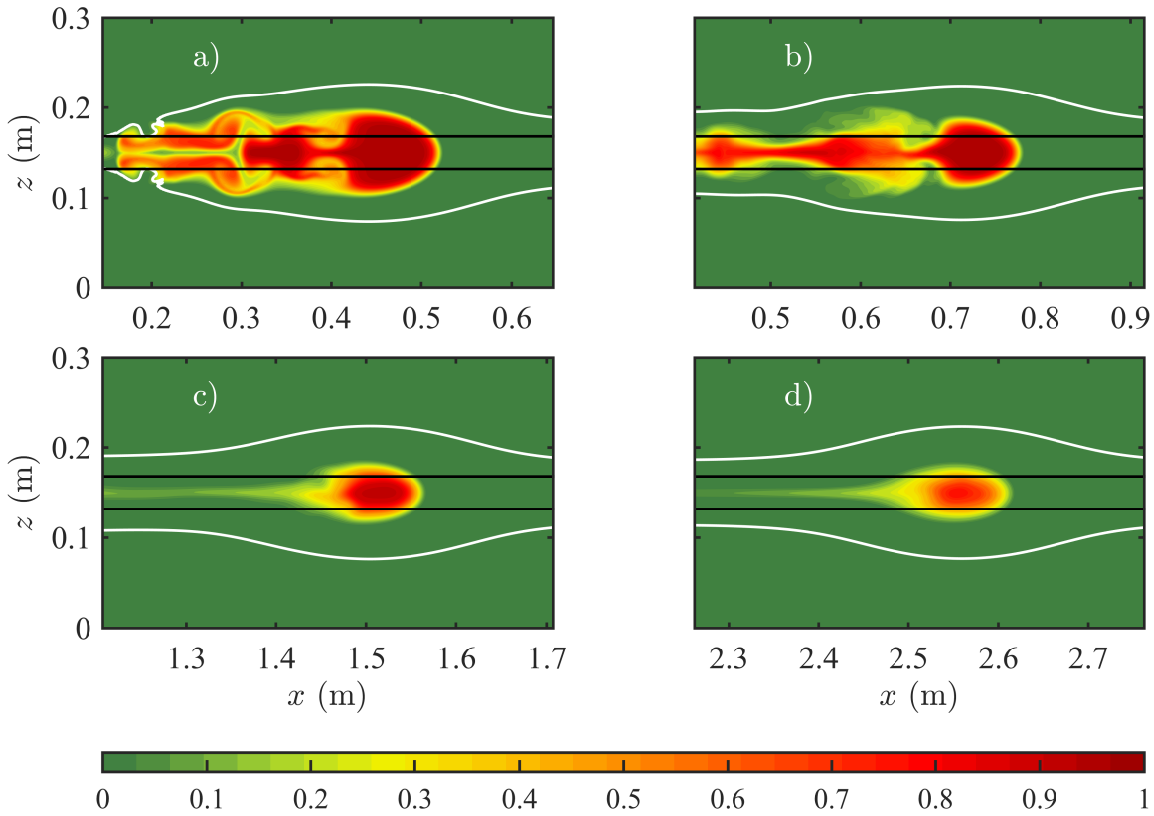

Figure 3.10: Evolution of T_1 for $\zeta = 0.12$ and $Sc = 20$ at $t =$ a) 20 s b) 30 s c) 60 s d) 100 s. Black lines are the centre of each pycnocline and white contour lines are the upper and lower isopycnals.

fluid collapses: the interior vortex pair (at $x \approx 0.4$ m in Figure 3.10(a)), and the exterior vortex pair (at $x \approx 0.3$ m in Figure 3.10(a)). The internal vortex pair, however, is smaller than that formed by a single pycnocline, and decays sooner (Figure 3.10(b)), while the core of the wave remains unaffected by this aft instability. Later (Figure 3.10(d)), the wave still contains a sizeable portion of the original tracer.

The improved transport is a result of the presence of a trapped core (Figure 3.11(c) and (e)). Comparing the streamlines (in a reference frame moving with the wave) to the vorticity demonstrates that the recirculation region exists where the vorticity is approximately zero. Though not plotted in Figure 3.11, the recirculating core consists of the reference density, ρ_0, only. The results largely agree with Luzzatto-Fegiz and Helfrich [2014], who found trapped cores in mode-1 waves to be both homogenous and irrotational. The vorticity plots shown in Figure 3.11 (b), (d) and (f) contains three main regions: 1) the baroclinic vorticity associated with the wave (which is the most dominant), 2) the interior vorticity pair of opposite orientation to the baroclinic vorticity, and 3) the zero vorticity region within the centre of the wave associated with a trapped core.

The persistence of the trapped core depends upon the ability of the interior vorticity pair to intrude into the wave centre. The disruption of the trapped core by the vortex pair requires both sufficient energy and coherence: sufficient energy allows the dipole to move forward within the wave, while coherence maintains the stability of the dipole. The strength of the opposing vorticity depends on the parameters of formation such as the aspect ratio of the intermediate fluid and the background stratification, while the coherence is linked to the Schmidt number. Higher Schmidt numbers are associated with higher momentum diffusion compared to tracer diffusion, therefore small scale structures in the density field will persist longer than the associated kinetic energy leading to a decrease in the coherence of the vortex dipole. The structure of the opposing vorticity is more chaotic and has traveled a shorter distance into the core (compare Figure 3.11(d) and (f)). In all cases, we find that the opposing vorticity eventually enters the wave, resulting in the termination of the recirculating core.

In Case 1, transitory recirculating regions also exist in the wave aft due to the high local turbulence (Figure 3.11(a) and (b)). This chaotic and mixed aft will entrain fluid from the water column [Terez and Knio, 1998], but will not retain this fluid for long (section 3.3)

Double and wide pycnoclines yield behavior that is less chaotic because the local buoyancy forces are smaller, yet cover a greater portion of the water-column, resulting in weaker initial vorticity. The interaction between the vorticity and the trapped core decreases because of the weaker nature of the vorticity and the greater cross-sectional area of the stratification. Interestingly, waves formed from these stratifications are similar in size to

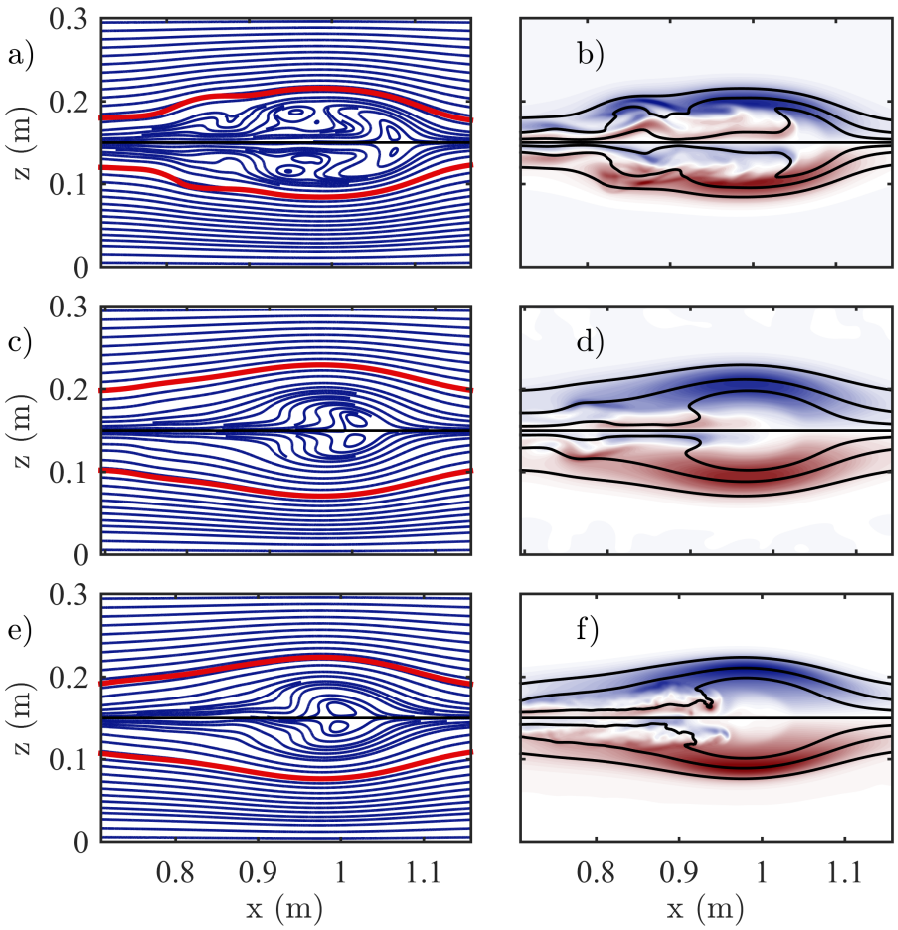

Figure 3.11: Streamlines and vorticity of (a, b) Case 1, (c, d) Case 9 - $\zeta = 0.12$, and (e, f) Case 10 - $\zeta = 0.12$, $Sc = 20$ at $t = 40$ s. Red contours in left column and outermost black contours in right columns are upper and lower isopycnals. Vorticity colour scheme ranges between [-2,2] s^{-1} in b) and [-1.25 s, 1.25] s^{-1} in d) and f).

those created with a single, thin pycnocline. Therefore waves of similar shape are formed with very different internal dynamics, and these dynamics have profound effects on mass transport.

3.6 Summary and discussion

We have conducted a variety of high resolution, three-dimensional numerical simulations of the release of an intermediate fluid into both two and three layer fluids. As the intermediate region collapses into the background stratification, vortex dipoles form in the aft of the gravity current. One vortex dipole remains within the wave core, seeding instabilities which act to reduce the mass transport. All cases show a consistent loss of tracer from the core, with the highest mass transport occurring in a moderately separated double pycnocline with a high Schmidt number.

A 3 cm wide intermediate region created a small mode-2 wave which was unable to transport matter because of the heightened effect of the opposing interior vorticity on the small wave. This vorticity pair resulted in an increased discharge of material along the pycnocline while preserving material slightly off-set from it. Overall, the mass transport was reduced for single pycnoclines because of a lack of a trapped core. The transport was further reduced in the smaller wave because of the heightened instability from the internal vortex pair.

The entrainment of material in vertical columns, T_{1b}, into the wave is ineffective in all cases. The front of each wave is consistently span-wise invariant and dynamically stable (until the instabilities from the aft arrive). Entrainment at the wave aft is also inefficient because of a consistent loss of fluid leaving the wave.

The maximum transport of material occurs within the trapped core, when such a structure exists. The core is distinguishable in its recirculation, which prevents a flux of material across its boundary. In such a case the only means of entrapment is through the molecular diffusion across the trapped core, which is inherently a slow and weak process. The impact on collection of chemical and biological material is therefore expected to be very weak. Transport may be significant, with perhaps the most interesting possibility being transport of swimming organisms [Scotti and Pineda, 2004]. The slow propagation speed of mode-2 waves (compared to their mode-1 counterparts) implies that an organism would not have to swim particularly quickly to ensure that they remain in the core region. Despite this interesting speculation, the greatest impact of mode-2 waves will likely be in the heightened mixing of the pycnocline.

A wide sampling of the parameter space was conducted through the completion of a large ensemble of simulations. The focus has been to understand how varying Schmidt number and pycnocline structure influences the internal dynamics of the wave. Optimal transport occurs when the Schmidt number is large and the stratification minimizes the formation of aft instabilities. Given a trapped core, the mass transport efficiency increases with decreasing tracer diffusivity. However, the efficiency is indistinguishable between tracers of different diffusivity when no trapped core exists.

As these are the first three-dimensional simulations of mass transport by mode-2 waves presented in the literature, we now give a comparison between select two-dimensional (2D) and three-dimensional (3D) simulations (Figure 3.12). The 2D and 3D simulations of the base case (Figure 3.12(a)) are comparable, with the 2D simulation having marginally better transport. The optimal mass transport case (Figure 3.12(b)) shows that the added degree of freedom is necessary to correctly describe the mass transport. The transition to the second discharge phase occurs earlier in three dimensions and therefore results in a higher overall tracer core mass. In 3D, the aft vorticity breaks down and, as a result of the velocity field being free to develop along the span, leaves the trapped core earlier.

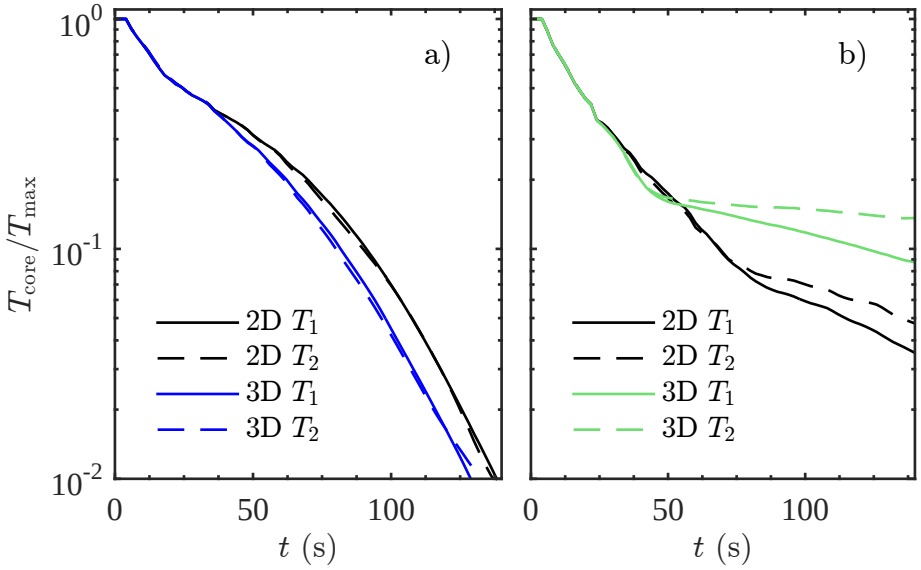

Figure 3.12: Comparison of $T_{\text{core}}/T_{\text{max}}$ for a two-dimensional and a three-dimensional simulation of a) the base simulation, and b) the optimal transport case ($\zeta = 0.12$, $Sc = 20$).

2D comparisons of the other 3D simulations reveal that the difference in mass transport is enhanced at higher Schmidt numbers. This agrees with the link between Schmidt number

and increased three-dimensional behaviour. The differences in transport also grow with the intermediate region width. Other simulations (namely Cases 5, 9, and 11) exhibit mass transport differences within 5% for a majority of the time. Though the general features are similar in the 2D and 3D simulations, and may give comparable transport efficiencies, we stress that knowledge of whether the aft instabilities are correctly described by 2D simulations is not necessarily known *a priori*.

On field scales, horizontal boundaries are an insignificant contributor to the evolution of horizontally propagating waves. Laboratory experiments are not as independent of these boundaries as tanks can be relatively shallow. We have compared no-slip and free-slip vertical boundary conditions and found that the wave is slower by approximately 4% with the no-slip condition. The kinetic energy associated with each wave is also comparable, so the difference between a free-slip and a no-slip condition is minimal. The largest visual impact of the no-slip condition is seen in T_{1b}, since the boundary layer restricts the motion of this field. After the wave has passed through a column, T_{1b} has a 3 cm deep transition region connecting the boundary layer to the main interior region. One additional product of using a no-slip condition is the potential for Rayleigh-Taylor instabilities to form around the intermediate region once the fluid has collapsed.

Further experimental and theoretical studies on the aft instabilities are needed for a better understanding of the efficiency of mass transport in mode-2 waves. Particular focus must be placed on the origins of the opposing core vorticity and whether it is common to all mode-2 waves or simply those formed by the commonly used lock-release technique. Laboratory experimentation on mass transport in double pycnocline stratifications is also needed for comparison with the results reported here.

We have seen that the internal dynamics of mode-2 waves are highly dependent upon external motions. In the coastal oceans, Shroyer et al. [2010] and Ramp et al. [2015] have shown that mode-2 waves are short lived, indicating that the external environment is energetic enough to disturb mode-2 waves. Interactions between large mode-1 and small mode-2 waves also reveal the ease with which mode-2 waves are destroyed [Stastna et al., 2015], which necessitates an understanding of how the wave energy transfers into lower modes and into turbulent kinetic energy. The implications on mixing are clear. Two such cases currently under investigation are: a shoaling mode-2 wave over a Gaussian hill and wave disintegration under high rotation (the latter relevant to an experimental set up as opposed to the ocean). The asymmetry due to topography for a shoaling wave may result in mode-mode interaction and destabilize the mode-2 wave because of the change in layer depths [Olsthoorn et al., 2013].

3.7 Further perspectives

Thus far, the chapter has assumed that the mode-2 ISW exists in a symmetric stratification, one in which the upper and lower layers are of equal depth. However, the pycnocline is *not* located at the mid-depth in the ocean. Changing the pycnocline location will greatly impact the forces applied on either side of the pycnocline.

One such process for forming internal waves is from the gravity intrusion along a near-surface pycnocline. [Bourgault et al., 2016] observed a frontally forced interfacial gravity current which subsequently produced ISWs and Kelvin-Helmholtz billows concomitantly. They also ran numerical simulations, not too dissimilar from the following, to show that the intrusions in initially dynamically-stable conditions can simultaneously lead to strong mixing and large-amplitude ISWs.

Here we compare the effects of a mid-depth centred pycnocline and one raised by 20% of the depth. Previously, Olsthoorn et al. [2013] considered the three-dimensional dynamics of these cases. We will expand on this foundation by focusing on the internal dynamics of the wave generation, and the response of passive tracers to these waves, in particular, the efficiency of Eulerian transport.

Since the mixed region encompasses the entire fluid depth, when the pycnocline is raised (lowered) from the mid-depth there is greater forcing from the bottom (top) during the collapse of the mixed region. This causes the tail of the mode-2 gravity intrusion to be lifted (lowered) creating an asymmetry across the pycnocline which enables the formation of a mode-1 tail behind the mode-2 ISW. By conservation of mass, the lifting (lowering) requires material in front of the forming mode-2 wave to be displaced below (above) the pycnocline. Thus, a long-wave mode-1 wave of depression (elevation) forms and travels ahead of the mode-2 wave due to its larger wave speed. In total, three waves, two of which did not exist in the mid-depth centred pycnocline, are created in this mechanism: the mode-2 ISW, a leading mode-1 wave of depression, and a trailing mode-1 wave packet.

Figure 3.13 shows the formation and evolution of the mode-2 wave when the pycnocline is raised by 20% of the depth from the mid-depth. The leading mode-1 wave of depression is briefly seen in Figure 3.13b as the lowering of the pycnocline half-width contours (white lines). Later, the wave has travelled ahead of the mode-2 ISW and does not have a major influence on the wave. This wave of depression has an amplitude and wavelength of 1.3 cm and 36.1 cm, respectively, (defined similarly as for the mode-2 wave) and an average wave speed of 4.8 cm/s, nearly double the speed of the mode-2 wave. The mode-1 wave reflects off the end wall and then weakly interacts with the mode-2 wave at $t = 116$ s. Due to the small amplitude of this mode-1 wave, the mode-2 wave passed through with only minor

adjustment (further discussion below). See Stastna et al. [2015] for a discussion of strong interactions between waves of different mode numbers and a large amplitude mode-1 wave.

The more significant effect caused by the initial flux throughout the pycnocline centre is the formation of a mode-1 wave-train behind the main mode-2 wave [Akylas and Grimshaw, 1992]. This method of generation (the mixed region covering the full depth) has created a wave-train which, at early times, has an amplitude comparable to the mode-2 wave. Strong mode–mode interaction occurs, promoting a reduction in the mass transport as seen by the majority of T_1 no longer present within the mode-2 portion of the wave in Figure 3.13f. Furthermore, the structure of the mode-2 ISW with the trailing mode-1 wave packet (Figure 3.13e) looks strikingly similar to Figure 4 in Mehta et al. [2002] and Figure 3 in Shroyer et al. [2010].

A crude estimate for the change in wave speed due to the new pycnocline location can be calculated using the "mode-2" wave speed in a 2-layer immiscible fluid,

$$c_{\text{2layer}} = \frac{1}{2}\left(\frac{g\Delta\rho}{\rho_0}\frac{H_1 H_2}{L_z}\right)^{1/2}, \tag{3.4}$$

where H_1 and H_2 are the quiescent layer depths and we assume that the mode-2 wave speed is half the speed of the first mode. The percent difference of the off-set pycnocline to mid-depth centred pycnocline velocity is $1 - \sqrt{0.21}/0.5 \approx 8\%$. The average speed in this pycnocline off-set case is 2.3 cm/s compared to the 2.5 cm/s for the mid-depth centered pycnocline. The percent difference (8%) matches the observed decrease.

A first mode wave-train has consistently been observed in laboratory tank experiments Brandt and Shipley [2014], Carr et al. [2015], Mehta et al. [2002], even in stratifications where such a tail is not expected to exist. It is impossible to fully remove all forms of asymmetry in the laboratory; the most dominant of which is likely the deviation of the pycnocline centre from the mid-depth. Other sources of asymmetry are the mechanism of generation (vorticity is introduced as the gate must be removed swiftly; even so fluid begins to readjust earlier at the bottom than at the top), and in the difference in the top and bottom boundary conditions (the top is often uncovered and therefore free-slip, while the bottom is no-slip).

These inherent asymmetries are not present in the mid-depth pycnocline case because all variability has been removed. However, it is not surprising to see a wave-train of such large amplitude in the pycnocline off-set case because of the magnitude of the asymmetry. The relative scale of the wave-train is comparable to, and likely larger than, field observations [Shroyer et al., 2010] and previous laboratory experiments [Carr et al., 2015].

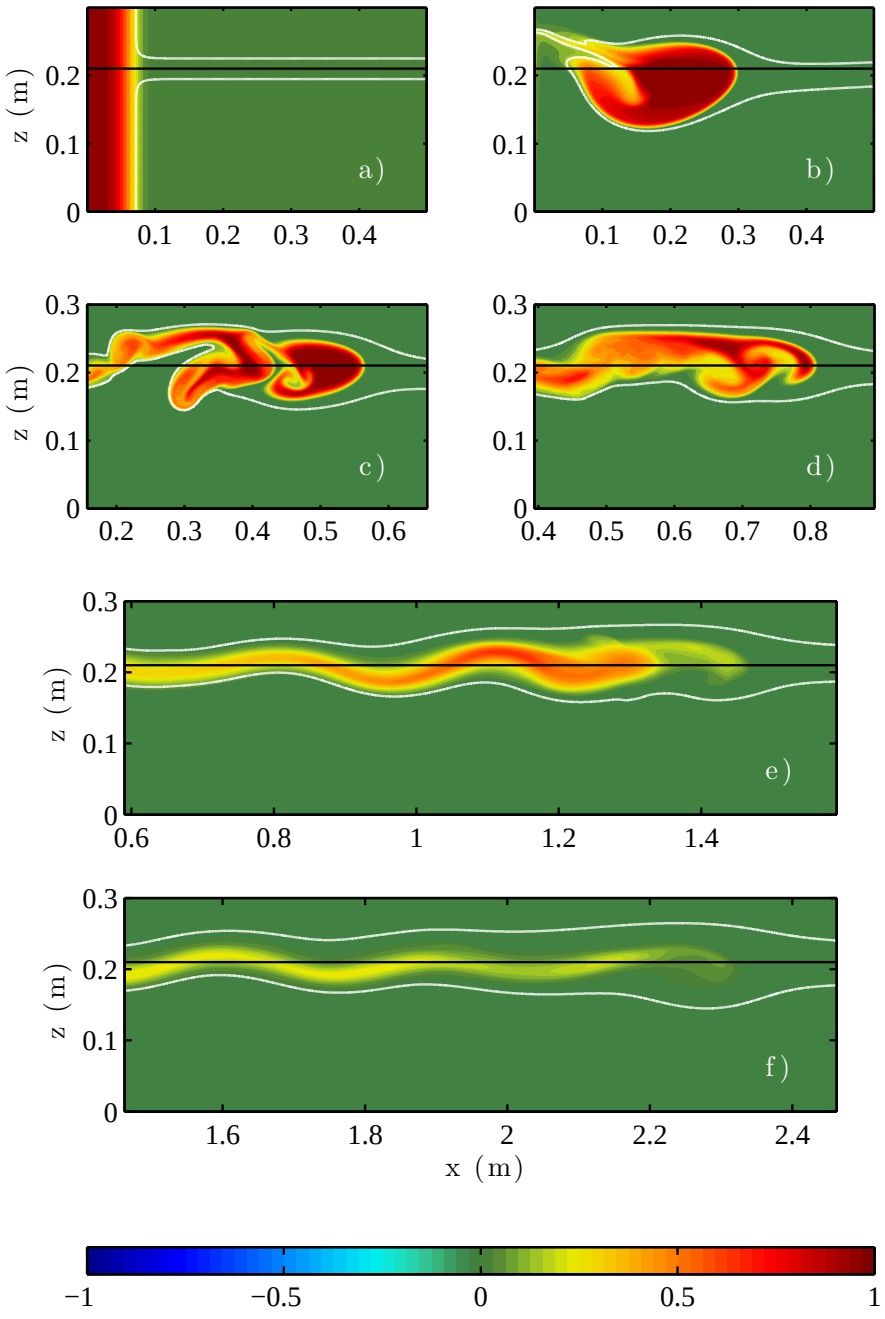

Figure 3.13: Evolution of tracer T_1 for the pycnocline raised 20% of the depth from the mid-depth at $t =$ a) 0 s b) 10 s c) 20 s d) 30 s e) 60 s f) 100 s. Black and white contour lines are equivalent to those in Figure 3.3.

The magnitude of the trailing wave-train and leading mode-1 wave of depression can be minimized by reducing the asymmetry of the intermediate volume. Two dimensional simulations with a systematic reduction of the intermediate volume show that equal intermediate fluid above and below the pycnocline centre creates a stable mode-2 wave (not shown). Nevertheless, a significantly smaller mode-1 wave-train behind the primary wave still forms because of the inherent asymmetry of the stratification.

At $t = 150$ s, the trailing mode-1 wave-train contains at least six full waves. In contrast to Shroyer et al. [2010], this wave-train detaches from the mode-2 wave and the wave-packet continues at a slower speed than the mode-2 wave. Two dimensional simulations on a longer domain (not presented) have confirmed this to be the case.

The wave generation is characterized by more chaotic motion in the off-centre case in agreement with Carr et al. [2015]. Figure 3.13c clearly shows regions of overturning and intrusion of fluid from the bottom layer into the aft of the mode-2 wave. This intrusion later moves to the fore of the trapped fluid as seen in Figure 3.13d. Figure 3.13e and f show how the majority of the tracer has been discharged from the mode-2 core.

The trapping of the downstream tracer by the mode-2 wave (Figure 3.14) exhibits similar features to the mid-depth centered case. The largest difference from Figure 3.4 is the separation of the tracer due to the chaotic motion in the lower portion of the wave core (Figure 3.14d). This motion is due to the intrusion from the lower layer which carried a portion of T_{1b} into the interior of the mode-2 core. Therefore, trapping occurs preferentially in the the lower portion of the wave as opposed to the calmer upper side. However, like in the mid-depth centred pycnocline case the trapping of the tracer is not strong and relies on the tracer to diffuse into the wave core region. Since the tracer diffuses into the wave core, it is not that difficult for the tracer to re-diffuse over the core boundary and be lost, especially if there is no core to partially trap the tracer.

The isosurfaces from the off-set pycnocline describe a qualitatively different pattern of activity from the mid-depth case (Figure 3.15 compared to Figure 3.5). The front of the wave is still smooth with no span-wise variation, but the rest of the gravity intrusion is much more chaotic. Span-wise variation is very evident and the initially trapped tracer is easily released from the core. The top of the wave, however, remains smooth and unchanging during passage across the tank. Carr et al. [2015] also observed the same heightened instability in the lower portion of the wave in conjunction with a stable upper portion.

Figure 3.16 shows the span-wise structure of the variation in the tracers along the cross-section $x = 0.6$ m at $t = 26$ s. The plumes in the mid-depth centred case are a result of overturning caused by the vortex pair moving through the mode-2 wave. In the mid-depth

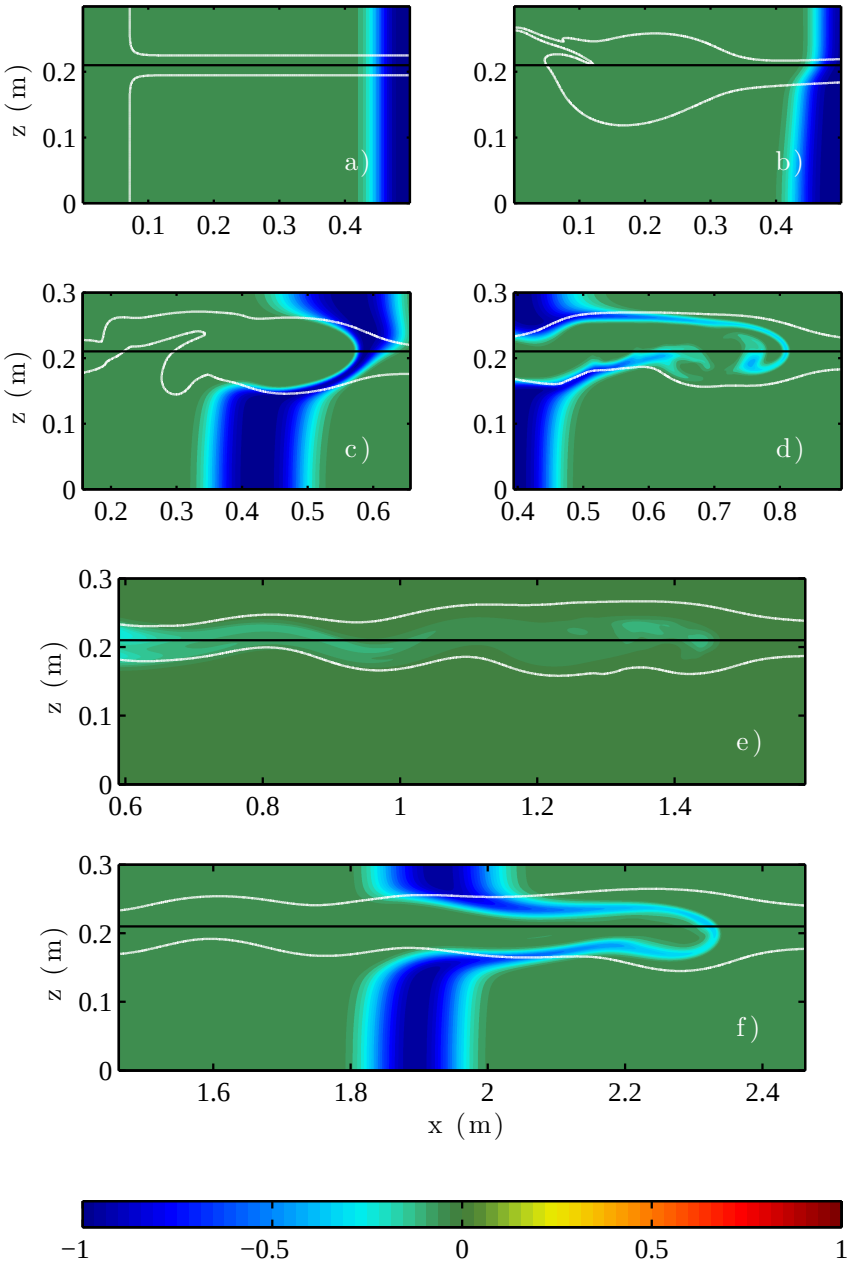

Figure 3.14: Evolution of tracer T_{1b} for the pycnocline raised 20% of the depth from the mid-depth at t = a) 0 s b) 10 s c) 20 s d) 30 s e) 60 s f) 100 s. Bands spanning the entire water-column are centered at $x = 0.5, 2$ m. Black and white contour lines are equivalent to those in Figure 3.3.

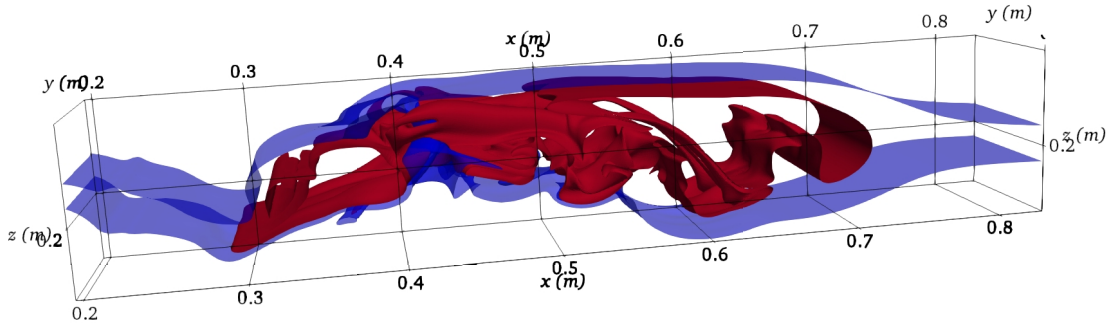

Figure 3.15: Isosurface of density (blue) and T_1 (red) for the case in which the pycnocline is centered away from the mid-depth at $t = 26$ s. Contours at $\rho = \rho_0 \pm \Delta\rho/4$, and $T_1 = 1/2$.

centred case, the clarity of the billows in T_2 are greater than for T_1, but both have the same features because they are formed by the overturning of density. The tracer in the off-set case is not as striking as the mid-depth centred case, but still has overturning at $z \approx 0.21$ due to the intrusion into the lower potion of the wave. The upper portion of the wave in the off-set case is also span-wise invariant, while the lower portion is varied.

Thus far we have seen that the mid-depth separated case has qualitatively been more chaotic than the mid-depth centered case. To quantify this we define a measure of turbulence using the standard deviation of kinetic energy along the span of the channel, $\sigma_{\mathrm{KE},y}(x, z, t)$. To reduce the number of dependent variables by one, we define the scaled, vertically-integrated, span-wise standard deviation as,

$$\sigma_{\mathrm{KE}}(x,t) = \frac{L_y \int_0^{L_z} \sigma_{\mathrm{KE},y} dz}{\max_{x\in[0,L_x]} \left\{ \int_0^{L_y} \int_0^{L_z} \frac{1}{2} \left(u^2 + v^2 + w^2\right) dz dy \right\}}. \tag{3.5}$$

σ_{KE} for the mid-depth centered and off-set pycnocline are plotted as space-time plots in Figure 3.17.

Furthermore, there are two simple choices to remove any dependence on position. A local measure of turbulence is simply the spatial maximum of σ_{KE},

$$\sigma'_{\mathrm{KE}}(t) = \max\left\{\sigma_{\mathrm{KE}}\right\}, \tag{3.6}$$

whereas a global measure is the average standard deviation of kinetic energy scaled by the average kinetic energy,

$$\overline{\sigma}_{\mathrm{KE}}(t) = \frac{L_y \int_0^{L_x} \int_0^{L_z} \sigma_{\mathrm{KE},y} dz dx}{\int \frac{1}{2} \left(u^2 + v^2 + w^2\right) dV}. \tag{3.7}$$

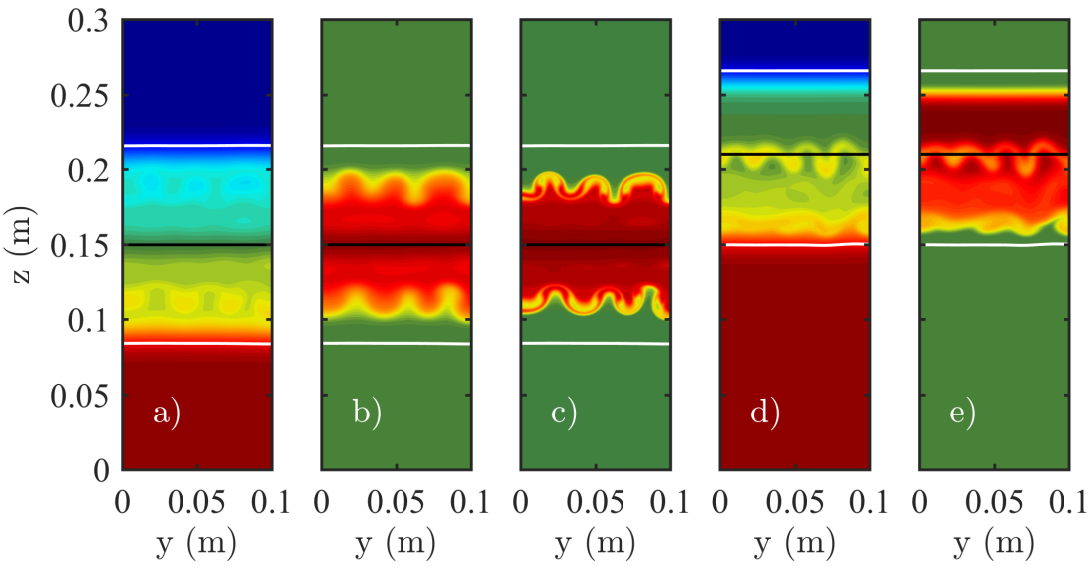

Figure 3.16: Span-wise distribution of density and tracers at $t = 26$ s and $x = 0.6$ m. Mid-depth centred pycnocline: a) density, b) T_1, and c) T_2. Off-set pycnocline: d) density, and e) T_1. White lines show upper and lower isopycnals, and the black line is the pycnocline centre. Compare to figure 3.6.

Both the local and global measures of turbulence are plotted in the insets in Figure 3.17 as red and blue curves, respectively.

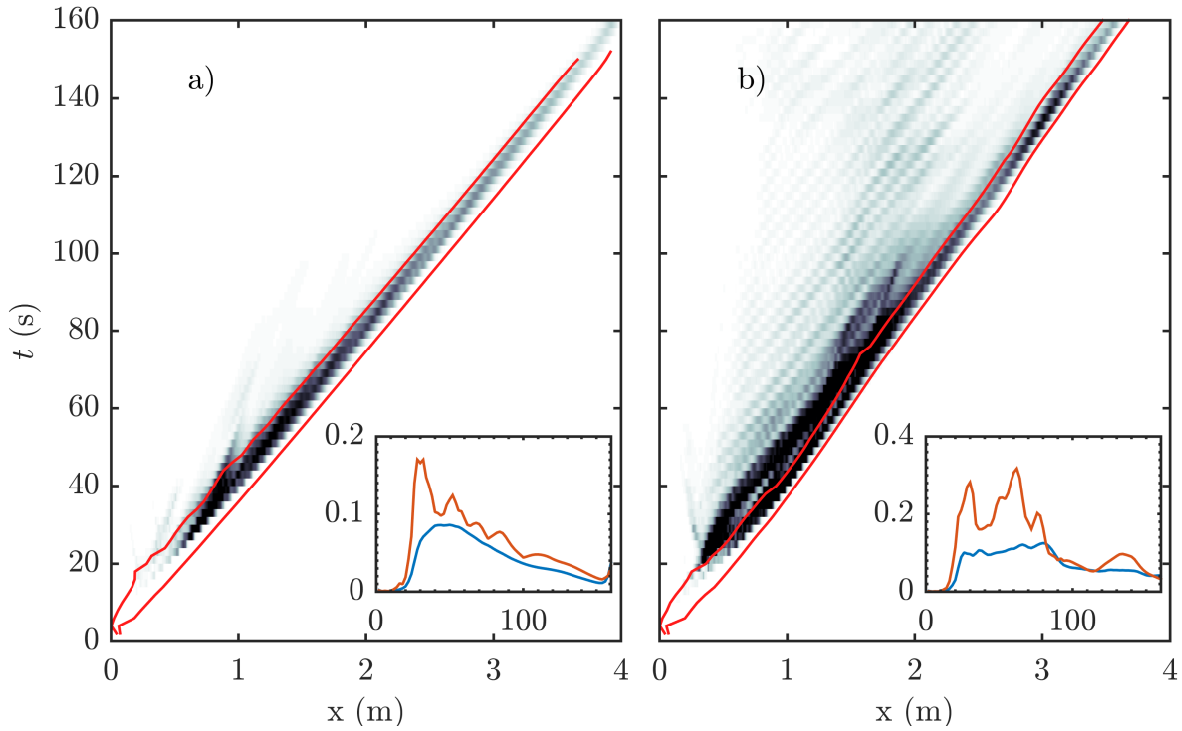

Figure 3.17: Scaled, span-wise standard deviation of kinetic energy space-time plot for the a) mid-depth centered pycnocline b) 20% off-set pycnocline. The colour scheme runs between 0 (white) and 10% (black) of the maximum of σ_{KE}, and the red lines denote the location of the front and back of the mode-2 ISW. Inset gives a global (blue) and local (red) representation of the strength of the variation.

In the depth-centered case the turbulence begins to form around $t = 20$ s and is mainly constrained to the wave body. There is evidence of low-level mixing regions being shed from the mode-2 wave between $t = 50$ and 100 s. The colour scheme is saturated at a maximum of 10% of σ_{KE} emphasizing the small magnitude of the variation of kinetic energy in comparison to the total kinetic energy. The local and global σ_{KE} both experience their maximum values around $t = 40 - 50$ s whereafter the scaled turbulence decays to about 2% before reaching the end of the channel.

The wave in the off-centre pycnocline case experiences far greater turbulence throughout a larger portion of the channel (Figure 3.17b). The turbulence is still primarily constrained

to the location of the mode-2 wave, but there is far more three-dimensionality in the trailing mode-1 wave-train. The local and global σ_{KE} are clearly much larger in magnitude than in the mid-depth centered case, but this heightened turbulence is short lived as seen by the drop in turbulence around $t = 90$ s which is partly explained by the interaction with the long mode-1 that has reflected off the end wall. Clear turbulence within the mode-1 wave-train exists after approximately 100 s. Furthermore, there is evidence here that the trailing wave-train is not phase-locked with the mode-2 ISW and will detach creating two separate wave packets. This is surprising as it will allow the leading mode-2 ISW to survive longer than if the mode-1 wave-train remained attached and constantly extracted energy from the higher mode wave.

Chapter 4

Multi-scale phenomena of rotation-modified mode-2 internal waves

The following chapter, except for section 4.6, has appeared as a publication in *Nonlinear Processes in Geophysics* [Deepwell et al., 2018]. Numerical simulations, analysis, and most of the writing was completed by D. Deepwell. A. Coutino participated in writing the introduction and gave feedback on the analysis. Supervision and direction was given by M. Stastna.

4.1 Introduction

Over recent decades nonlinear internal solitary waves (ISWs) have been the subject of continuing research due, in part, to their common presence in coastal waters [Shroyer et al., 2010, Lamb, 2004] and estuaries [Richards et al., 2013], and an expanding set of applications, such as plankton and krill transport [Scotti and Pineda, 2004] or cross-shelf transport [Hosegood and van Haren, 2004]. Of particular interest are the effects that rotation has on these waves, since they have been observed to have lifetimes such that this effect is non-negligible [Farmer et al., 2009]. At observation sites such as Knight inlet [Klymak and Gregg, 2001] and within the St. Lawrence River [Mertz and Gratton, 1990], side walls may also impact the propagation of these waves. Indeed, classical linear wave theory for rotation-modified waves demonstrates that the presence of side walls allows a different type of wave to be created, namely a Kelvin wave.

The dominant insights on Kelvin waves in a channel geometry come from the experimental work of Maxworthy [1983], and Renouard et al. [1987]. These authors performed lab-scale experiments in which mode-2 [Maxworthy, 1983] and mode-1 [Renouard et al., 1987] Kelvin waves were generated in a rectangular domain. They found that though the wave amplitude increased at the channel wall with increasing rotation rate, the phase speed and shape were comparable to waves of similar amplitude in the presence of no rotation. The authors also described how the wave amplitude decayed exponentially away from the wall, how the wave front was curved backwards, and how the waves decayed as they propagated away from the generation site due to the generation of inertial waves. In Sánchez-Garrido and Vlasenko [2009] the authors discussed numerical simulations constructed to approximately model the evolution of mode-1 waves in the Strait of Gibraltar. When the latitude was increased to 60 degrees, the authors found clear evidence of a secondary tail of Poincaré waves which trailed the leading Kelvin wave and extracted energy from this wave. The authors also found clear evidence of Mach stems. As this study provides a direct comparison work to our own, its results will be discussed at various points in the following.

In the simpler case of a rotating fluid adjusting without the presence of side walls, it has been observed that if dispersive effects are accounted for, a leading solitary wave is created which then breaks down into a nonlinear wave packet as it propagates [Coutino and Stastna, 2017]. Additionally, a geostrophic state is created at the site of the initial condition which oscillates at a near inertial frequency and radiates waves. Previous work based on hydrostatic equations [Kuo and Polvani, 1997] had suggested that the nonlinear waves created would steepen and eventually break, however, when dispersive effects are accounted for, breaking does not occur and a nonlinear wave packet is generated instead. This effect has been observed in laboratory scale experiments using the Coriolis Rotating Platform in Grenoble [Grimshaw et al., 2013]. To account for these effects the authors used model equations based on the rotation modified Korteweg-de Vries (KdV) or Ostrovsky equation, which gave qualitatively similar results to the observations. However, these equations do not account for the full nonlinearity which accounts for the differences to Coutino and Stastna [2017] where the full Euler equations were used.

The work by Fedorov and Melville [1995] showed that if dispersive effects are neglected (when nonlinearity is large) the Kelvin waves will break. Specifically, the authors found that rotation delays the onset of breaking by 60%. When the breaking occurs, it simultaneously forms across the zone of uniform phase that is normal to the boundary. The increase in nonlinearity is seen to create a dipole structure in the cross-shelf velocities. On a similar note, Kuo and Polvani [1997] note that time to breaking depends on both the rotation rate and the steepness of the initial conditions (see their Figure 18 for details).

However, it is unclear how a more realistic model with short wave dispersion would modify these results.

There have been a number of studies on Kelvin waves from a model equation approach. Grimshaw [1985] derived a rotation-modified Korteweg-de Vries (rKdV) equation whose transverse structure is that of a linear Kelvin wave. The author also showed that when rotation is weak, (the internal Rossby radius is much larger than the wavelength of the wave) the evolution is described by the rotation-modified Kadomstev-Petviashvili (rKP) equation. This was followed up by Katsis and Akylas [1987] who performed a numerical simulation of these equations and found that the wave amplitude varied exponentially across the channel and the wave front was curved backwards in agreement with the results seen in Maxworthy [1983] and Renouard et al. [1987].

ISWs within a cylindrical geometry have also been investigated by Ulloa et al. [2014] and Ulloa et al. [2015] using an immersed boundary numerical method. The authors found that the rotation rate affected the nonlinear steepening which further caused a degeneration of the fundamental Kelvin wave into a solitary-type wave packet. When the Kelvin wave amplitude was large enough, localized turbulent patches were produced by Kelvin wave breaking. However, we estimate that a single turbulent patch has a vertical extent of about 40 cm and contains approximately 25 points. Since the features within this turbulent patch are highly chaotic, it is doubtful that the small-scale structure contained within this region were sufficiently resolved.

While results on non-rotating mode-2 ISWs, especially with regards to their mass transport capabilities [Deepwell and Stastna, 2016, Salloum et al., 2012, Brandt and Shipley, 2014, Terez and Knio, 1998], are readily available, however the case of mode-2 ISWs in a rotating reference frame has only been investigated experimentally by Maxworthy [1983]. We extend that research with a focus on the breaking of the rotation modified ISW (or Kelvin wave, depending on one's choice of terminology) at the focusing boundary.

The remainder of the chapter is structured as follows: the set up of the numerical experiments and numerical methods are outlined first, with the results that follow structured to identify fundamental differences between rotating and non-rotating evolution, characterize the three-dimensional structure of near wall overturning, and point out the importance of keeping a realistic Schmidt number other than Sc=1, which has been consistently used in past literature.

4.1.1 Configuration of Numerical Experiments

We have run a series of direct numerical simulations in a setup similar to that of Maxworthy [1983]. These experiments employed a gravity intrusion in a rectangular domain in a rotating reference frame to generate mode-2 waves. On experimental scales, both the gravity intrusion and the subsequent set of rank-ordered mode-2 internal solitary-like waves are modified by rotation.

We form the gravity intrusion by releasing a large perturbation into a quiescent, quasi-two-layer background stratification (Figure 4.1). Algebraically, the density field has the form,

$$\rho(x,z) = \rho_0 - \frac{\Delta\rho}{4}\left[\tanh\left(\frac{z - z_0 - \eta(x)}{h}\right) + \tanh\left(\frac{z - z_0 + \eta(x)}{h}\right)\right], \tag{4.1}$$

where

$$\eta(x) = \frac{H_m}{2}\exp\left[-\left(\frac{x}{L_m}\right)^p\right], \tag{4.2}$$

describes the perturbation in which H_m, L_m, and p set the height, width, and transition length, respectively. This stratification leads to a single hyperbolic tangent profile for $x \gg L_m$ and a double hyperbolic tangent profile with an intermediate density layer for $x \ll L_m$. The pycnocline is centred on the mid-depth, while the rest of the stratification parameters are listed in table 4.1. For comparison, the domain size is 6.4 m $\times$ 0.4 m $\times$ 0.3 m.

Table 4.1: Stratification parameters.

H_m (m)	L_m (m)	p	$\Delta\rho/\rho_0$	z_0	h
0.1	0.3	8	0.02	0.15	0.02

We have completed a suite of numerical simulations at various rotation rates and Schmidt numbers. The rotation rate has been specified using the Coriolis parameter, f, which is defined in the usual way as twice the rotation rate. We define our maximum Coriolis parameter as $f_0 = 0.105$ s^{-1} which is comparable to the literature [Grimshaw et al., 2013] and in particular to values achievable in the Coriolis Rotating Platform.

We characterize the parameters of the leading wave in regard to their size at the $y = 0$ m wall. In particular, the wave speed, c_w, and amplitude, a_w, will be parametrized at this boundary because it is where they reach their maximal values due to the focusing of mass and energy by rotation. The amplitude is defined as the maximum upstream displacement

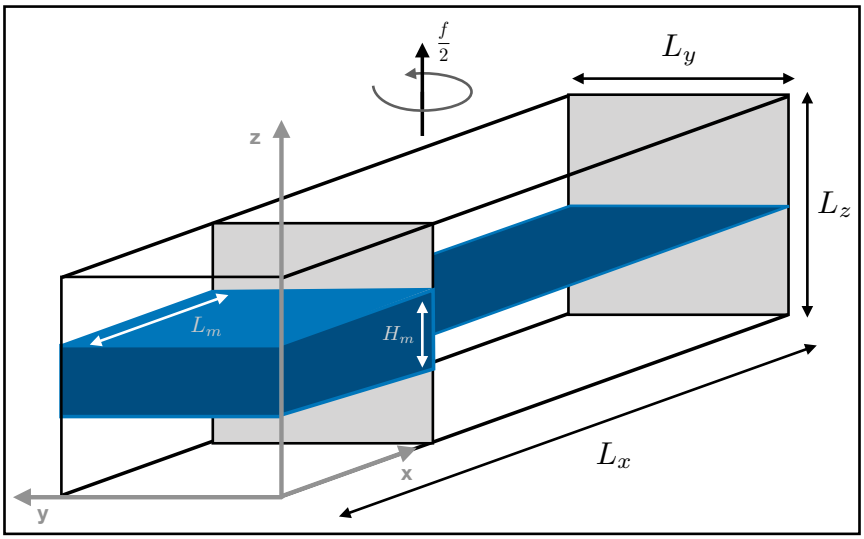

Figure 4.1: Schematic of the numerical domain. The blue region corresponds to $\rho = \rho_0$ with heavier fluid below and lighter fluid above.

of the $\rho(z_0 \pm h)$ isopyncals just prior to the formation of instabilities. The internal Rossby radius of deformation is thus defined as $L_c = c_w/f$, the Rossby number as $\mathrm{Ro} = c_w/fL_m$, the Reynolds number as $\mathrm{Re} = c_w L_m/\nu$, and the Schmidt number as $\mathrm{Sc} = \nu/\kappa$. The kinematic viscosity was $\nu = 2 \times 10^{-6}$ m^2/s for all cases, whereas the mass diffusivity, κ, varied. The parameters and characteristic values for each simulation are presented in table 4.2. The velocity is scaled by the linear, non-rotating, long wave speed, $c_0 = \frac{1}{2}\left(gh\Delta\rho/\rho_0\right)^{1/2}$ [Benjamin, 1967]. The average rate of change of the amplitude is given by $a' = -\frac{T}{h}\frac{da_w}{dt}$, where $T = L_m/c_0$ is the characteristic time scale.

We briefly contrast our set-up to that of Sánchez-Garrido and Vlasenko [2009]. The primary difference is the scale to be modelled. While we seek to model laboratory scale motions, and hence resolve both tank scale and small scale motions, in Sánchez-Garrido and Vlasenko [2009] the authors sought to model field scale motions. Hence their ratio of depth to span-wise extent is much smaller than ours. Moreover they modeled dissipation through an eddy viscosity, while we attempt to carry out a Direct Numerical Simulation (DNS). Nevertheless, the ratio of their Rossby radius to span-wise extent is roughly 0.6, which is similar to some of our experiments. Thus many of the large scale motions in the two sets of simulations can be expected to be similar. In particular, Figure 2 of Sánchez-Garrido and Vlasenko [2009] makes for a useful comparison to some of our findings.

Table 4.2: Case parameters and characterizations.

Case	Sc	f/f_0	c_w/c_0	a_w/h	a'	Re	Ro	L_c (m)
10_0	10	0	1.48	1.47	1.83	6960	∞	∞
10_1/16	10	1/16	1.49	1.45	2.47	7010	23.74	7.12
10_1/4	10	1/4	1.48	1.49	6.02	6960	5.90	1.77
10_1/2	10	1/2	1.46	1.53	6.40	6870	2.91	0.87
10_1	10	1	1.47	1.61	6.76	6900	1.46	0.44
4_0	4	0	1.48	1.46	2.03	6930	∞	∞
4_1/2	4	1/2	1.45	1.53	5.96	6820	2.89	0.87
4_1	4	1	1.46	1.61	6.62	6870	1.45	0.44
1_0	1	0	1.44	1.41	2.88	6770	∞	∞
1_1/2	1	1/2	1.41	1.50	4.97	6640	2.81	0.84
1_1	1	1	1.44	1.61	6.32	6780	1.43	0.43

4.1.2 Numerical Methods

The governing equations used within our numerical model are the stratified Navier-Stokes equations with the f-plane and Boussinesq approximations [Kundu et al., 2012],

$$\frac{D\vec{u}}{Dt} + (-fv, fu, 0) = -\frac{1}{\rho_0}\nabla p + \frac{\rho}{\rho_0}\vec{g} + \nu\nabla^2\vec{u}, \tag{4.3a}$$

$$\nabla \cdot \vec{u} = 0, \tag{4.3b}$$

$$\frac{D\rho}{Dt} = \kappa\nabla^2\rho, \tag{4.3c}$$

where each variable has their usual meaning. The Navier-Stokes equations are presented in dimensional form, while the remainder of this chapter will use the following non-dimensionalizations,

$$\widetilde{x} = x/L_m, \quad \widetilde{y} = y/L_y, \quad \widetilde{z} = z/L_z, \tag{4.4a}$$

$$\widetilde{t} = t/T, \tag{4.4b}$$

$$\widetilde{\rho} = (\rho - \rho_0)/\rho_0, \tag{4.4c}$$

where the later is called the density anomaly. Scaling time by the rotation rate is inapplicable because the flow is predominantly a Kelvin wave. Rather, time has been scaled by

$T = L_m/c_0$ since the propagation speed of a Kelvin wave is equivalent to the gravity wave speed in the absence of rotation.

The size of the channel and the grid resolution are listed in Table 4.3. The stated resolution was sufficient for all but two simulations: case 10_1 and case 4_1. These both had the resolutions in the x and z dimensions doubled to have the total number of points be $4096 \times 256 \times 512$. Grid convergence studies were conducted for these cases because they were the most energetic with the largest and most energetic density overturns. Good agreement was found for the cases with the stated resolution and those with half the resolution. In general, the higher resolutions have been used in this chapter because of their higher accuracy, though bulk characteristics of the flow computed at the lower resolution remain accurate.

Table 4.3: Tank dimensions and numerical resolution.

L_x (m)	L_y (m)	L_z (m)	N_x	N_y	N_z	Δx (mm)	Δy (mm)	Δz (mm)
6.4	0.4	0.3	2048	256	256	3.1	1.6	1.2

4.2 Results: Influence of rotation

We begin by looking at how the ISW is affected by rotation through the Coriolis force. We have chosen the rotation to match that of the Northern Hemisphere which causes objects to be deflected towards the right of their trajectory. In the context of our experiment this leads to span-wise variation in the developing ISW. Maxworthy [1983] found that the wave front became curved as a result of variation of the celerity on wave amplitude. At $\widetilde{y} = 0$ (which we will call the focusing wall) the amplitude and celerity were both larger than at other y values.

We investigate the location of the ISW crests using the scaled, vertically integrated kinetic energy,

$$\xi(x, y, t) = \frac{\int_0^{L_z} \text{KE}\ dz}{\max_{x,y,t} \int_0^{L_z} \text{KE}\ dz} \tag{4.5}$$

where the kinetic energy is defined in the usual way, $\text{KE} = \frac{1}{2}\rho_0 \left(u^2 + v^2 + w^2\right)$, and the maximum is over space and time.

The time evolution of ξ displays the bending of the leading internal Kelvin wave and the developing Poincaré waves for case 10_1 (figure 4.2). Early on (figure 4.2a), the energy

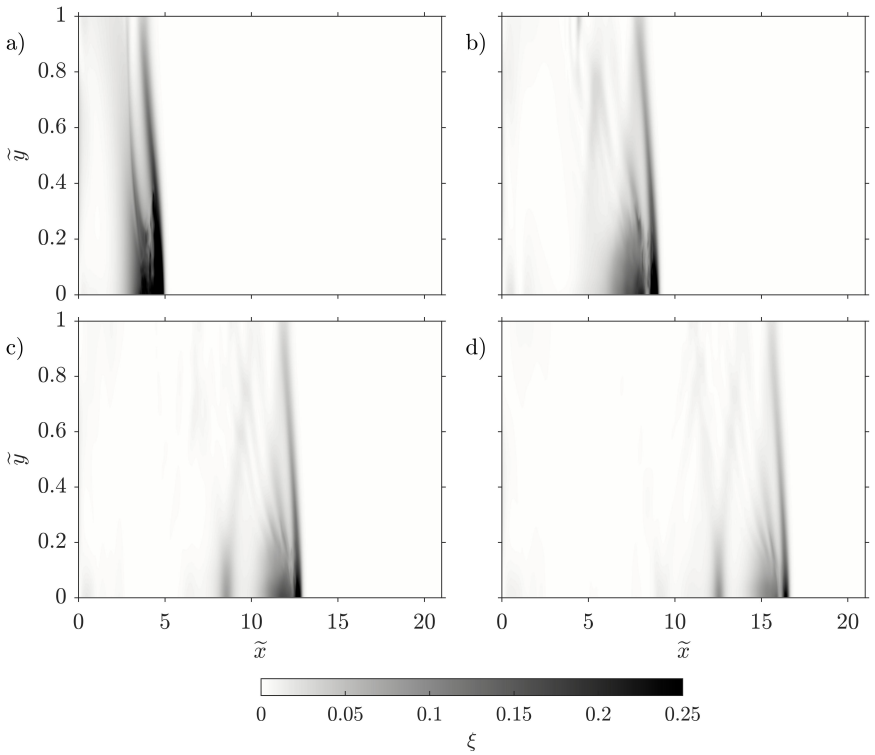

Figure 4.2: The time evolution of the scaled, vertically integrated kinetic energy, ξ, for case 10_1 at t = a) $\widetilde{t} = 2.6$ ($t = 25$ s) b) $\widetilde{t} = 5.2$ ($t = 50$ s) c) $\widetilde{t} = 7.8$ ($t = 75$ s) d) $\widetilde{t} = 10.4$ ($t = 100$ s). Colour axis is saturated at early times to show the wave at later intervals.

is mostly within the leading wave since insufficient time has passed for radiation to occur. However, at this early time, the wave, which began as a plane wave across the channel, has clearly been affected by the rotation as evidenced by energy being focused towards $\widetilde{y} = 0$. This focusing also resulted in the curvature of the leading Kelvin wave front, a phenomenon which remains evident for the remainder of the simulation.

As time progresses, Poincaré waves form behind the Kelvin wave, as previously described by Sánchez-Garrido and Vlasenko [2009]. The Poincaré waves reflect multiple times off both the $\widetilde{y} = 1$ and $\widetilde{y} = 0$ walls. At $\widetilde{t} = 10.4$ ($t = 100$ s) the ratio of total KE on the $\widetilde{y} = 1$ wall to the $\widetilde{y} = 0$ is approximately 0.11 indicating that location of primary activity will be near the focusing wall. The shear also reaches its maximum in this location, enabling the onset of dynamic instabilities.

The presence of the Kelvin and Poincaré waves in this context is quite common and is dependent on the rotation rate (figure 4.3). An increasing rotation rate leads to an increase in the angle that the leading wave makes with the normal of the boundary. The Poincaré waves behave similarly as the rotation rate is varied, however they also have the added complication of reflection and non-linear interaction between waves. When rotation is absent (figure 4.3a), Poincaré waves are unable to form; instead, a simple train of three planar ISWs of decreasing amplitude and energy are formed. Overall, the energy within the Poincaré waves is considerably smaller than the energy in the leading wave, at least over the duration of our numerical experiments.

It needs to be mentioned that the presence of side walls removes the possibility of a span-wise invariant geostrophic state forming in the collapse region since the presence of walls enforces that flow is in the along tank direction. This means that the release of mass and energy into the ISWs is greater than when no side wall is present. The detailed dynamics of the near field are interesting, but beyond the present manuscript.

A secondary boundary trapped wave also forms in the rotation modified cases (figure 4.3b-d). The generation mechanism for this wave is fundamentally distinct from the formation of trailing ISWs in the non-rotating case. In discussing this difference, ISW will be used to describe the non-rotating waves only, while Kelvin and Poincaré waves will naturally be understood to relate to the rotation modified waves. To see how this secondary Kelvin wave is formed, figure 4.4 compares the span-wise average ξ of the non-rotating case (case 10_0, in red) to that of the full ξ for case 10_1 (black pseudocolour). At the early time, $\widetilde{t} = 4.7$ ($t = 45$ s), there is a single leading Kelvin wave and a few radiating Poincaré waves which are just beginning to reflect off the $\widetilde{y} = 1$ wall. The trailing ISWs of the non-rotating case are completely unrelated to the energy distribution of the rotating case. This is clearly evident in figure 4.4 b) and c) where the second trailing ISW is located

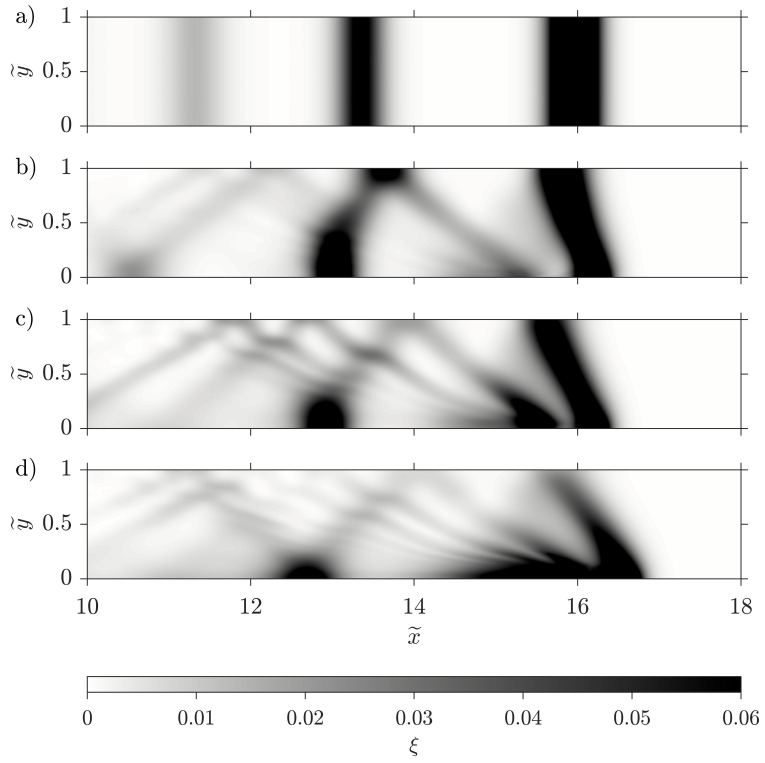

Figure 4.3: Scaled, vertically integrated kinetic energy, ξ, at $\widetilde{t} = 10.4$ ($t = 100$ s) for case with $f/f_0 =$ a) 0 b) 1/4 c) 1/2 d) 1. The scaling is by the maximum over the $f = f_0$ case and the colour axis is saturated to emphasize the Poincaré waves emanating from the focusing region and their reflection off the $\widetilde{y} = 1$ wall. Though in non-dimensional form, the axes have correct dimensional scaling.

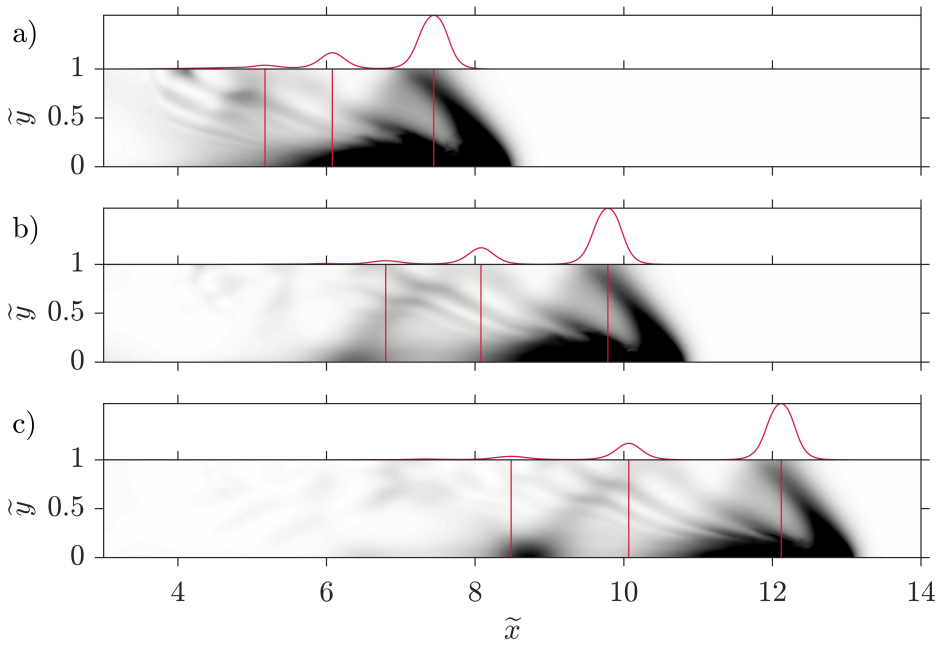

Figure 4.4: Scaled, vertically integrated kinetic energy, ξ, for case 10_1 at t = a) $\widetilde{t}$ = 4.7 (t = 45 s) b) $\widetilde{t}$ = 6.3 (t = 60 s) c) $\widetilde{t}$ = 7.8 (t = 75 s). Scaling and colour axis is identical to figure 4.2. The red plots are the span-wise average ξ profiles for the non-rotating case (Case 10_0), with corresponding maxima locations (vertical lines).

where very little energy exists in the rotating case. The third ISW is near where the second Kelvin wave is forming, but this happens to be a coincidence of the choice of the presented time. Later, at $\widetilde{t}$ = 10.4 (t = 100 s) (figure 4.3) the third ISW is well behind the second Kelvin wave.

More importantly, at high rotation rates the second Kelvin wave is clearly formed by a resonance with the Poincaré waves at the focused wall, which is directly contrary to how the trailing ISWs form without rotation (they are the excess mass that isn't trapped by the leading wave). This description appears to be valid for rotation rates greater than $f/f_0 = 1/4$, since rates slower than this show that the trailing Kelvin wave matches the generation of a trailing ISW in the non-rotating case with additional perturbations due to Poincaré waves.

As described by Sánchez-Garrido and Vlasenko [2009] the Poincaré waves will continue to remove energy from the leading Kelvin wave, which is then deposited in this secondary Kelvin wave. This deposition primarily occurs on the focusing wall, as opposed to equal

deposition on both sides of the channel, because of the broken symmetry caused by the collapse of intermediate fluid on one end of the channel. This means that there is more residual kinetic energy at $\widetilde{y} = 0$ (compared to $\widetilde{y} = 1$), and that the time for the Poincaré wave to resonantly interact with the Kelvin wave is greater at $\widetilde{y} = 0$ since both are traveling in the same direction. Once the secondary Kelvin wave is fully developed, this resonance can be considered analogous to a Mach stem in that the energy builds up on the boundary enough that the reflection no longer occurs at the boundary, and moves instead some distance away from the wall.

As energy is drained from the leading Kelvin wave and deposited into the secondary wave, the secondary wave will eventually become more energetic than the first resulting in an eventual overtaking. Our simulations do not show this feature since our channel is not long enough and we are focused on the shorter time scales associated with the energetics of the leading Kelvin wave. See Sánchez-Garrido and Vlasenko [2009] for a description of overtaking.

The differentiation of whether a wave is a Kelvin wave or a Poincaré wave is made difficult because of the non-linearity associated with the large amplitude of these waves. The classical linear theory presented by Kelvin describes a Kelvin wave as one which has no span-wise velocity, and where the wave crest does not curve in the span-wise direction. A simple check shows that the leading and radiating waves have significant span-wise velocities which would indicate that they are not Kelvin waves (in the classical sense). However, we choose to label the radiating waves as Poincaré waves and the leading wave as a Kelvin wave because both fit all other descriptions of the particular wave type.

We just saw that the radiating Poincaré waves resonate to form a secondary Kelvin wave. Since this secondary wave is separated from the chaotic leading wave, it could possibly fit better in the description of a classical Kelvin wave. Figure 4.5 presents a test for this by plotting the vertically integrated span-wise squared velocity (in dark) and contours of the total vertically integrated KE (in red). The secondary wave (at $\widetilde{x} \approx 12.5$) does indeed show no span-wise velocity or wave crest curvature, and thus our description of it as a Kelvin wave is valid. The red lines indicate the presence of a wave, while black shading denotes the strength of the span-wise velocity. The classical Kelvin wave is evidenced where there is a wave (red contours) with no span-wise velocity (black shading). We also notice that the region directly trailing the wave also has little to no span-wise velocity. Looking back at figure 4.3b and c it becomes clear that there are Kelvin waves directly trailing the leading wave at weaker rotation rates (the highest rotation rate requires more time to settle into this description). This Kelvin wave is distinct from the previously described secondary wave. In this case they are formed out of the remains of the excess focused mass along $\widetilde{y} = 0$. To distinguish this Kelvin wave from the leading wave, we call

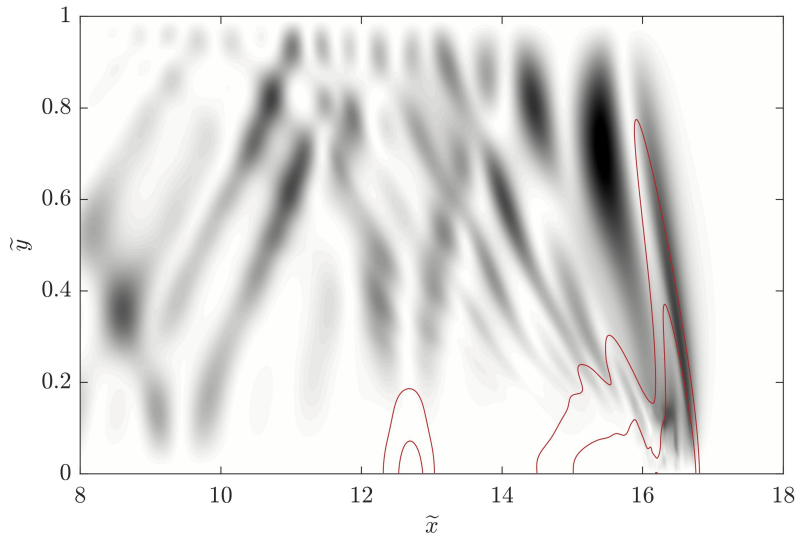

Figure 4.5: Vertically integrated v^2 at $\widetilde{t} = 10.4$ ($t = 100$ s) for case 10_1. Red contours are level curves of the vertically integrated KE.

it the Kelvin wave tail.

The dynamics seen thus far are fundamentally different than in the case without the side walls. As described in Coutino and Stastna [2017], without the walls the Poincaré waves steepen and eventually breakdown into a non-linear wave packet as dispersive effects take over. The addition of side walls appears to slow the large-scale breakdown of the leading wave. Rather, this energy is moved towards the side wall, and is then radiated leeward into trailing Poincaré waves at a slower pace.

The advection of kinetic energy within the Kelvin and Poincaré waves is key to understanding how the distribution of this energy is influenced by the side wall. The span-wise flux of KE (figure 4.6) reveals some interesting features. Of primary interest is the leading Kelvin wave which has both positive and negative span-wise flux of KE. Close to the wall (figure 4.6c), the front of the wave has advection away from the wall, which then becomes a stronger, more localized, return of kinetic energy flux towards the wall within the downstream portion of the leading wave. Further from the side-wall (figure 4.6a), the KE flux is weaker by nearly an order of magnitude and the structure has changed so that the leading wave contains more positive flux.

The secondary Kelvin wave (near $\widetilde{x} = 12.75$ m) has much weaker KE flux even though the waves are of comparable amplitude. The leading wave still contains residual energy

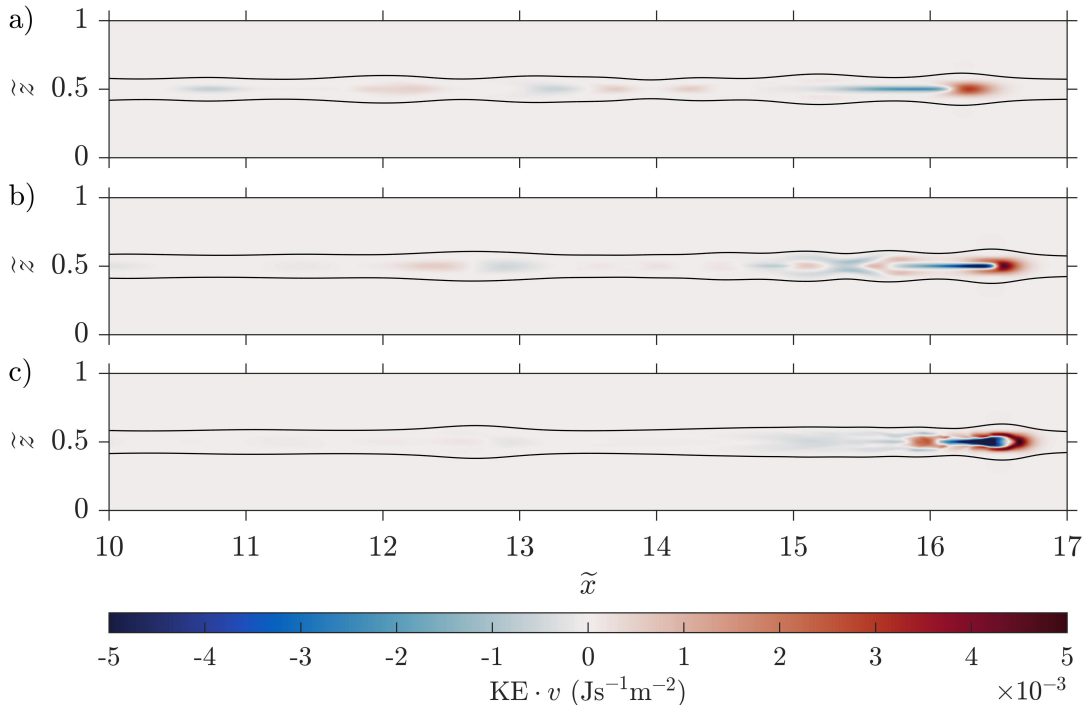

Figure 4.6: Span-wise kinetic energy flux density for case 10_1 at $\widetilde{t} = 10.4$ ($t = 100$ s) and $\widetilde{y} =$ a) 1/2 b) 1/4 c) 1/8.

from the K-H instabilities while the secondary wave receives energy from upstream. To within 3%, the same KE flux is advected towards and away from the focusing wall in this secondary Kelvin wave.

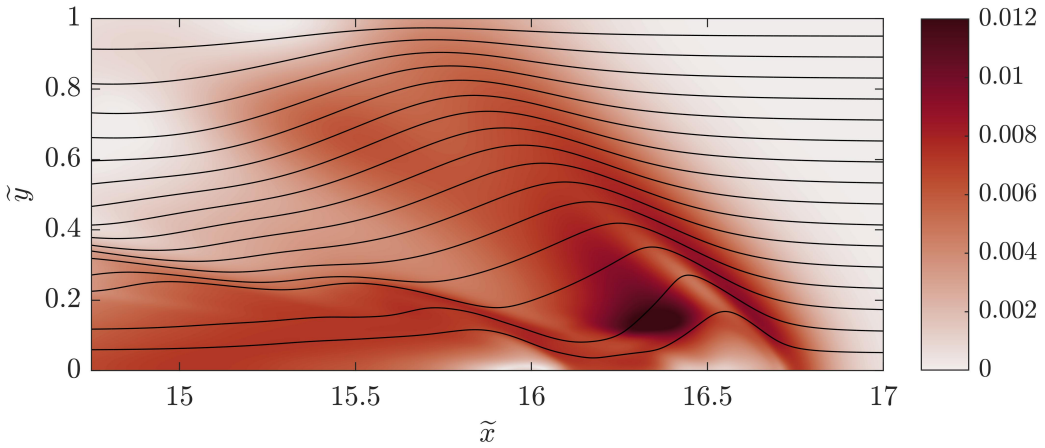

Figure 4.7: Horizontal kinetic energy flux density for case 10_1 at $\widetilde{t} = 10.4$ ($t = 100$ s) and $\widetilde{z} = 0.5$. Streamlines show direction of KE flux in reference frame moving with the leading wave (i.e. flow is right to left). Colour axis shows magnitude of KE flux.

For comparison purposes, we have completed the same simulation in two dimensions while allowing transverse flow to be coupled to horizontal motion through the Coriolis force (i.e. a two-and-a-half dimensional model). Since there exists no side wall, the radiated ISWs are smaller because much of the energy remains within the geostrophic state. Regardless of the waves being smaller and thus traveling slower, the KE flux in the leading wave of the 2D case (not shown) is different from that of the 3D case with sidewalls, especially near the wall. Further from the side walls, the two become more similar yet remain distinct in the magnitudes and distributions of the KE flux.

The span-wise variation in the KE flux along the mid-depth ($\widetilde{z} = 0.5$ m) further describes the KE flux away and towards the focusing wall. Figure 4.7 displays both the magnitude of the flux (colour) and direction (streamlines) in a reference frame moving with the wave. The strongest KE flux is directed towards the wall in the aft of the Kelvin wave. We hypothesize that this KE flux is the cause of wave breaking in the Kelvin wave (the details of which we present in the next section). The kinetic energy near the wall then leaves the Kelvin wave and travels along the wall until forming the Kelvin wave tail some time later.

4.3 Results: Details of wave breaking

Now that the description of the global wave field has been presented, we move onto the localized behaviour of the leading Kelvin wave at the focusing wall. As described by Maxworthy [1983], the dominant instability takes the form of a pair of Kelvin-Helmholtz (K-H) billows at the crests of the leading Kelvin wave at the upper and lower extrema of the wave (figure 4.8a), and confined to within approximately ten centimetres (a quarter of the channel width) of the focusing wall (figure 4.8b-d).

For all cases, the Kelvin-Helmholtz billows simultaneously form as pairs with a vortex above and below the pycnocline. Furthermore, except during the early energetic K-H formation, these billows remain synchronous even during the process of being broken down. For a while it appeared as though case 10_1 made a transition from simultaneous K-H formation to an oscillatory one. However, this transition disappeared when the resolution was increased to properly resolve this case. Whether the vortices form simultaneously or not, they are visually analogous to a von Karman vortex street. We note that there is no quantitative correspondence since the object is not a solid, there are no boundary layers, and the rotation rate is an additional parameter which affects the form of the vortex street.

At the wave crest, the wave has the expected exponential decay (figure 4.8d). Further behind, a description that is purely in the $\widetilde{x} - \widetilde{z}$ plane is no longer valid, since the wave front curves backwards as discussed in the previous section. However, the instabilities remain trapped along the side wall (figure 4.8b and c), while the wave itself, which created the instabilities, remains stable further away. In the density field, the instabilities are recognized as interleaving layers of lighter and denser fluid associated with the roll-up of the K-H billows. The span-wise extent remains largely unchanged as the vortices leave the leading wave. This means that rotation causes mixing and turbulence to occur at a preferred location, namely on the focusing wall. Should the geometry, or environmental forcing (e.g. flow over a sill in a fjord) cause Kelvin waves to be generated at a specific location, this would indicate that one side of the channel would experience more mixing. The aforementioned fjords, as well as narrow lakes would be particularly susceptible to this.

We find that changes in the rotation rate (i.e. the strength of the Coriolis force) influence the intensity of the K-H billows (figure 4.9). Though the initial available energy is the same in all cases, the higher rotation rates lead to higher localized kinetic energy density. At early times (first column of figure 4.9) the amplitude of the leading waves are all comparable, but have varying levels of stability. The cases with increasing rotation are far more energetic. Fundamentally, these vortices are formed from stratified shear instabilities

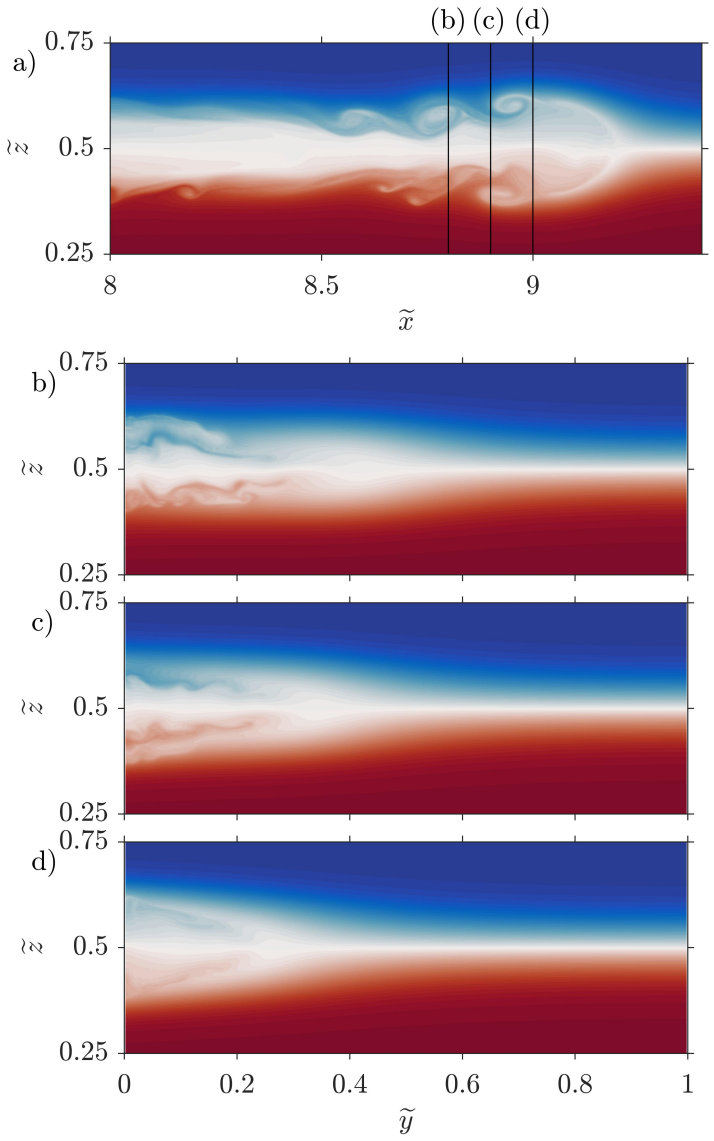

Figure 4.8: Density anomaly, $\widetilde{\rho}$, at $\widetilde{t} = 5.2$ ($t = 50$ s) and a) $\widetilde{y} = 0$ b) $\widetilde{x} = 8.8$ c) $\widetilde{x} = 8.9$ d) $\widetilde{x} = 9$ for case 10_1.

commonly associated with larger amplitude waves [Brandt and Shipley, 2014]. This leads us to suggest that a coastally trapped wave has a lower minimum amplitude threshold for instability generation. Over time this causes the wave to reduce in amplitude considerably faster than would be the case without the presence of rotation. The precise reason for the

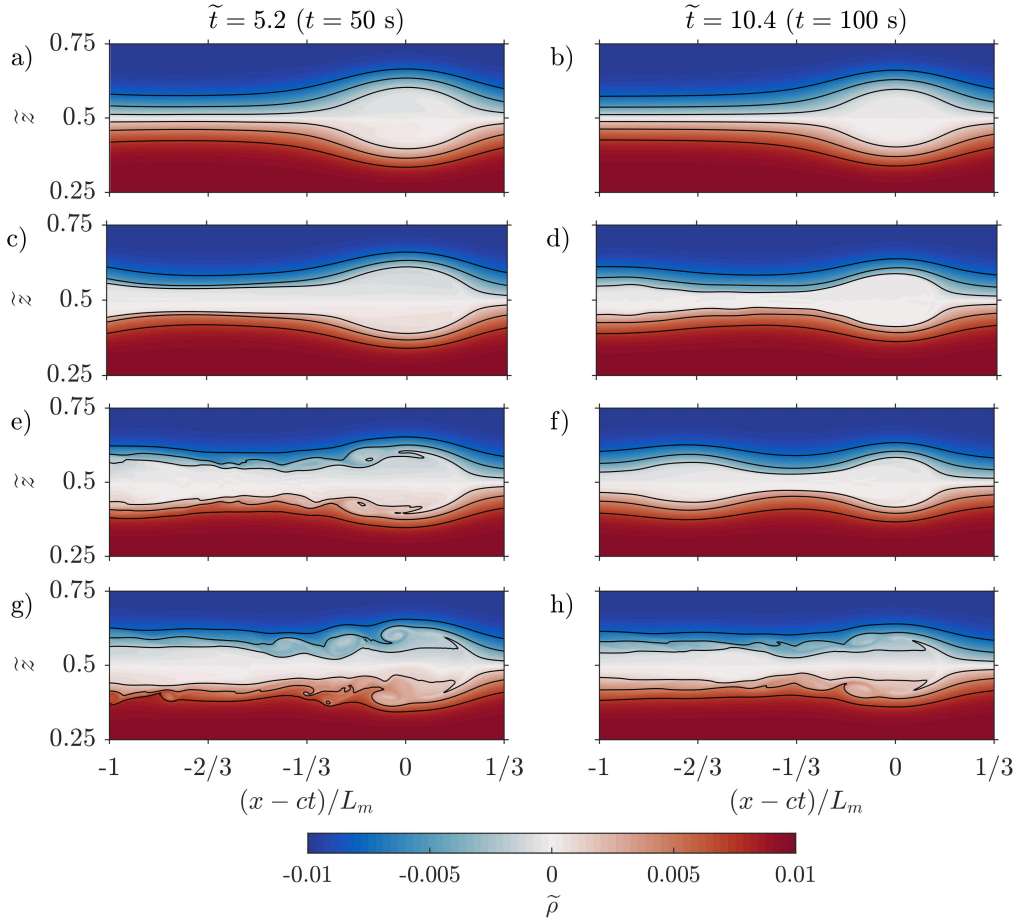

Figure 4.9: Density anomaly, $\widetilde{\rho}$, at $\widetilde{y} = 0$ for f/f_0 = a,b) 0 c,d) 1/4 e,f) 1/2 g,h) 1. Black contours are equispaced isopycnals between $\rho(z_0 - h)$ and $\rho(z_0 + h)$. All cases have Sc=10.

lower minimum amplitude remains an open problem, but it likely has to do with the mass and energy flux towards the focusing region discussed in the previous section.

As time progresses, the wave sheds energy and mass in the shear instabilities until reaching a critical amplitude, after which the wave continues to decay because of the lossy behaviour of the core region of large amplitude mode-2 ISWs [Deepwell and Stastna, 2016] and chapter 3. At $\widetilde{t} = 10.4$ ($t = 100$ s), only the highest rotation rate still produces shear instabilities. In comparison, the non-rotating case is laminar and time-invariant, apart from small dissipative effects for all times. The weaker rotation rate cases do not exhibit instabilities at later times, but rather the mass from the shed vortices has formed the

Kelvin wave tail. This wave is also immediately apparent from figure 4.3 which shows the kinetic energy within this wave directly behind the leading Kelvin wave. Over time the lower rotation rates show that this Kelvin wave tail obtains energy from the leading wave and eventually overtakes it. At the highest rotation rate, the shear instability remains active for the entire simulation which makes it difficult for this wave to form.

The emergence of shear instabilities is correlated with the rotation rate. That is, a higher rotation rate is associated with an earlier shear instability. The higher rotation causes greater fluid to be directed towards the focusing wall which leads to a greater initial amplitude which creates favourable conditions for shear instabilities. Though the initial amplitude is correlated with rotation rate (figure 4.10), the three fastest rotations result in similar wave amplitudes as the experiment continues. This leads to the interesting question of whether Kelvin waves have a stability restriction based on their amplitudes, though the form of their creation here (as a collapse of a span-wise invariant perturbation) greatly impacts the dynamics, especially with the K-H billows.

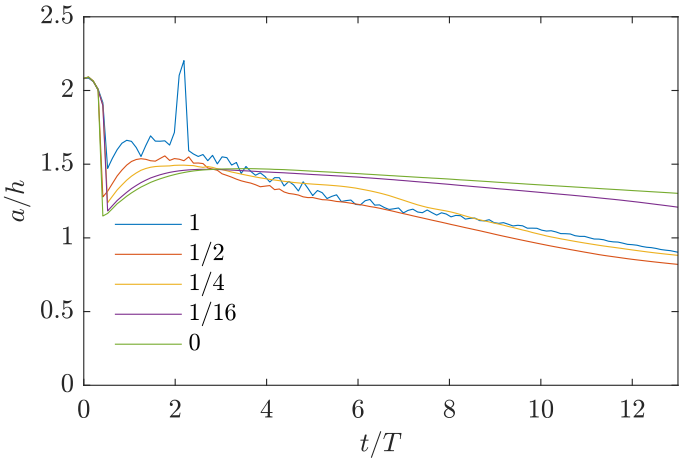

Figure 4.10: Wave amplitude as a function of time for different rotation rates (f/f_0 in legend). All cases have Sc=10.

The wave amplitude decay rate,

$$a' = -\frac{T}{h}\frac{da_w}{dt}, \tag{4.6}$$

increases with rotation rate (table 4.2, and figure 4.10). At larger rotation rates this is a result of a greater initial amplitude, while slower rates create far less K-H billows and the

associated loss of mass. At $\widetilde{t} = 5.2$ ($t = 50$ s), the kinetic energy within the leading wave increases with rotation rate (first column of figure 4.11). The kinetic energy also becomes localized in space at the K-H billows. At later times, The kinetic energy has decreased most substantially in the higher rotation rates because of the shear instabilities.

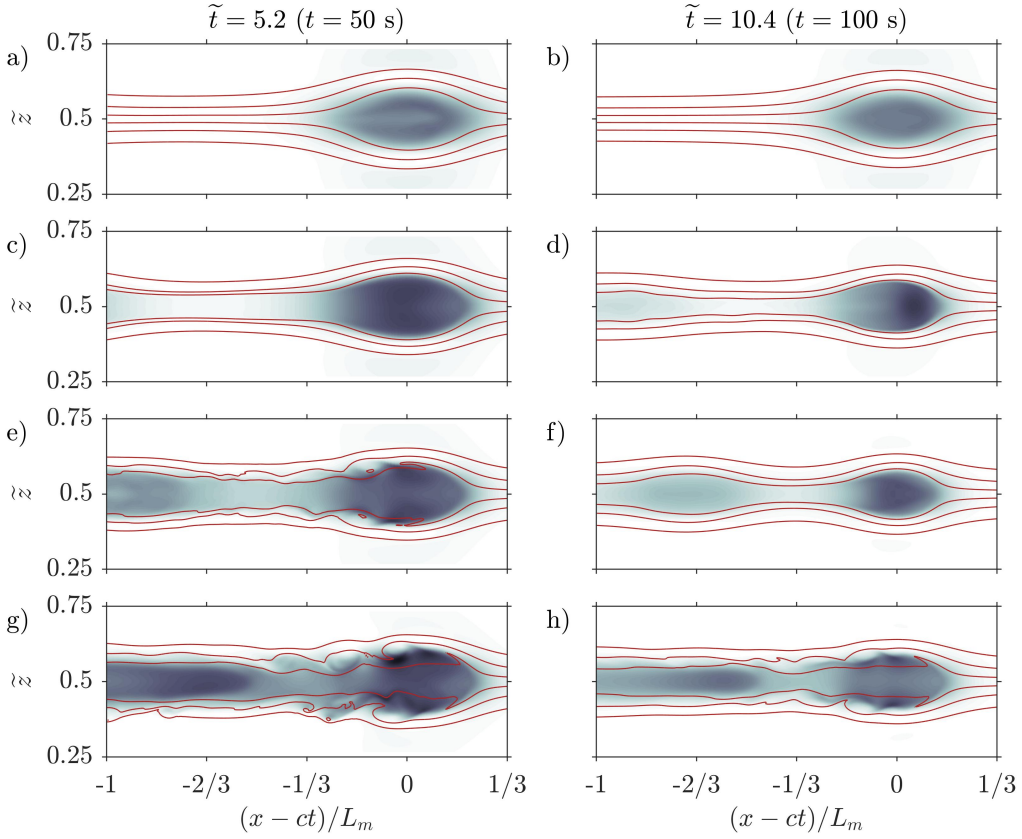

Figure 4.11: Kinetic energy density at at $\widetilde{y} = 0$ for f/f_0 = a,b) 0 c,d) 1/2 e,f) 1. Red contours are the same as in figure 4.9. All cases have Sc=10.

Figure 4.12 shows the kinetic energy slices in the $\widetilde{y} - \widetilde{z}$ plane at the crest of the Kelvin wave (ISW in the non-rotating case). The case of no rotation has an essentially span-wise invariant wave front, whereas the rotation breaks the symmetry by curving the wave front. Along the cross-section of maximum amplitude this appears as an exponential decay of the wave amplitude. Essentially all of the kinetic energy resides within the characteristic isopycnals, $\rho(z_0 \pm h)$. Furthermore, the density overturns resulting from the instabilities are correlated with the locations of maximum KE.

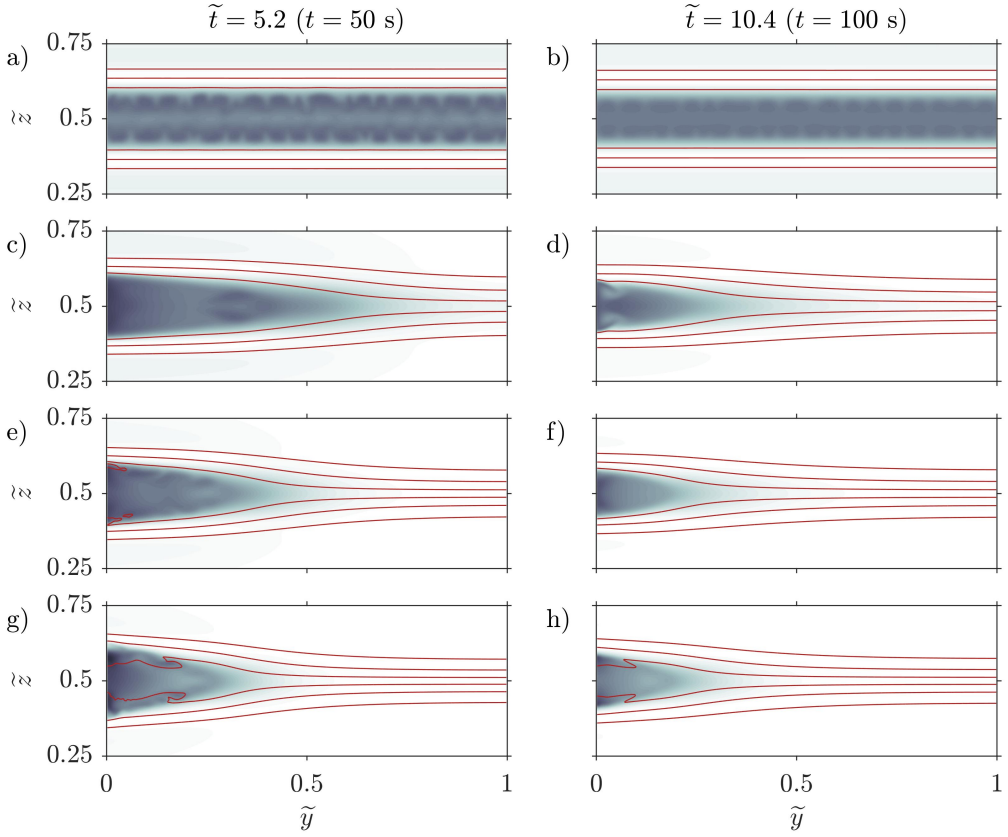

Figure 4.12: Kinetic energy density at the location of maximum amplitude for f/f_0 = a,b) 0 c,d) 1/4 e,f) 1/2 g,h) 1. Red contours are the same as in figure 4.9. All cases have Sc=10.

Over time, due to the radiation of energy into trailing waves, the leading Kelvin wave reduces in amplitude, span-wise width, and KE. The time dependent nature of the width, and thus the exponential decay, results in an increased localization of KE along the focusing wall (seen very clearly in the second row of figure 4.12). This is true along the cross-section of maximum amplitude where the decaying Kelvin wave applies. In the curved portion of the leading wave, this coincides with a simple reduction of the width of the curved wavefront.

Maxworthy [1983] found that the measured Rossby radius of deformation, L_M, (that is, the distance from the wall for the amplitude to drop by a factor of e) was a factor of two smaller than the calculated Rossby radius, L_c. Only the highest rotation rate has L_M smaller than the width of the channel for us to make a comparison. Case 10_1 has the

factor being close to 2.6, which is comparable. This does not appear to be the case at lower rotation rates since these cases have their amplitudes decay over the entire channel width even though the Rossby radius increase by up to a factor for 4. This could be due to the narrowness of the channel compared to the Rossby radius or more likely a difference in measurement technique. Maxworthy [1983] made their estimate based on the projection of the wave field onto the $\widetilde{y} - \widetilde{z}$ plane. This would lead to a weaker decay rate since the wave curves backwards away from the cross-section with a fixed $\widetilde{x}$ at which our estimate is made. In other words the method of Maxworthy [1983] integrates in the along tank direction, while we choose a particular stream-wise location for our estimate.

4.4 Results: Schmidt number dependence

The shear instabilities and associated dynamics are fundamentally small scale behaviour which are damped by viscosity and smeared by diffusion, both of which are determined by the properties of the fluid, namely the molecular diffusivity and the viscosity. Experimentally, the diffusivity is fixed by the choice of stratifying solute. Physical values of a salt stratified experiment, which are typical for experiments of this type, give a Schmidt number of approximately 700. Since direct numerical simulations at these values are unattainable due to the resolution required, we provide here a short description of the impact that various Schmidt numbers have on the results presented thus far.

For longer simulations, such as the ones conducted here, the pycnocline will diffuse causing the waves to propagate in a slightly different stratification near the end of the simulation compared to the beginning. Smaller Schmidt numbers have greater diffusion causing a greater impact (figure 4.13a). The $\mathrm{Sc} = 1$ case had the pycnocline grow by 70% while the $\mathrm{Sc} = 10$ case only grew by 10%. The background stratification at the end of the experiment is noticeably different (figure 4.13b).

We find that the wave amplitude is unaffected when compared at various Schmidt numbers. The general features characterizing the wave are thus fairly similar at $\widetilde{t} = 5.2$ ($t = 50$ s) (figure 4.14). The details, however, are significant enough to warrant comment. All Schmidt numbers experience the shedding of Kelvin-Helmholtz billows, but in the lowest Schmidt number case formation ceases at around $\widetilde{t} = 11.7$ ($t = 112$ s) while the other two cases never stop. Since the stratification has broadened in this case, the Richardson number has increased leaving the unstable region for shear instabilities to form.

The span-wise profile of the wave also shows the difference (right column of figure 4.14). The highest Schmidt number case has overturning which is not present in the

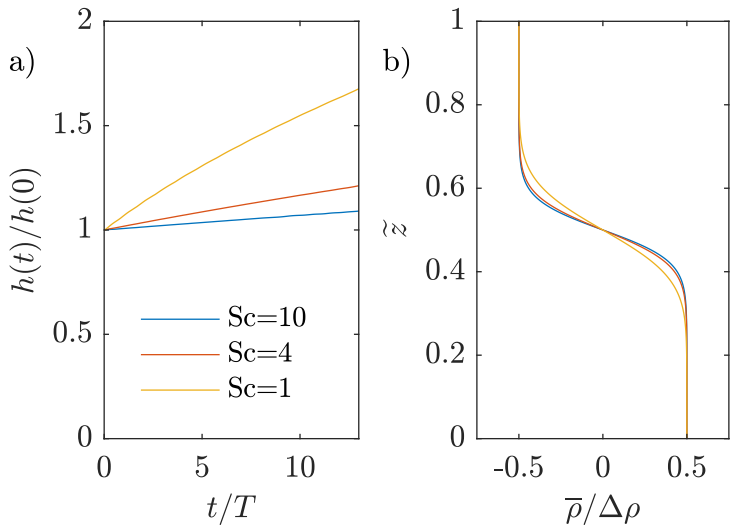

Figure 4.13: a) Pycnocline half-width as a function of time for different Schmidt numbers. b) The background stratification at $t/T = 12.5$ ($t = 120$ s).

lowest Schmidt number case. These features are secondary to the over-all behaviour. For example, the total kinetic energy is comparable between all cases at a given rotation rate but remains consistently weaker for lower Schmidt number. The greatest separation between the Sc=1 and Sc=10 case is 13%. As this ratio is only expected to grow as Sc increases, the difference between typical simulations of Sc=1 or Sc=7 are bound to misrepresent the smaller dynamical features of an equivalent physical experiment.

In the $f/f_0 = 1/2$ rotation rate cases (comparison not shown) the differences are more obvious. The density field does not clearly show the Kelvin wave tail in the Sc=1 case. Rather, the wave is of such small amplitude that it is nearly indistinguishable compared to the pycnocline width. Only by looking at the vertically integrated KE does the wave appear, but is of considerably smaller magnitude. The fanning structure seen in figure 4.4 also goes from at least two branches in case 10_1/2 to one in case 1_1/2. This results in a different Poincaré wave field in the majority of the domain.

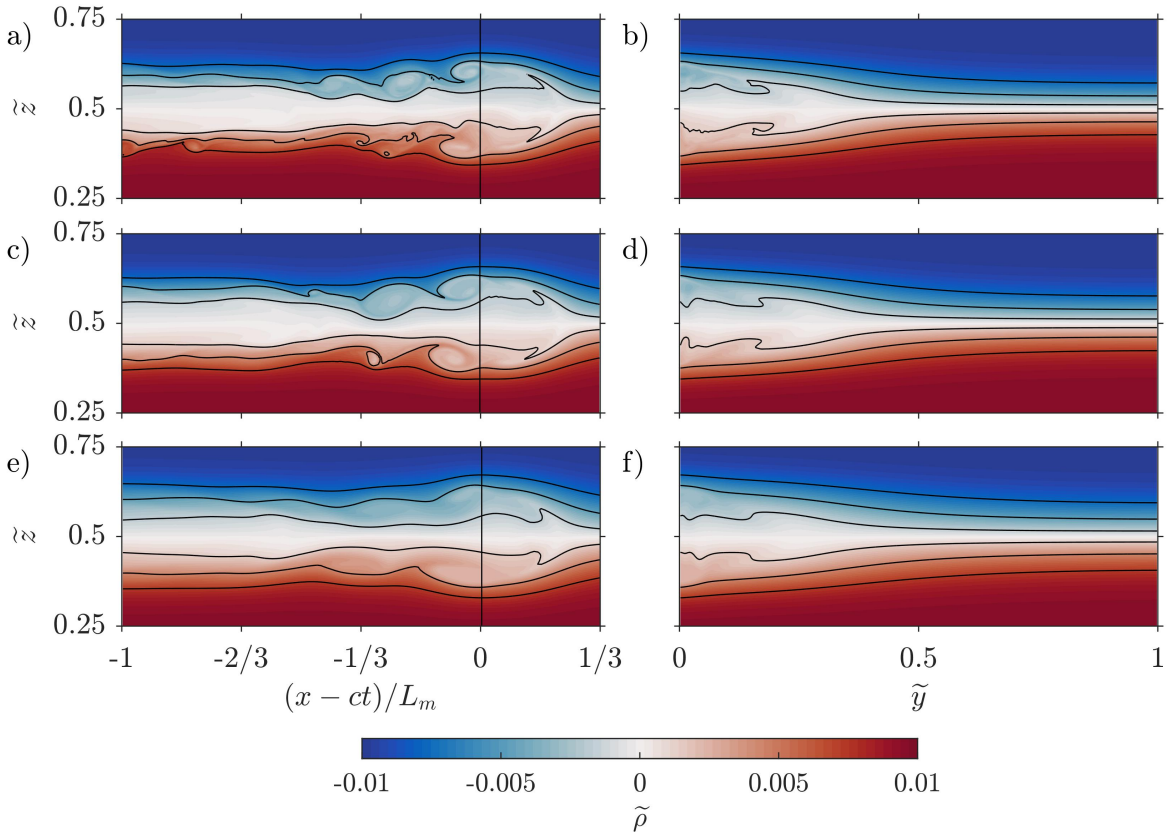

Figure 4.14: Density anomaly, $\widetilde{\rho}$, at $\widetilde{t} = 5.2$ ($t = 50$ s) with cross-sections at $\widetilde{y} = 0$ (first column) and at the location of maximum amplitude (second column) for Sc = a,b) 10 c,d) 4 e,f) 1. Black contours are the same as in 4.9. Vertical, black line denotes location of the cross-section shown in the right column. All cases have $f/f_0 = 1$.

4.5 Conclusions

We have performed a series of numerical experiments of a lock–release configuration exploring the effects that rotation and side walls have on the evolution of mode-2 ISWs. When the stratification has a single pycnocline form, naturally occurring mode-2 waves are quite likely to exhibit regions of overturning and hence our configuration is ideal for exploring the combined effects of rotation and instability. Matching with the results of Maxworthy [1983], we observe that the leading wave becomes curved by rotation and that the dominant instability takes the form of two K-H billows at the crest of the wave, above and below the pycnocline center. By modifying the rotation rate we observe that as the rate of rotation

increases the instabilities become more energetic. This appears to be due to increased focusing of mass and the kinetic energy density along the focusing wall, especially in the early period of adjustment after the lock is released. Since these type of shear instabilities are most commonly formed by large amplitude waves, this suggests that channel trapped waves have a lower minimum amplitude threshold for instability generation and thus will have smaller amplitude waves compared to internal solitary waves in the open ocean.

These instabilities cause the leading wave to lose energy and thus higher rotation rates result in a faster decay in wave amplitude than cases with a lower rotation rate. The increased instability generation along the side wall also serves to create an asymmetry in the extent of mixing across the width of the tank. This effect could be observed in fjords or narrow lakes by making a careful comparison of mixing levels and wave amplitudes across the channel.

The high level of mass and kinetic energy along the focusing wall also resulted in the radiation of Poincaré waves, as previously described by Sánchez-Garrido and Vlasenko [2009]. The Poincaré waves reflect off the opposing wall before returning to resonantly generate the secondary Kelvin wave along the focusing wall. When compared against an equivalent non-rotating case we found that this generation mechanism (through resonance) at higher rotation rates was completely different from the creation of secondary ISWs in a non-rotating reference frame. We referred to this wave as the secondary Kelvin wave. In addition to this, a Kelvin wave tail formed from the remains of the focused mass and energy along the wall. During propagation, we observed that the leading Kelvin wave appeared to lose energy to the both of these Kelvin waves, each of which became more energetic and thus faster. Eventually, these trailing Kelvin waves will overtake and surpass the leading wave. The results observed are fundamentally different than those seen without side walls. In the case without the side walls the leading wave energy is deposited into the trailing waves through dispersion eventually forming a wave packet. This packet has no span-wise variation. With side walls, the trailing waves are a fan of Poincaré waves that exhibit a complex interference pattern and hence have a span-wise structure. Furthermore, the energy of the leading wave is not continuously being lost to the primary trailing wave and hence this wave lives significantly longer, compared to the non-rotating case..

The results presented above suggest two clear avenues for future work. One avenue would focus on the rotation modified instability region. While in the above, clear evidence of transitional behaviour was presented, it is unclear to what extent a truly turbulent state was achieved. This is because trapping by the leading Kelvin wave is incomplete and turbulence may lose energy due to a spreading in space. Moreover, while the resolution of the numerical simulations was excellent for the full domain, a study that is focused on turbulent transition could optimize the domain and stratification parameters. For example,

the domain could be shortened and the initial perturbation increased in size to increase the wave amplitude. A second possible avenue for future work would explore the effect of the span-wise extent. Figure 15 of Sánchez-Garrido and Vlasenko [2009] suggests that for wider domains, mode-1 Kelvin waves yield Poincaré wave trains whose focusing yields Mach stems on the far wall. We did not observe this phenomenon in our simulations, but it is possible that our span-wise extent was simply not large enough to achieve this. Of course, an experimental realization of our simulations would provide both a test of our results, and suggestions for future numerical studies that are most relevant to the experimentalist.

4.6 A supplemental perspective with an ultra-high resolution simulation

The resolutions used in the chapter thus far have been sufficient for the analysis conducted as it depends on primary variables, namely the velocities and density fields. However, the Kelvin-Helmholtz billows lead to strongly three-dimensional flows, with considerable enstrophy, viscous dissipation and mixing. To ensure that secondary variables, namely those derived from the velocity gradient matrix or the gradient of density, are well resolved we have increased the resolution for case 10_1 to that listed in table 4.4. In comparison to the previous run, the resolution has been doubled in the x and y dimensions.

Table 4.4: Numerical resolution of the high resolution of case 10_1.

N_x	N_y	N_z	Δx (mm)	Δy (mm)	Δz (mm)
8192	512	512	0.78	0.78	0.59

Firstly, the density field (Figure 4.15a) shows the three-dimensional curvature of the wave front in addition to the chaotic turbulence in the aft of the wave along the focusing wall. There is an evident change from laminar flow into the Kelvin-Helmholtz billows which in-turn becomes the turbulent region. This transition occurs at the crest of the wave where the Richardson number is near a maximum, while only forming within a short distance from the focusing wall (the near pane). This turbulent region has a lasting impact on the stratification for multiple wavelengths behind the wavefront. Sufficient distance from the focusing wall the wave returns to laminar flow.

Comparison to the non-rotating case (Case 10_0, Figure 4.15b) shows just how different these are spatially. Both figures are on the same scale and viewed at the same point in

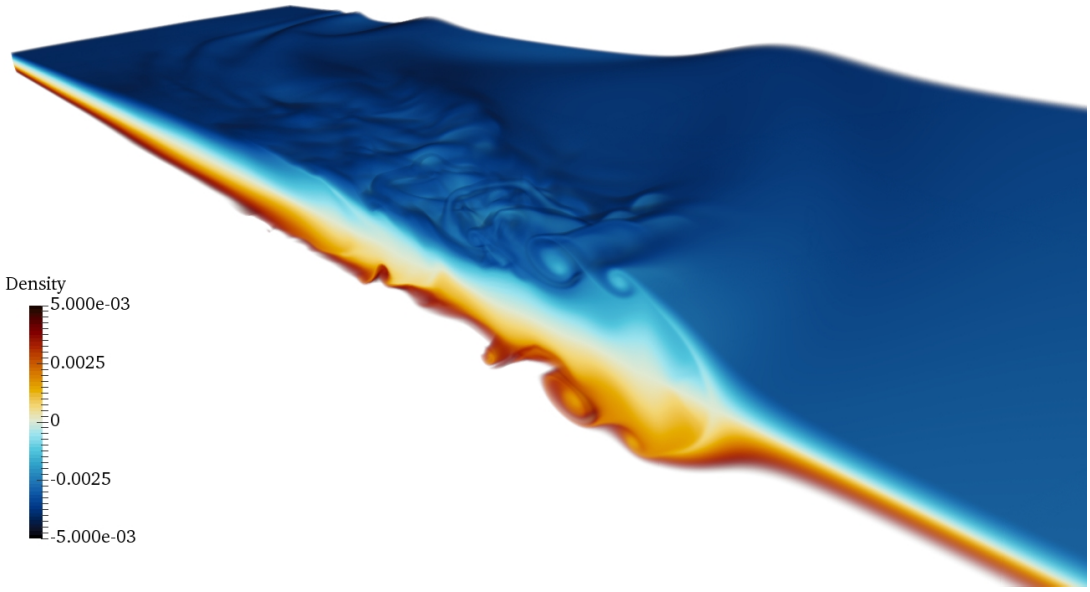

(a) Density at $t = 38$ s for the high resolution version of case 10_1.

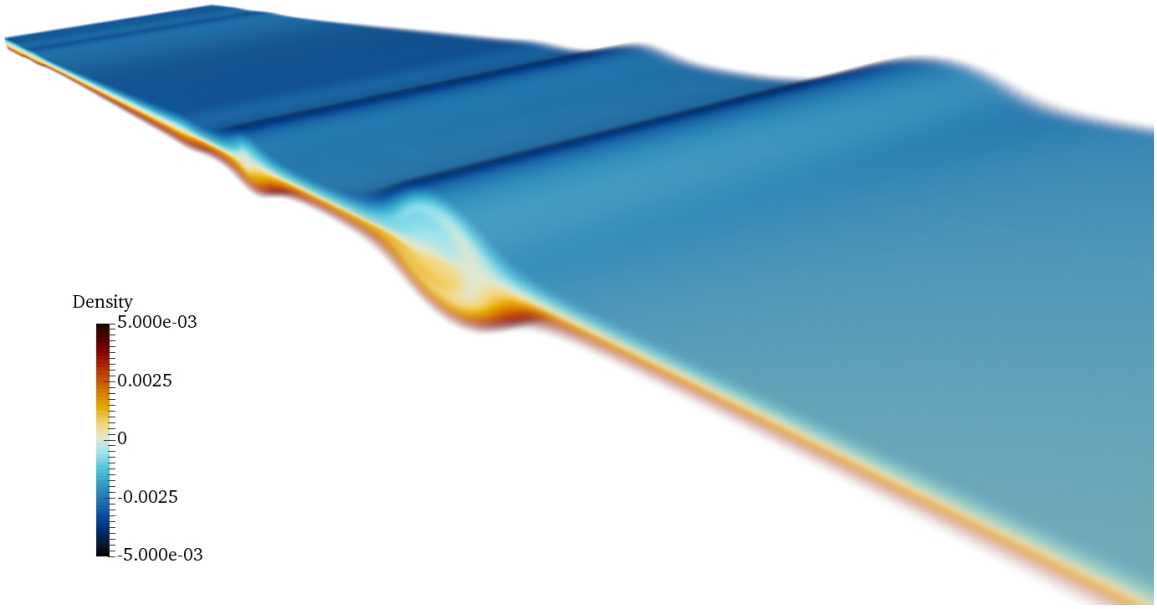

(b) Density at $t = 38$ s for case 10_0.

Figure 4.15: Comparison of density anomalies for cases a) high resolution 10_1 and b) 10_0. The viewing angle is from ahead, and above the ISW, from the outside of the focusing wall.

space (ahead, and above the ISW, from the outside of the focusing wall). The non-rotating case is smaller in amplitude, completely laminar, and has travelled a lesser distance. There is essentially no three-dimensionality in the non-rotating case. It is clear that rotation has had a drastic impact on this coastally trapped ISW in regard to the structure of the ISW and the initialization of turbulent eddies.

The enstrophy (Figure 4.16a) further emphasizes the location of maximum vorticity, which we will use as a proxy for three-dimensionalization and mixing. The strongest vorticity is, unsurprisingly, within the KH billows. Due to the vertical symmetry, the KH billows above and below the centre of the pycnocline are equal in strength and location while they are being formed. Once the KH billow is left in the wake, the vertical symmetry in the enstrophy breaks down in the usual turbulent cascade phenomenon. The strength of the mixing however remains quite strong for multiple wavelengths behind the wave. The dissipation (Figure 4.16b) is relatively similar to the enstrophy, in that the regions of maximum enstrophy and dissipation are roughly in the same location. This is unsurprising since the maximum velocity (and the gradient of velocity) exists in the turbulent region.

A more careful comparison between the viscous dissipation and the enstrophy is completed through the Q criterion. Initially proposed by Hunt et al. [1988], the Q criterion is useful for measuring the relative strengths of both the strain and the vorticity [Davidson, 2006]. Formally, Q is defined as

$$Q = \frac{1}{2}\left(W_{ij}W_{ij} - e_{ij}e_{ij}\right) \tag{4.7}$$

where $W_{ij} = \frac{1}{2}(\frac{\partial u_i}{\partial x_j} - \frac{\partial u_j}{\partial x_i})$ is half the rotation tensor, and e_{ij} is the strain rate tensor [Kundu et al., 2012]. Based on the definitions of viscous dissipation and the rotation tensor, (4.7) can be written as

$$Q = \frac{1}{2}\left(\Omega - \frac{\epsilon}{2\mu}\right). \tag{4.8}$$

The Q criterion (figure 4.16c) shows clear regions of both high enstrophy (red) and high strain (blue). In the front portion of the wave (ahead of the KH billows) Q is approximately zero indicating that the dissipation matches the vorticity. Regions where Q has large magnitude exist only once the Kelvin Helmholtz billows have formed. The KH billows are indicated by large Q which are then paired with high strain during the breakdown of the billows.

The span-wise structure of the enstrophy is highly variable; from maximal mixing on and near the focusing wall, to minimal vorticity on the far wall (figure 4.17). Within the wavefront there is a correlation with decreasing Kelvin wave amplitude and local enstrophy

(a) Enstrophy.

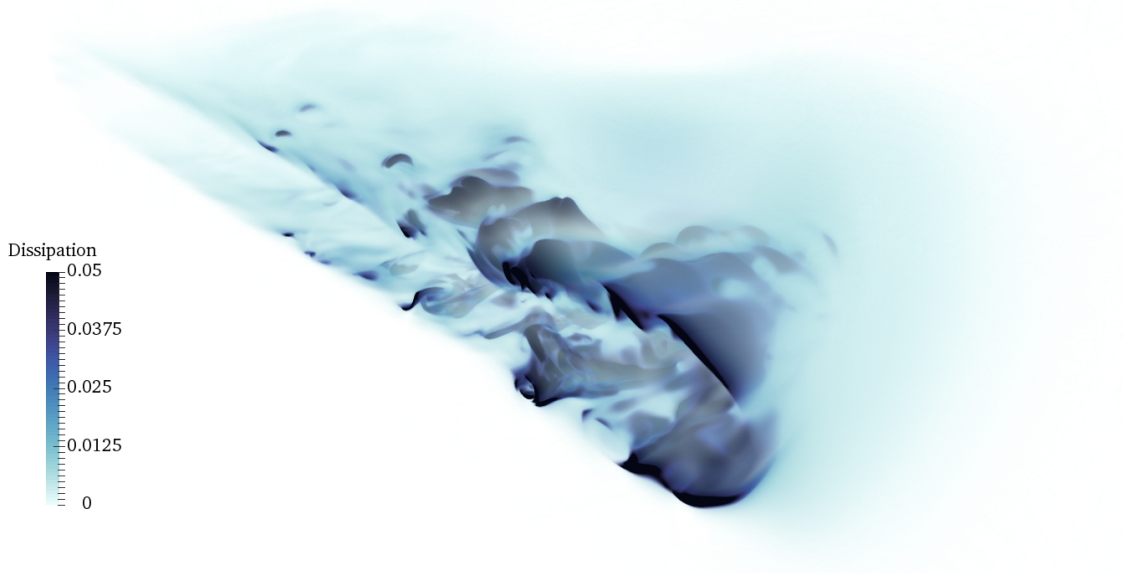

(b) Dissipation.

Figure 4.16: a) Enstrophy b) dissipation and c) Q criterion at $t = 38$ s for the high resolution version of case 10_1. The viewing angle is similar to that of figure 4.15.

(c) Q criterion.

Figure 4.16: a) Enstrophy b) dissipation and c) Q criterion at $t = 38$ s for the high resolution version of case 10_1. The viewing angle is similar to that of figure 4.15.

(figure 4.17c). Figure 4.17b indicates that this mixing does not exist within the core of the Kelvin wave, but rather along the edges of the pycnocline ($\rho(t = 0, L_x, z_0 \pm h)$). Though the extent of the pycnocline is not shown, its border is approximately on the edge of the high enstrophy region of the wavefront. We can also see that the turbulent wake does not extend further from the focusing wall than the initial distance within which it was formed. So even though the mixing is quite vigorous, until this point in time, it has not spread spatially across the channel at any significant rate. The turbulence, however, is left behind in the wake of the Kelvin wave where spatially small, energetically weak, turbulent bursts continue to appear.

The total enstrophy (figure 4.18a) shows which components experience the highest rotational energy. The y-component of enstrophy is the largest, in accordance with an internal wave traveling in the x-direction. By $t = 10$ s there is vorticity in the x and z directions indicating that the wavefront has begun to 'bend' because of the rotation. Around $t \approx 15$ s all components of enstrophy rapidly increase in size at which time the first Kelvin-Helmholtz billows have formed and begin to degrade through secondary instabilities and vortex stretching and tilting. The enstrophy peaks around $t = 20$ s, after which the wave begins to slowly stabilize, though KH billows are formed for the duration of the

(a) Top view.

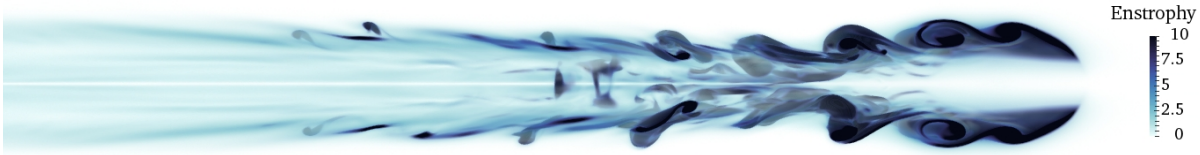

(b) Side view.

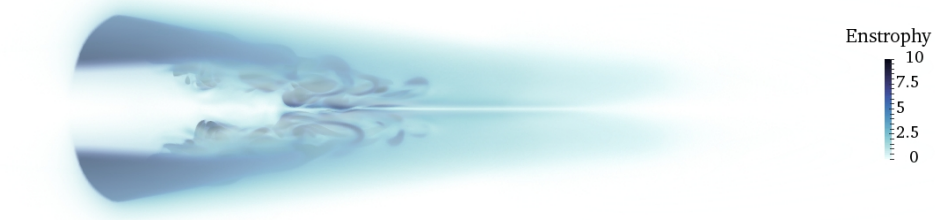

(c) Front view.

Figure 4.17: Enstrophy at $t = 38$ s for the high resolution version of case 10_1.

simulation.

Interestingly, the x-component of enstrophy (vorticity which is oriented along the channel) is consistently 2-3 times larger than the z-component (vertically oriented). We hypothesize that this is a result of the vertical length scale being smaller than the horizontal length scales. A scale analysis of the vorticity components shows that the x-component of vorticity will therefore be larger than the along channel component, while being smaller than the across channel component because the along channel velocity is considerably bigger than the other components (figure 4.18b).

The kinetic energy (figure 4.18b) is dominated by along channel flow. The vertical and across channel flow are roughly an order of magnitude smaller with the across channel flow being consistently larger than the vertical.

In conclusion for this section, the mixing is a direct result of the rotation causing a flux of mass and energy towards the focusing wall. This mixing is caused by the formation and degradation of Kelvin-Helmholtz billows which are localized near the wall and along the edge of the pycnocline.

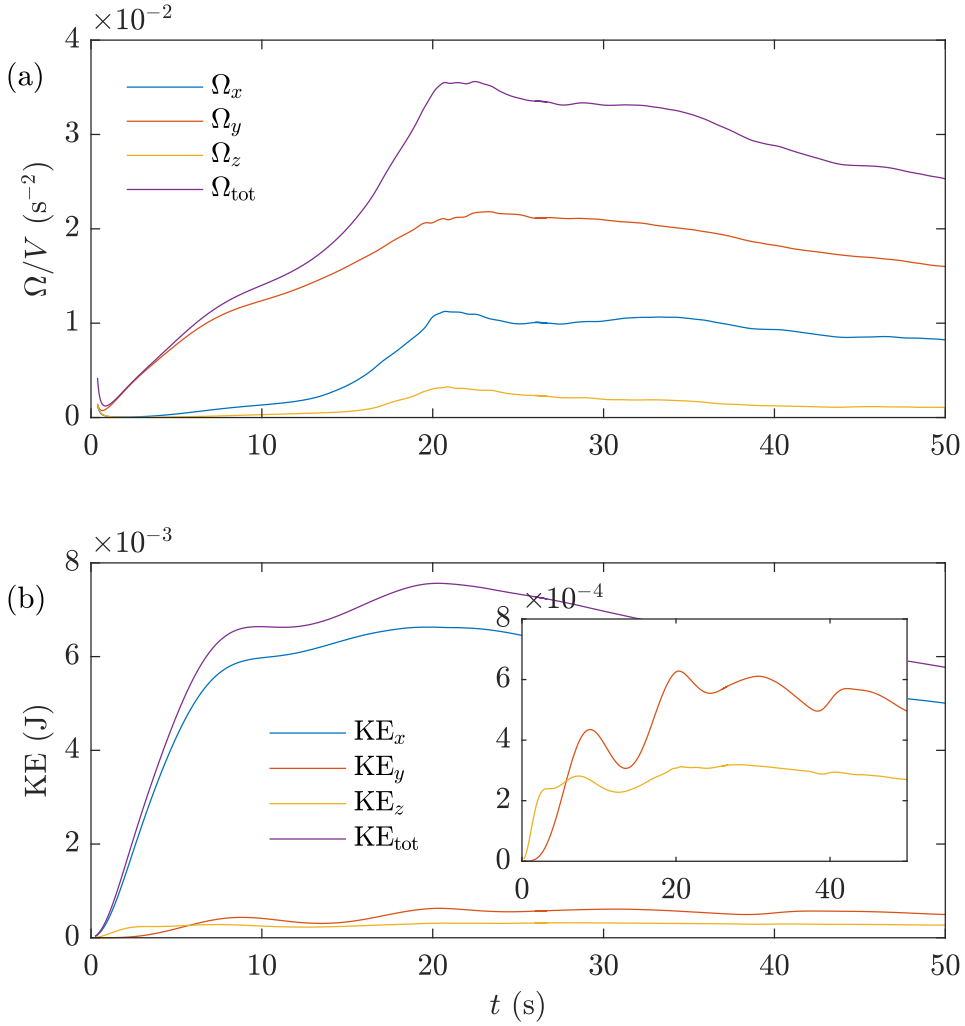

Figure 4.18: a) Enstrophy and b) kinetic energy components versus time of the high resolution case 10_1. Insert in b) magnifies KE_y and KE_z which are and order magnitude smaller than KE_x.

Chapter 5

Interaction of mode-2 ISW with narrow topography

The following chapter has appeared as a publication in *Physics of Fluids* [Deepwell et al., 2017]. Numerical simulations, laboratory experiments, analysis, and writing was completed by D. Deepwell. The laboratory experiments were supervised by M. Carr. The laboratory equipment was provided by P. Davies. Project supervision was given by M. Stastna. Each co-author helped edit the text and write a few paragraphs.

5.1 Introduction

Until now, the majority of both the physical and numerical literature on mode-2 waves has been devoted to mid-depth centred waves with flat bottom boundaries [Brandt and Shipley, 2014, Davis and Acrivos, 1967, Terez and Knio, 1998, Sutherland, 2002, Mehta et al., 2002, Salloum et al., 2012, Stamp and Jacka, 1995]. These studies have expanded upon the original weakly non-linear theory by Benjamin [1967], and have described the characteristics of large amplitude mode-2 waves. Behavioural characteristics such as the wave speed, amplitude, and wavelength are now reasonably well understood for mode-2 waves within a constant fluid depth in the weakly non-linear to the strongly non-linear regime. The mass transport capabilities have also been extensively discussed in the literature [Salloum et al., 2012, Brandt and Shipley, 2014, Terez and Knio, 1998, Deepwell and Stastna, 2016]. Deepwell and Stastna [2016] found that the transport efficiency has a strong dependence on Schmidt number, as well as stratification. Optimal parameters were found that reduced the effect of instabilities on the wave's trapped core.

Two papers have discussed behaviour in layers of unequal depth [Carr et al., 2015, Olsthoorn et al., 2013]. Both articles found that even a small off-set of the pycnocline from the mid-depth led to significant asymmetry in the wave core which contributed to an increase in instabilities therein. A strong off-set was also associated with the introduction of a mode-1 wavetrain trailing the mode-2 wave.

Recently, Terletska et al. [2016] presented numerical simulations of mode-2 ISWs traveling over a step. Depending on the size of the step, the incident mode-2 was either unaffected, severely adjusted but reformed a smaller mode-2 wave, or destroyed but formed a mode-1 wave in the process. Mode-1 breather-like internal waves or mode-1 wavetrains were formed in all cases. In the weakly non-linear regime, Belogortsev et al. [2013] investigated the run-up of a mode-2 ISW onto a slope. Depending on the stratification the initial convex mode-2 ISW either remained convex but was deformed, or was converted into a train of concave mode-2 ISWs.

We present, what we believe, to be the first experimental descriptions of shoaling mode-2 ISWs. Associated numerical simulations are also analyzed and compared. Rather than looking at the long term impact of shoaling on the wave, we focus on the interaction of the wave with the topography, specifically in terms of particle resuspension and vorticity generation.

While the literature for shoaling mode-2 waves is now in its infancy, much can be learned from the shoaling mode-1 literature which has been predominantly concerned with waves traveling onto a shelf or slope (see Lamb and Xiao [2014] and the references therein). Though this is an important topic worthy of being studied in the future, we chose to first investigate mode-2 shoaling over an isolated ridge because of the ability to directly measure the impact that topography of a certain amplitude and slope will have on the evolution of the mode-2 ISW without the wave being completely destroyed. Many studies of shoaling mode-1 waves show heightened activity on the upstream side of the topography (Sveen et al. [2002] for example). Using a ridge captures this wave-topography interaction while also investigating the long time behaviour of the wave once it has passed over the hill and returned to the original fluid depth.

Experiments on shoaling mode-1 ISWs indicate that such waves often pass through a critical point causing the wave to change polarity [Cheng et al., 2011]. This often results in local overturning, vorticity generation, and heightened turbulent mixing. In general, there has been much discussion on all aspects of shoaling mode-1 waves, but essentially nothing for mode-2 waves.

A few papers have discussed shoaling mode-1 ISW over a ridge [Sveen et al., 2002, Guo et al., 2004, Hult et al., 2009, 2011a,b, Zhu et al., 2016]. Many of these have described

the wave-hill interaction within three categories: weak, moderate, and strong. Strong interaction has been associated with a change in polarity causing the wave to break. This breaking led to strong vorticity generation causing particle resuspension to occur [Sveen et al., 2002]. It is this tracer resuspension that will be a central theme of this chapter.

To ensure no possible confusion in the remainder of this chapter, the terms experiments and simulations will be used to indicate the completed physical experiments and numerical simulations, respectively.

The structure of this chapter is as follows. Section 5.2 describes the numerical techniques and configuration used to create a mode-2 ISW. Section 5.3 will discuss the numerical results of the interaction of the mode-2 ISW with the isolated ridge. Particular focus will be placed on the vortex dynamics and boundary layer resuspension. Section 5.4 will compare the numerical results with matching laboratory experiments. Section 5.5 outlines a criteria for categorizing the wave-hill interaction based upon the initial configuration. Finally, section 5.6 will summarize the presented work.

5.2 Numerical methods and experimental configuration

We again use (1.1) as our governing equations with the added passive tracer field, T, governed by,

$$\frac{DT}{Dt} = \kappa_T \nabla^2 T. \tag{5.1}$$

To model the formation and progression of a mode-2 ISW we have used the Spectral Parallel Incompressible Navier-Stokes Solver (SPINS), the details of the construction and validation of which are described in Subich et al. [2013]. No slip boundary conditions were used in the vertical (top and bottom boundaries) through the use of Chebyshev grids to cluster points within the boundary layer. The free slip condition was used in horizontal directions by using Fourier grids. Time dependent simulations were completed on the high-performance computer cluster SHARCNET (www.sharcnet.ca).

The isolated topography consists of a single Gaussian hump,

$$h(x) = A_{\text{hill}} \exp\left[-\left(x - x_0\right)^2 / \sigma_{\text{hill}}^2\right]. \tag{5.2}$$

where the origin was chosen so that $x = 0$ and $z = 0$ coincided with the upstream (left) end of the tank and the top of the tank, respectively. The hill parameters, given in Table 5.1,

Table 5.1: Hill parameters.

A_{hill} (m)	x_0 (m)	σ_{hill}
0.10	4.8	0.10

remained unchanged for all simulations and experiments. The aspect ratio, $A_{\text{hill}}/\sigma_{\text{hill}} = 1$, is large compared to typical topographical features in the ocean. Therefore we describe this hill as narrow. The maximum slope of 0.86 is steeper than the slope of 0.33 used in Sveen et al. [2002] and Guo et al. [2004], but is much smoother than the step function used by others [Maderich et al., 2010, Talipova et al., 2013, Terletska et al., 2016]. Wave-hill interaction with broader topography will be discussed in an upcoming journal article.

We have checked for numerical convergence by conducting grid coarsening studies. As this is a spectral method, the spatial order of accuracy of the simulation is equivalent to the number of grid points in each dimension. We thus require that an important small feature have a sufficient number of grid cells. If this is not the case, sharp gradients may not be adequately handled by the spectral method and can cause unphysical growth of a field. In particular, this can occur in the density field. In addition to the grid coarsening studies, we have checked to make sure that the density field does not increase above its initial maximum nor below its initial minimum.

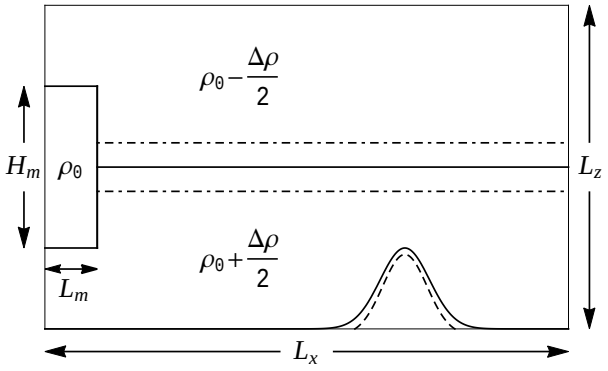

Figure 5.1: Initial tank configuration. Horizontal lines denote the location of the pycnocline centre (solid line), and pycnocline half-width (semi-dashed lines).

The majority of the tank contains a background stratification consisting of a hyperbolic tangent profile,

$$\bar{\rho}(z) = \rho_0 - \frac{\Delta\rho}{2} \tanh\left(\frac{z - L_z/2}{d}\right), \tag{5.3}$$

where $\Delta\rho$ is the density difference between the top and bottom layers of the stratification, d is the pycnocline half-width, and L_z is the total fluid depth. A mode-2 ISW is formed by releasing a region of intermediate density, ρ_0, into this background stratification. This region is centered on the pycnocline and has height, H_m, and width L_m (Figure 5.1). The ratio of the intermediate region, H_m/L_m, sets the number of rank ordered mode-2 ISW to be formed [Maxworthy, 1980]. This configuration is chosen to match that of the initial configuration of physical experiments also completed.

The domain for both the numerical and physical experiments was a long, narrow, rectangular channel with the dimensions given in Table 5.2. Most simulations are two-dimensional (2D). A couple three dimensional (3D) simulations (not listed) were also completed but showed little difference from those in two dimensions. The fluid depth varied between 0.25 m and 0.40 m.

Table 5.2: Tank dimensions and resolution.

Case	L_x (m)	L_y (m)	L_z (m)	N_x	N_z	Δx (mm)	$\Delta z_{\max}$ (mm)
Num.	6.4	-	varied	4096	384	1.56	1.23
Exp.	6.4	0.4	varied	-	-	-	-

Following the convention used in previous studies [Salloum et al., 2012, Stamp and Jacka, 1995, Carr et al., 2015], the characteristics describing a solitary mode-2 wave were calculated from the displacement of the $\bar{\rho}(L_z/2 \pm d)$ isopycnals from their original depth (Figure 5.2). The amplitude, a, is the average of the maximum displacement of these isopycnals, and the aft and fore wavelengths are the distance from the maximum isopycnal displacement to the half-maximum. The fore wavelength, λ_f, and the aft wavelength, λ_a, for the width ahead and behind the maximum amplitude, respectively.

As with past literature [Salloum et al., 2012, Stamp and Jacka, 1995, Carr et al., 2015], we define the characteristic length as the pycnocline half-width, d. These articles used the mode-2 linear long wave speed [Benjamin, 1967],

$$c_0 = \frac{1}{2}\left(\frac{gd\Delta\rho}{\rho_0}\right)^{1/2},$$

for the velocity scale, but we have found that this is impractical for large amplitude waves. These waves can easily reach speed twice that of the long wave limit (see Table 5.3). For example, the fastest wave propagates at 5.6 cm/s, or 2.36 when non-dimensionalized. Therefore, we have used the average speed, c, of the wave between the time the wave settled

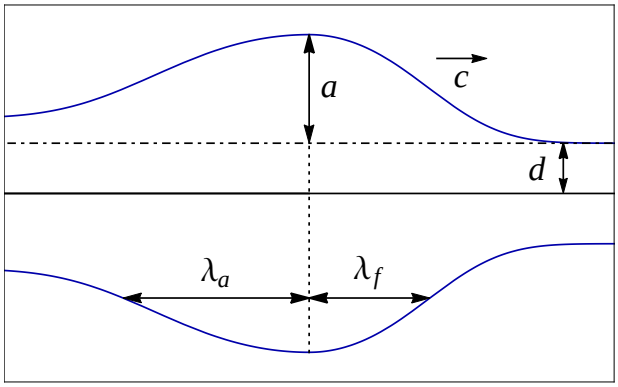

Figure 5.2: Schematic of parameters for a rightward moving mode-2 ISW.

after the collapse and directly before reaching the base of the topography. Therefore, we define the Reynolds number as $\mathrm{Re} = cd/\nu$. The characteristic time is defined in terms of the pycnocline half-width and this velocity scale, $T = d/c$. This then defines the non-dimensional time, $\widetilde{t} = t/T$.

The parameters of the simulations and experiments are listed in Table 5.3. In summary, the fluid depth varied between 0.25 m and 0.40 m, and the intermediate fluid depth varied between 0.04 m and 0.14 m. Within the simulations, the non-dimensionalized density difference was 2.3% which approximates the density differences used in the laboratory experiments. The Schmidt number, $\mathrm{Sc} = \nu/\kappa$, was fixed at 10 for all primary simulations. The effect of adjusting Schmidt number and Reynolds number will be looked at in section 5.3.3.

The interaction can broadly be categorized into three main regimes: weak (W), moderate (M), or strong (S) interaction. The strong interaction exhibits a clear loss of material from the mode-2 wave core and strong separation in the bottom boundary layer (BBL). The moderate interaction is characterized by the creation of a persistent vortex at the hill crest, while the wave is slightly adjusted. The weak interaction leaves the mode-2 ISW essentially unaffected by the transit. These categories are comparable to those in Sveen et al. [2002] who, in the case of a mode-1 wave of depression, described the interaction as wave breaking, moderate, or weak.

Table 5.3: Simulation and experimental parameters.

Case	L_z (m)	L_m (m)	H_m (m)	d (mm)	$\Delta\rho/\rho_0$	c/c_0	a/d	Sc	Re	Interaction
Simulation										
2504	0.25	0.3	0.04	10	0.023	1.37	0.69	10	163	M
2506	0.25	0.3	0.06	10	0.023	1.70	1.47	10	202	S
2508	0.25	0.3	0.08	10	0.023	1.94	2.24	10	230	S
3002	0.30	0.3	0.02	10	0.023	1.12	0.21	10	133	W
3004	0.30	0.3	0.04	10	0.023	1.40	0.75	10	167	W
3006	0.30	0.3	0.06	10	0.023	1.75	1.55	10	207	M
3007	0.30	0.3	0.07	10	0.023	1.89	1.96	10	224	M
3008	0.30	0.3	0.08	10	0.023	2.00	2.33	10	237	M
3009	0.30	0.3	0.09	10	0.023	2.10	2.70	10	249	S
3010	0.30	0.3	0.10	10	0.023	2.17	3.04	10	257	S
3012	0.30	0.3	0.12	10	0.023	2.24	3.48	10	265	S
3506	0.35	0.3	0.06	10	0.023	1.78	1.61	10	211	W
3508	0.35	0.3	0.08	10	0.023	2.05	2.41	10	243	M
3509	0.35	0.3	0.09	10	0.023	2.15	2.79	10	255	M
3510	0.35	0.3	0.10	10	0.023	2.21	3.08	10	263	M
3512	0.35	0.3	0.12	10	0.023	2.29	3.43	10	272	S
4008	0.40	0.3	0.08	10	0.023	2.07	2.45	10	246	W
4010	0.40	0.3	0.10	10	0.023	2.26	3.14	10	268	M
4012	0.40	0.3	0.12	10	0.023	2.36	3.56	10	280	M
Experimental										
110516	0.300	0.3	0.061	8.1	0.021	2.04	2.06	-	339	W
060516	0.300	0.3	0.086	7.2	0.024	2.35	3.42	-	348	M
290416	0.301	0.3	0.111	9.0	0.023	2.11	3.20	-	428	S
260416	0.355	0.3	0.085	9.5	0.018	2.10	2.78	-	410	M
020516	0.356	0.3	0.110	9.5	0.022	2.13	3.13	-	456	M
090516	0.400	0.3	0.096	10.4	0.021	2.07	2.78	-	497	W
040516	0.400	0.3	0.140	10.4	0.022	2.26	3.46	-	555	M

5.3 Numerical Simulations

5.3.1 Wave-hill interaction

Here we present two-dimensional numerical simulations of a solitary mode-2 internal wave interacting with a narrow topography. We investigate the adjustment of the mode-2 ISW due to the hill, the vorticity generation within the boundary layer, and the resulting particle resuspension.

The wave speed is modulated through the non-linear dependence on wave amplitude. By increasing the amplitude, and therefore the wave speed, the flow changed from negligible interaction, to moderate vorticity roll-up, until finally exhibiting strong vortex generation at large amplitude.

When the interaction is weak, the wave passed over the hill mostly unchanged. The wave speed and amplitude were perturbed by approximately one to two percent of their pre-interaction values. However, these changes were on the order of the losses due to the natural deceleration and core leakage associated with large amplitude mode-2 waves. The local surface stress along the bottom boundary increased from the pre-hill value because of the increase in flow speed due to the shrinking layer depth. Not only was the shear strong enough to induce weak separation, but it was sufficient to create a persistent yet weak, $\mathcal{O}\left(0.5\ \mathrm{s}^{-1}\right)$, vorticity field above the hill.

In a moderate wave-hill interaction a small amount of fluid was removed from the lower half of the mode-2 wave which caused slight density over-turning to occur (Figure 5.3a and c). This small overturn was associated with the generation of vorticity lines within the pycnocline (Figure 5.3d and f), which continues to impact the BBL because of the close proximity to the hill crest. The obstruction of the mode-2 wave also led to boundary layer separation along the hill and the roll-up of a single vortex (Figure 5.3d and f) . As a result of this vortex, some fluid was pulled from the pycnocline into the boundary layer. This boundary layer separation occurs after the wave has passed the crest of the hill in a process similar to the vorticity roll-up discussed in Harnanan et al. [2015] and Olsthoorn and Stastna [2014]. The vorticity roll-up remains atop the hill well after the wave has passed. Thus, the instabilities produced by one wave may interact with a subsequent ISW resulting in amplified resuspension and dispersal of BBL material. This interaction is seen when the next rank-ordered mode-2 ISW reaches the hill (Figure 5.4).

The moderate interaction is characterized by minimal mixing in the pycnocline coupled with delayed vorticity roll-up near the peak of the hill. This indicates that while there is but a small perturbation to the wave, significant vorticity is still produced at the bottom

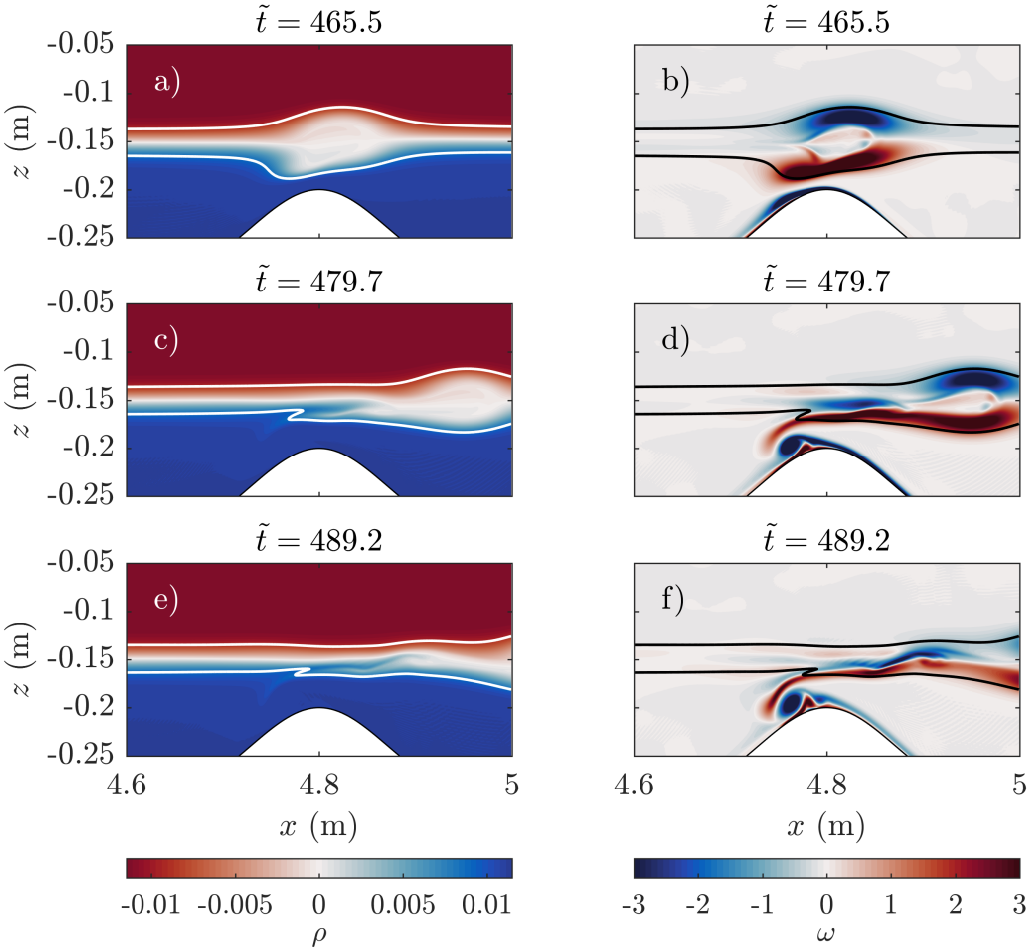

Figure 5.3: Density anomaly (a,c,e) and vorticity (b,d,f) for a moderate interaction (case 3008). White (black) contours in left (right) column are the characteristics isopycnals.

boundary which is capable of transporting material into the water column. The majority of the vortex roll-up forms while the wave is on the lee side of the hill, and remains long after the wave has passed

The moderate vorticity roll-up interaction also exhibited the creation of a small amplitude ($a = \mathcal{O}(1\text{ cm})$) mode-1 wavetrain behind the mode-2 ISW; the initial formation of which is partly seen in Figure 5.3e. The sudden reduction in fluid depth caused the ISW to be deflected vertically, causing a break in symmetry across the pycnocline. Since the ridge was quite narrow, the mode-2 ISW soon returned to an equilibrium depth and

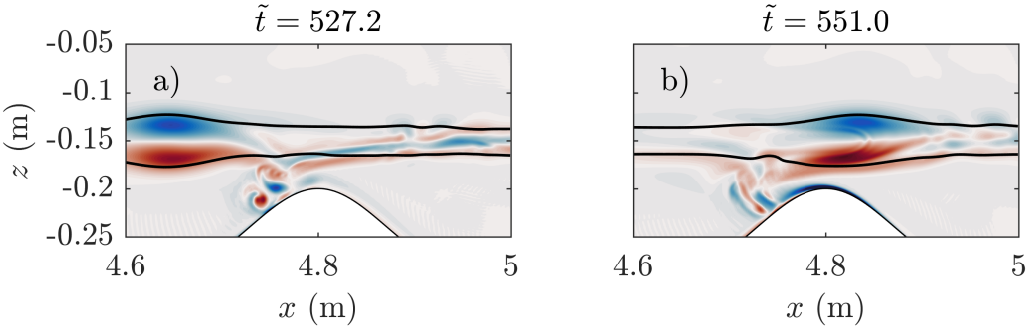

Figure 5.4: Vorticity of the second mode-2 ISW for moderate interaction (case 3008). Color scale is the same as the right column of Figure 5.3.

re-stabilized. The wavetrain, however, was not phase locked with the mode-2 ISW and eventually dispersed behind the wave. The vertical deflection also created a long mode-1 ISW to travel in front of the mode-2 ISW.

Despite the large size of the hill, the wave still remained coherent throughout the entire transit over the topography. The criterion for wave breaking will be discussed below, but it is clear that a large amplitude wave may travel largely unmodulated even with drastic topography. Case 4010 is a prime example as the wave amplitude in this case is quite large, but only modest vorticity roll-up is observed.

The strong wave-hill interaction occurred when the wave amplitude was large enough to cause core material to nearly impact the crest of the hill. Unlike the moderate interaction, an unmistakable filament of fluid was extracted from the mode-2 wave by the blocking of the hill (Figure 5.5c). It is this defining feature that was used to distinguish between moderate and strong interactions. This strong density over-turning quickly equilibrated (Figure 5.5e) while causing a sudden increase in viscous dissipation and mixing along the pycnocline.

The formation of the filament led to the formation of a large vortex (Figure 5.5d) which travelled nearly perpendicularly away from the hill. This vortex was quite energetic and moved from within the boundary layer into the pycnocline. It is expressly clear that in interactions of this type, fluid from the boundary layer and pycnocline are easily mixed. Therefore, this process may be efficient at lifting and dispersing boundary layer material into the water column.

The filamentary extraction realized in this large amplitude case has been described

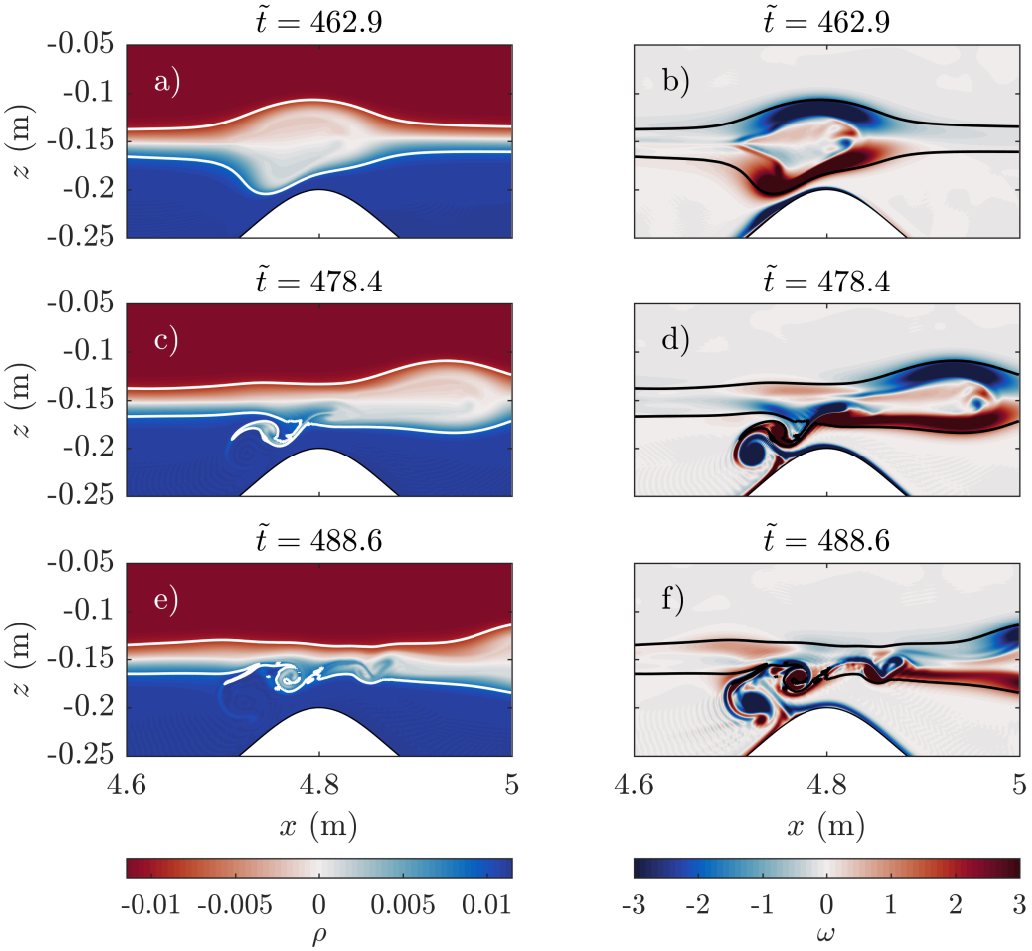

Figure 5.5: Density anomaly (a,c,e) and vorticity (b,d,f) for the strong interaction (case 3010). All other contours are the same as in Figure 5.3.

before in the case of a mode-1 ISW when traveling over a step [Maderich et al., 2010] and over a ridge [Sveen et al., 2002]. Though the waves were mode-1, the density fields appear quite similar (see Figure 15c from Maderich et al. [2010] and Figure 7c from Sveen et al. [2002]). Looking back at Figure 5.5, it is clear that the upper portion of the mode-2 ISW was essentially unaffected by the interaction with the bottom topography. All the kinetic energy induced by the interaction is isolated in the lower layer. This indicates that the dynamics of the interaction are independent of the wave mode number.

A trailing mode-1 wavetrain was again generated by the interaction with the hill in

the strong interaction cases. This wavetrain, however, was weaker than that formed in the moderate interaction because the mixing in the pycnocline caused a decrease of the amplitude. As in the moderate interaction type, the mode-2 ISW was deflected vertically causing the generation of a single long mode-1 ISW to travel in front of the mode-2 ISW. The mode-2 ISW was also noticeably smaller after the interaction because of the loss of core material - approximately 24% based on the product of the amplitude and wavelengths, $a(\lambda_a + \lambda_f)$, which is an over-estimate.

For the large size of the topography, the wave is not modified as much as one might expect in any of the cases. Due to the large asymmetry in layer depth it was expected that the mode-2 wave would deform enough to begin radiating large mode-1 waves. While some waves mode-1 are radiated, their amplitudes are small, $\mathcal{O}(1\text{ cm})$ at the largest. Aside from the strong wave-hill interactions, the wave amplitude, wavelength and speed of the transmitted mode-2 wave are all comparable to their values prior to interacting with the hill. Case 3012, a strong interaction, had the amplitude, wavelength and wave speed reduced by approximately 18, 14, and 5%, respectively. The interaction time is short, $\mathcal{O}(1\text{ s})$, such that the work done on the wave by the hill is minimal. Comparisons to wave-hill interaction in the case of a broad hill with a longer interaction time will be made in a follow-up article.

5.3.2 Tracer resuspension due to vorticity generation

A standard diagnostic used to measure the likelihood of particle resuspension is the surface stress. The surface stress along the hill was calculated from the stress vector, $f_i = \tau_{ij} n_j$ [Kundu et al., 2012], where τ_{ij} is the Cauchy stress tensor and n_j is the unit normal to the surface of the hill. For two dimensional simulations, the component tangential to the surface can be explicitly written as

$$f_s(x) = \frac{\mu}{1 + h'(x)^2} \left(2h'(x) \left(w_z - u_x \right) + \left(1 - h'(x)^2 \right) \left(u_z + w_x \right) \right),$$

where subscripts on the right hand side denote differentiation with respect to the given variable. The total tangential surface stress,

$$f_{\text{tot}} = \int_0^{L_x} |f_s(x)| \sqrt{1 + h'(x)} dx,$$

indicates the overall strength of the wave-hill interaction.

The surface stress for fluid depth of 30 cm (Figure 5.6) clearly indicates that the wave-hill interaction occured at $\widetilde{t} \approx 465$. Comparing Figures 5.3 and 5.5 to Figure 5.6 it is

clear that the maximal surface stress is associated with the obstruction of core material. In the strong interaction case (Figure 5.5a, c) the maximum stress occurs just prior to the formation of the filament.

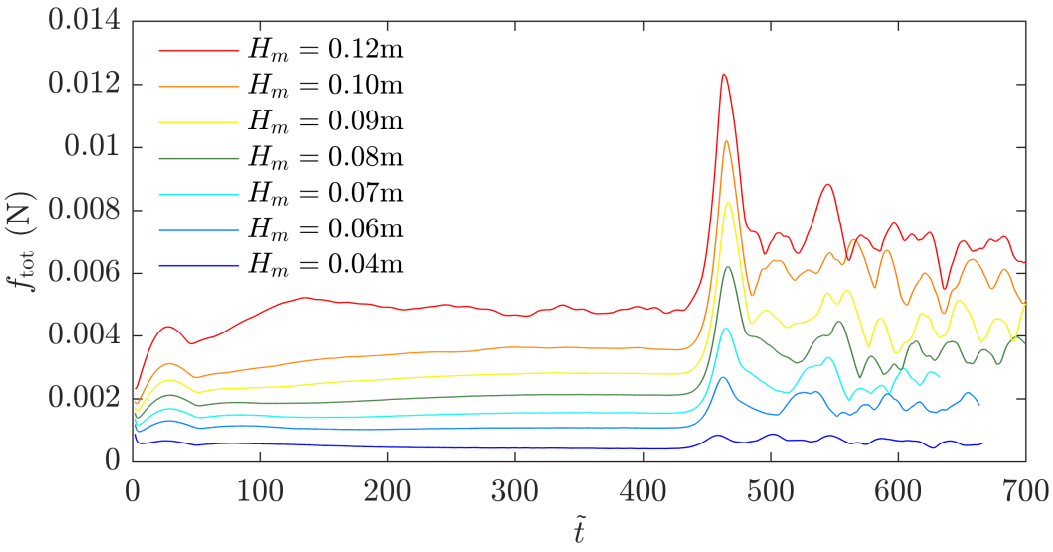

Figure 5.6: Total bottom surface stress with fluid depth, $L_z = 0.30$ m.

Prior to the wave-hill interaction, the surface stress is relatively constant once the wave had formed and become stable. In all cases the surface stress at least doubled from the pre-interaction value, while a couple cases ($H_m = 0.08$ m and $H_m = 0.09$ m) nearly reached triple the pre-interaction stress. After the interaction, the stress remains above the pre-interaction value due to the prevalence of the vorticity and mixing above the hill. Some cases show the interaction of the second rank-ordered mode-2 wave at approximately $\widetilde{t} = 540$.

As fluid depth increased, the required amplitude for separation increased due to a reduction in bottom surface stress. On an oceanic scale this indicates that resuspension occurs when the wave is large or the pycnocline is close to the hill crest. Proper quantification of this is done in section 5.5.

Further investigation of the role of surface stress and vorticity was done with the addition of a passive tracer localized to within one centimetre above the bottom topography. So far, it has already been seen that vorticity is easily produced on the upstream side of the hill, and that sufficient surface stress exists to cause separation.

In the moderate and strong interaction cases, vorticity produced on the upstream side of the hill acted to lift part of the tracer away from the hill (Figure 5.7). The majority of the tracer movement was confined within the vortex on the side of the hill on which the wave originates. In the moderate interaction (left column of Figure 5.7) the vorticity

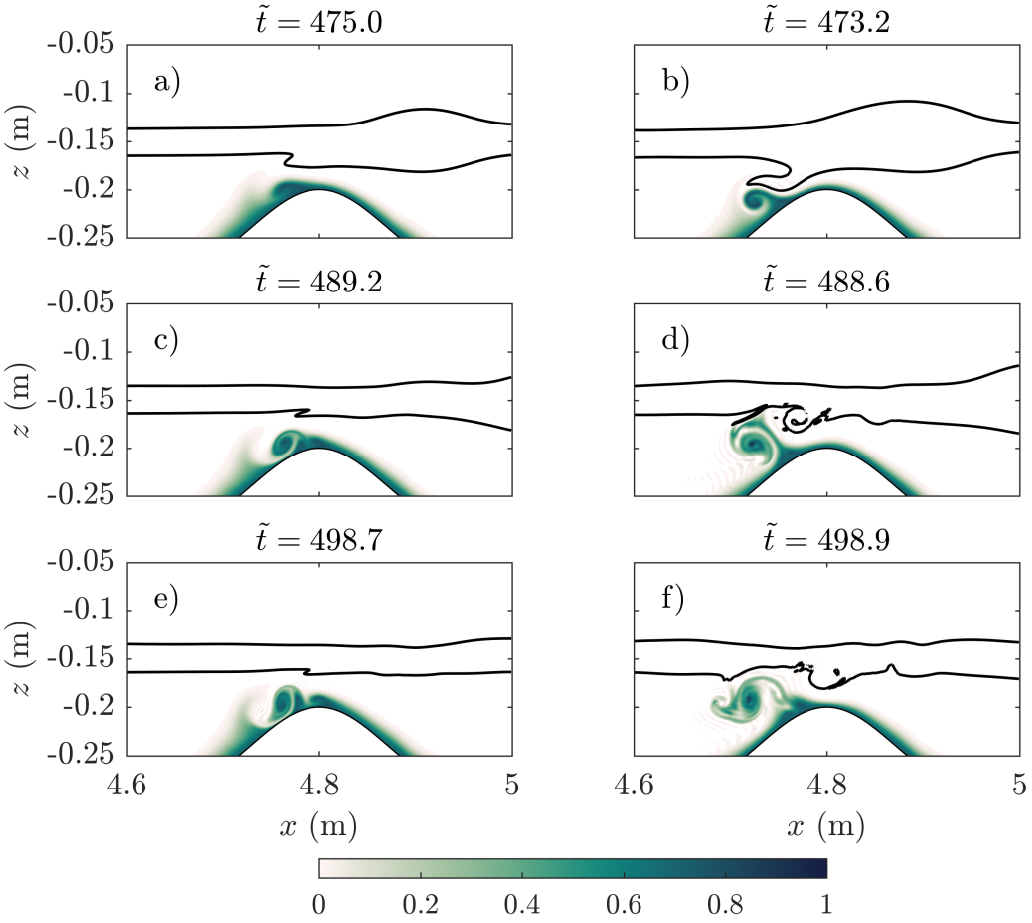

Figure 5.7: Passive tracer for (a,c,e) moderate (case 3008) and (b,d,f) strong (case 3010) interaction.

remained coherent and persisted long enough to move the tracer away from the bottom surface. The strong interaction was energetic and quickly moved material from the BBL to the edge of the pycnocline (Figure 5.7d). In both interactions, it is the coherent vortex which was the primary driver for transport of the tracer. The strength of the vortex is

weaker in the moderate interaction, and therefore the resuspension is considerably slower. In the strong interaction case, the vortex was unable to penetrate the pycnocline causing all the resuspended material to remain within the lower layer.

In either interaction case, the resuspended tracer remained suspended long after the interaction of the initial mode-2 ISW with the hill (Figure 5.8). At $\widetilde{t} \approx 710$, the first four rank ordered mode-2 ISWs have all travelled over the hill. The resuspended tracer from each interaction has been advected away from the hill in the direction opposite to that of the wave. Should there be fixed mode-2 generation sites (as proposed by Ramp et al. [2015] for the Heng-Chun ridge) then particulates will be preferentially directed towards those generation sites.

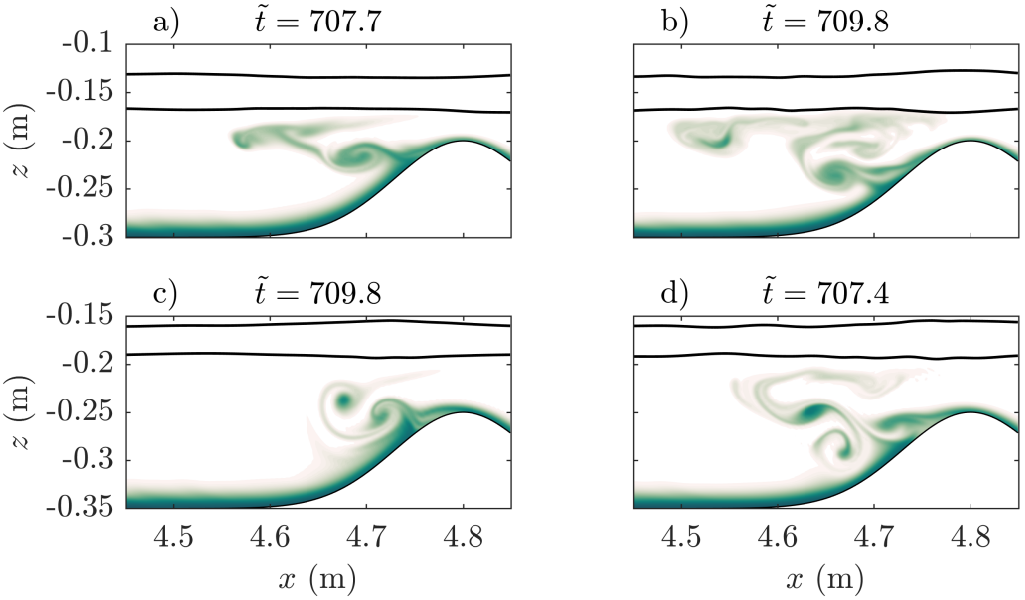

Figure 5.8: Passive tracer well after the transit of the mode-2 ISW for case a) 3008 and b) 3010 c) 3510 d) 3512. Moderate (strong) interaction corresponds to the left (right) column. The colorbar is the same as Figure 5.7.

Figure 5.8 reveals that within a given time-frame, stronger wave-hill interactions (right column) resuspend more BBL material and disperse those particulates over a wider area than for a moderate interaction (left column). Less BBL material was resuspended at an increased fluid depth (second row) due to the weaker surface stress. In any case, the ease to which bottom boundary layer material is resuspended is clear and should not be neglected.

In future work, a tracer with a settling velocity should be employed, but we have been concerned with the resuspension capabilities of the wave-hill interaction, and the neutrally buoyant tracer is ideal for this purpose.

Breaking waves were easily distinguished by the extraction of core material from the mode-2 ISW. They are an interesting dynamical effect which rapidly resuspends BBL material by means of vorticity generation at the hill crest. The moderate interactions experienced a calmer vorticity roll-up which still moved substantial BBL material. Therefore, mode-2 waves are an efficient means of both moving BBL material along the topography and resuspending particulates.

5.3.3 Reynolds number influence

Rather than looking at the tracer resuspension for different wave amplitudes and fluid depths, we now investigate the impact of changing Schmidt number and Reynolds number on a specific case. Numerical simulations are a particularly useful tool for this type of study, compared to laboratory experiments. Since case 3010 most clearly shows the filamentary extraction (Figure 5.5) and the quickest response to the interaction with the hill, it is this case that we will focus on.

Case 3010 was restarted just prior to interacting with the hill ($\widetilde{t} = 452.6$). In each new restart, either the density diffusivity, the viscosity, or both were halved or doubled. This created a parameter sweep where either the Reynolds number was held fixed while the Schmidt number varied, the converse, or where both varied.

Figure 5.9 shows the tracer for varying Reynolds number and a fixed value of $\mathrm{Sc} = 1$. This parameter sweep was chosen for presentation as it had the most variation in the tracer field. In contrast, a varying Schmidt number with fixed Reynolds number had no noticeable impact on the observed distribution of the tracer. The density field (contours in Figure 5.9) was found to be comparable for all Reynolds numbers used. The tracer field shows similar dynamical behaviour in each case; chiefly, the formation of a vortex which acts to resuspend the tracer. However, the visible details within that vortex structure increase with increasing Reynolds number. As we are primarily focused on the resuspension efficiency of the wave-hill interaction, it is evident that the Reynolds number does not have a primary role in this for the range reported. It should be noted that the Reynolds number for mode-2 wave shoaling in the field [Shroyer et al., 2010] is expected to be $\mathcal{O}(10^5)$, and hence it is possible that finer scale structure, or even secondary instabilities could be observed.

5.4 Comparison to laboratory experiments

5.4.1 Laboratory set-up, procedure, and measurement technique

Laboratory experiments were conducted using geometry matching that of the numerical simulations. The tank was 6.4 m long (L_x), 0.4 m wide (L_y), 0.6 m high (L_z), and contained a removeable gate located at $x = 0.30$ m.

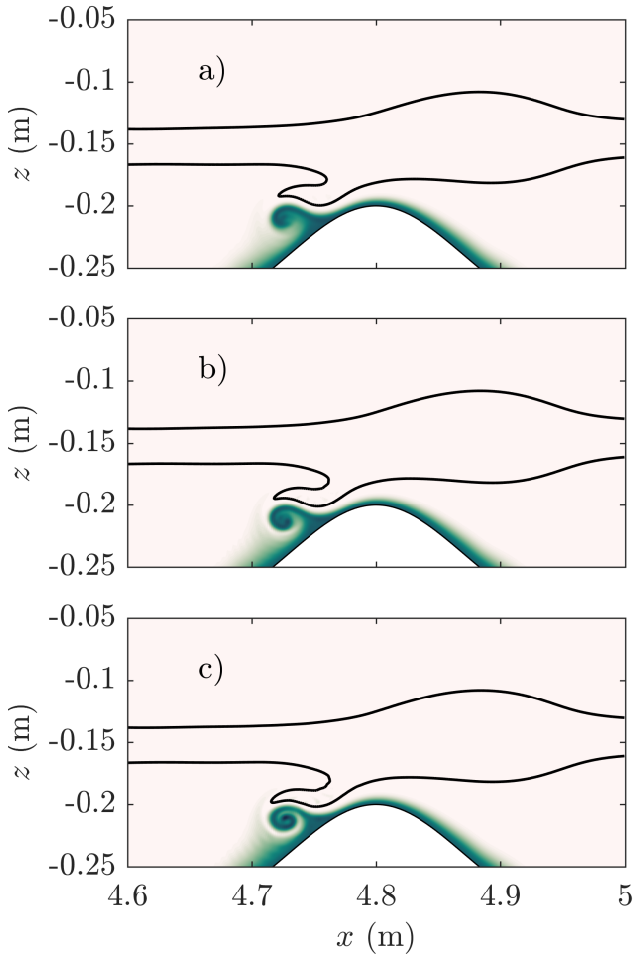

Figure 5.9: Passive tracer for strong interaction (case 3010) at $\widetilde{t} = 473.2$ with a) Re = 129, b) Re = 257, and c) Re = 514. The colorbar is the same as Figure 5.7.

The stratification was formed by slowly dripping a layer of less dense fluid on top of a more dense layer through an array of sponges. The two layers were both composed of miscible homogeneous brine solution, with the bottom and top layers having typical densities of $\rho_3 = 1047 \pm 2$ kg/m^3 and $\rho_1 = 1025 \pm 2$ kg/m^3, respectively. As a result of the miscibility of salt, the two layers diffused to form a continuous stratification that closely approximates a hyperbolic tangent profile.

After the lower layer in the main section of the tank had been filled, the gate was installed and fully closed. The main section of the tank was then stratified and at the same time, fluid of density ρ_3 was added behind the gate to maintain equilibrium pressure between the two sides of the gate. After the stratification was formed in the main section of the tank, a small valve located on the bottom of the channel was used to drop the fluid behind the gate. The fluid was dropped by an amount equal to the depth required for the wave-generating volume of mixed fluid, of density $\rho_2 = (\rho_1 + \rho_3)/2$. The mixed fluid was added using a floating sponge and a top layer of density ρ_1 was subsequently added through the same sponge. The fluid behind the gate was lowered and filled until the top and bottom layers behind the gate contained equal volumes. The resulting stratification then resembled that of Figure 5.1 with the addition of the gate a distance of L_m away from the left (upstream) wall.

The form of the stratification was measured using high precision, micro-conductivity sensors [Davies, 1992] connected to a rigid rack and pinion traverse system fitted with a potentiometer. Measurements of the position and conductivity of the sensors were made and converted into units of density by calibrating with the known upper and lower layer densities. The sensors were used to ensure that the mid-depth of the mixed layer behind the gate coincided with the mid-depth of the pycnocline in the main section of the tank.

Upon removal of the gate, the motion of the resultant mode-2 ISW was captured on three digital video cameras that were set up outside of the tank. The cameras were centered, in the vertical direction, on the pycnocline in order to minimize distortion and perspective errors in this portion of the flow field. The middle camera was centered, in the horizontal direction, on the apex of the topography. The cameras were arranged to have overlapping fields of view and were synchronized in time. Neutrally-buoyant, light-reflecting tracer particles of diameter $100 - 300$ μm, were used to seed the water column. An array of light boxes placed below the transparent base of the tank generated a continuous, narrow, collimated light sheet which illuminated a vertical section in the mid-plane of the tank. The motion of the tracer particles within the light sheet were viewed and recorded from the side by the three cameras. A rigid lid was placed on top of the water column to aid comparison with the numerical simulations.

The software package *DigiFlow* [Dalziel et al., 2007] was used to process the digital video records. The time series function of *DigiFlow* was used to measure wave speed and wave velocity while the Particle Image Velocimetry (PIV) function was used to calculate continuous synoptic velocity and vorticity field data along the illuminated cross-section in the middle of the tank. Further details on these techniques can be found in Carr et al. [2015].

5.4.2 Vorticity roll-up of the moderate interaction

As in the discussion of the numerical simulations, we begin with the moderate interaction case. Three experimental cases contain the vortex roll-up characteristic of this interaction (Table 5.3), of which two have a small amount of fluid removed from the edge of the wave core as a result of vorticity created along the lower crest of the wave.

The traversal of the wave over the hill created a large, slow vortex located just above and upstream of the hill peak. The vortex then moved towards the hill peak where separation occurred because of the favourable change in topography. Figure 5.10a shows the separation 7.8 non-dimensional time unites (1.5 s) after onset. 6.5 non-dimensional time units (1.25 s) later the separation has continued and particles from the boundary layer were advected vertically into the water column (Figure 5.10b).

As in the simulations, the vertically advected boundary layer material was carried up to the pycnocline and remained suspended well beyond the passage of the secondary mode-2 ISW.

5.4.3 Strong interaction extraction types

Thus far the interesting wave-hill interactions have been described as either moderate or strong. However, the laboratory experiments demonstrated another state that was a combination of the two. This interaction experienced strong vorticity in the lower aft of the wave, but did not result in a thin filament as in the strong interactions. For clarity, we will call the interaction that forms a filament a filamentary extraction (FE), while the interaction with similar vorticity but no filament will be called a globular extraction (GE). For the purpose of categorizing the GE interaction, it is listed as a moderate interaction because of the lack of a filament.

Figure 5.11 compares these two interaction types. The left column shows the globular extraction, while the right shows the filamentary extraction. Both types of interactions

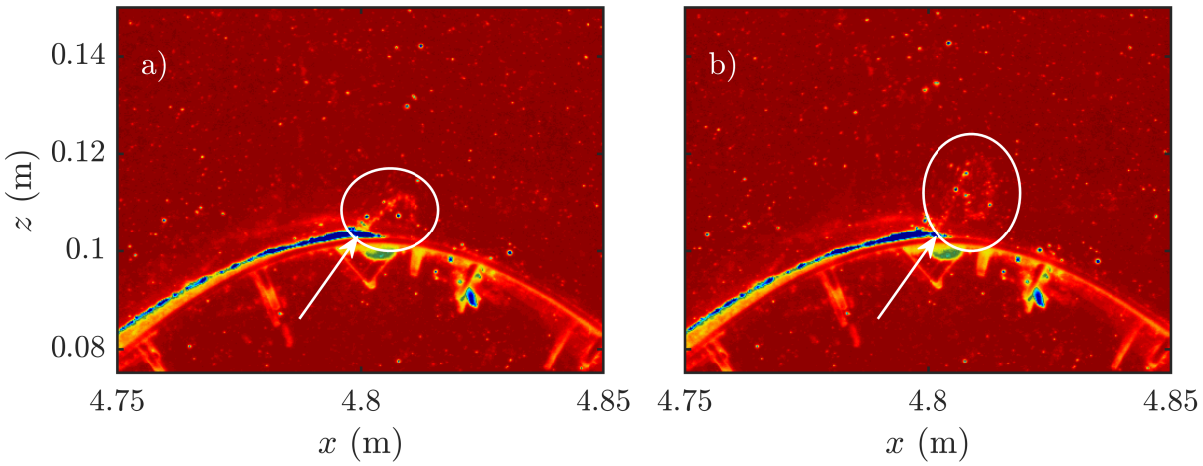

Figure 5.10: Experimental time series of vorticity roll-up (case 040516). a) 34.7 non-dimensional time units (6.7 s) after the wave crossed directly over the hill peak, b) 6.5 non-dimensional time units (1.25 s) after a). The circle emphasizes the resuspended particles, and the arrow points to the separation point.

exhibit a similar waveform when directly over the hill (Figure 5.11a and b), but have different extraction mechanisms. Six non-dimensional time units later the two waves show vastly different behaviour. The FE interaction displays a long, thin 'finger' of material emanating from the wave core (Figure 5.11d), while the GE interaction shows a large vortex of core material in contact with the pycnocline (Figure 5.11c). The GE and FE interactions caused comparable levels of mixing in the pycnocline. In the lower layer, induced vorticity and mixing was also comparable but covered different areas (Figure 5.11e and 5.11f).

The filamentary and globular extraction types are very similar. Filamentary extraction simply had the required energy to pull core fluid deep enough to form the filament. Since the wave speeds were similar between the two cases we surmise that the additional energy for the filamentary extraction came from the larger ISW amplitude. The larger amplitude would force the return flow to exist within the narrower region between the wave and the hill, thereby increasing the shear.

The amount of turbulent mixing is similar whether the separation interaction is globular or filamentary (circled region of Figure 5.11e and 5.11f). Though the filamentary case has been forced into a far more unstable situation, the amount of mass is not as large as in the globular case. Instead, the globular case has more core fluid transported to lie below its equilibrium depth. This caused similar reductions in the lower layer depth which increased the surface shear along the hill.

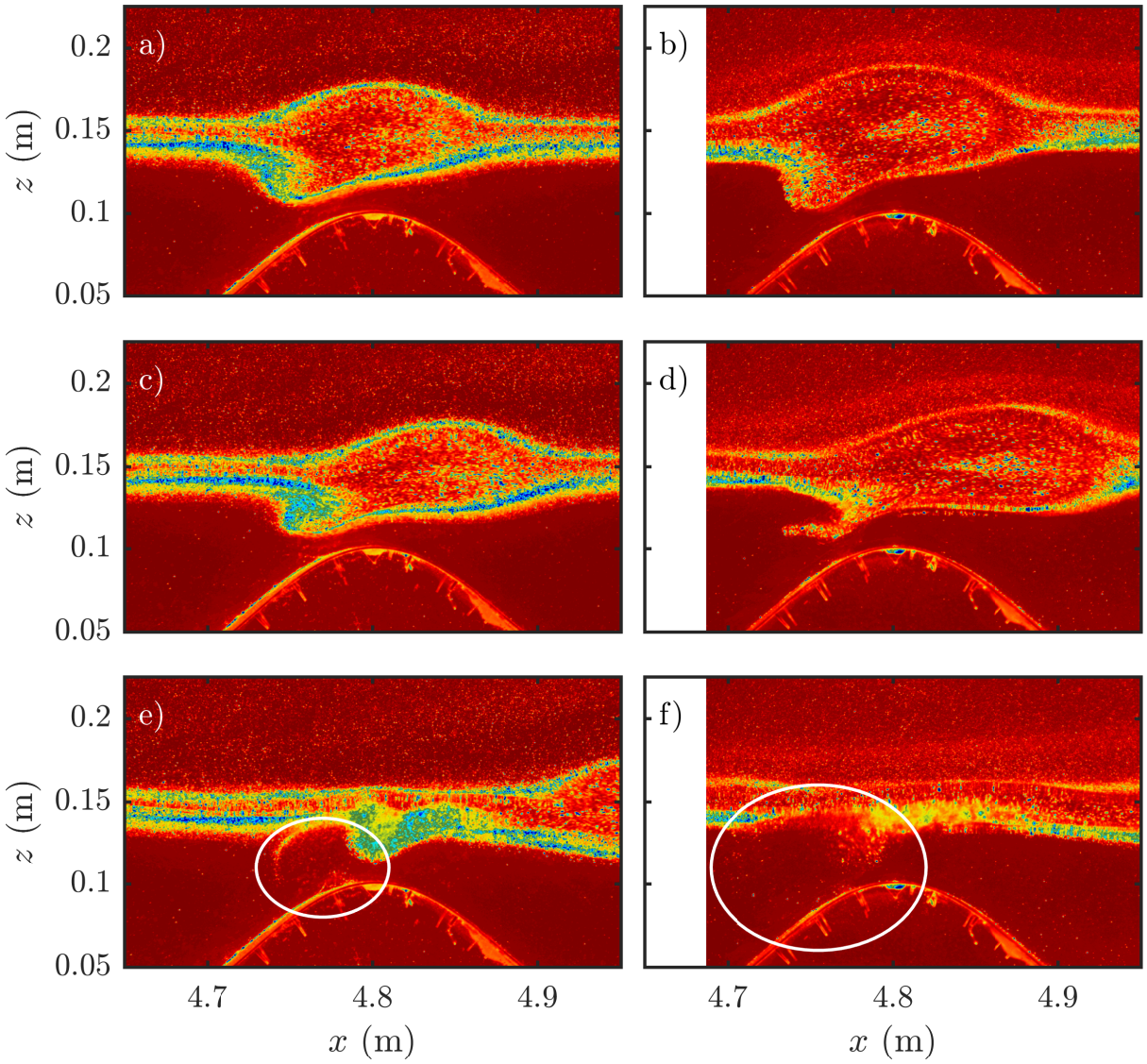

Figure 5.11: Experimental time series of the mass extraction of type: (a,c,e) globular extraction (Case 060516) and (b,d,f) filamentary extraction (Case 290416). (c,d) and (e,f) are 6 and 23 non-dimensional time units after (a,b), respectively.

The vorticity fields from the PIV measurements for the globular and filamentary extraction types are very similar (Figure 5.12) and match that from the filamentary extraction

type from simulations (Figure 5.5b). Vorticity calculations from PIV after the fluid has become three-dimensional are unreliable as particles are no longer moving predominantly in the x-z plane. As the flow becomes three dimensional, particles may pass through the illuminated plane making it nearly impossible to track a specific particle.

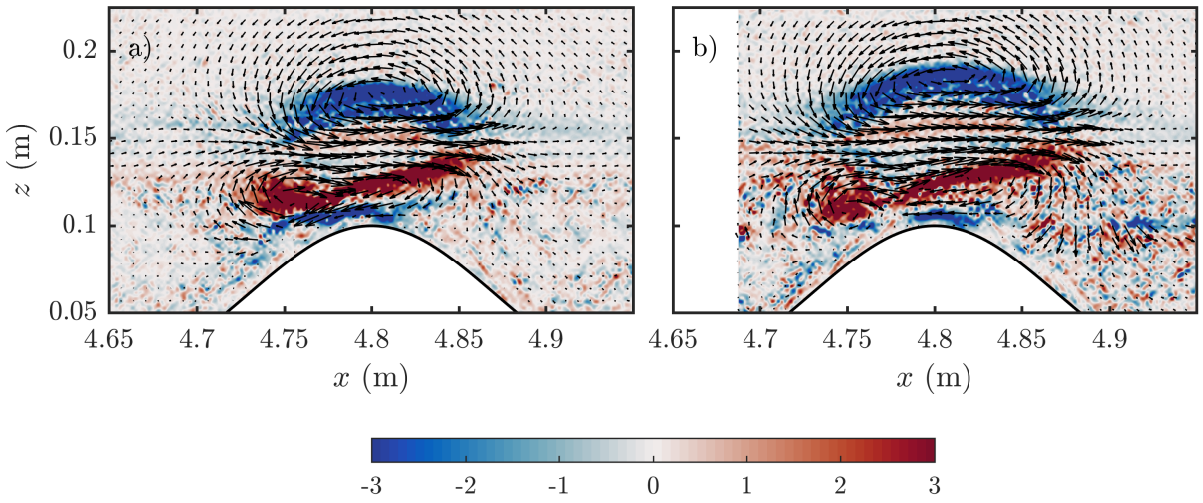

Figure 5.12: Vorticity and velocity vector field for (a,c,e) globular extraction (Case 060516) and (b,d,f) filamentary extraction (Case 290416) at the moment the wave is directly above the hill crest.

It should be mentioned that the globular extraction type was not explicitly seen within the numerical simulations. There are instances of removal of material from the core in a globular-like fashion, but these generally occurred in smaller quantities than those seen in Figure 5.11c. This difference can be attributed to the greater inherent chaotic behaviour of an experiment compared to a simulation (e.g. the effects of a surface that is free over a portion of the experimental flume, the effects of sidewalls, and artifacts associated with the lock release mechanism). In the simulations the conditions are always 'just right' for the filament to fully form, while for an experiment the formation may be delayed during the formation, allowing the structures associated with the ISW to move over the hill crest rather than forming the thin, dynamic filament on the upstream side of the topography crest.

In both the moderate and strong wave-hill interactions a long-wave mode-1 wavetrain was formed behind the mode-2 ISW. This matches the numerical simulations, but unlike the simulations, the experiments do not show the formation of a leading mode-1 ISW. This

is likely due to the leading wave having such a small amplitude that it wasn't perceptible from the PIV.

5.5 Wave breaking criteria

A criteria for wave breaking can be found from a new non-dimensionalized amplitude. The non-dimensionalization used above (scaling by the pycnocline half-width) is impractical since it contains no information on the size of the topography. The total depth could be used, but since the upper layer was essentially unaffected by the wave-hill interaction, it is the lower layer which entirely sets the behaviour of the wave-hill interaction.

The primary determining parameters for the interaction are the wave amplitude and hill height. The non-dimensional amplitude, a/ℓ, where $\ell = L_z/2 - d - A_{\text{hill}}$ is the depth of the lower layer at the hill crest, provides the proper scaling of the wave amplitude to minimum lower layer depth. Figure 5.13 shows the interaction types for given non-dimensional wave amplitude and wave speed. For $a/\ell < 1/3$ the wave-hill interaction is weak (W), while $a/\ell > 1/2$ manifests the strong FE interaction (S) which is a clear sign of wave breaking. For $1/3 < a/\ell < 1/2$ the interaction is moderate (M) and exhibits the vorticity roll-up interaction.

Two cases described as moderate interactions have $a/\ell > 0.5$. These cases are very nearly strong interactions as they showed the beginning formation of the filament being extracted from the ISW core. Nevertheless, because the filament was not clearly exhibited these cases were designated as moderate interactions. For these, and a few other cases, the categorization of the interactions was difficult. The demarcation lines of Figure 5.13 are somewhat arbitrarily chosen and are useful as a guideline rather than as a concrete rule.

The waves used herein are similar in amplitude but shorter in wavelength to those in Sveen et al. [2002]. The descriptions of the wave-hill interactions have also been quite similar. This, in addition to the upper layer being mostly unaffected by the wave-hill interaction indicates that the interaction is independent of mode number. The lower half of the mode-2 ISW (that which is below the pycnocline centre) is the effective region of influence. Since this region appears approximately as a mode-1 ISW of depression with an upper boundary at the pycnocline centre, the similarity between the different modes is unsurprising. The wave structure, particularly the wavelengths, are different between the modes so the interactions are not exactly comparable.

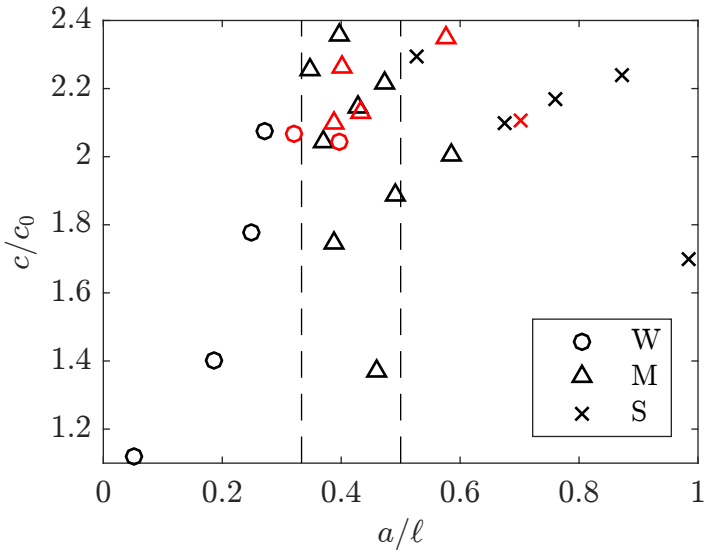

Figure 5.13: Non-dimensional wave speed versus non-dimensional amplitude. Black (red) markers correspond to simulations (experiments). The legend indicates the wave-hill interaction type. Vertical dashed lines are where $a/\ell = 1/3$ and $a/\ell = 1/2$.

5.6 Summary

We have conducted numerical and physical experiments of mode-2 ISWs traversing an isolated ridge. We have focused on a particularly narrow topography, while adjusting the size of the wave and the depth of the fluid. The wave amplitude compared to the pycnocline half-width were in the range 0.69-3.56, putting them in the highly non-linear regime. When compared to the minimum lower layer depth the amplitude was in the range 0.05-1.5; most cases where less than one.

We have found that the wave-hill interaction can be broken down into three regimes: weak, moderate, and strong interactions. The first occurs when the wave amplitude non-dimensionalized by the minimum lower layer depth, a/ℓ, is less than 1/3. The second, moderate interaction, occurs where the wave induces vorticity in the boundary layer of the hill, but is itself left largely unaffected. The third, when $a/\ell > 1/2$, has powerful vorticity generated at the hill crest and core material is extracted from the wave in the form of a thin filament of core fluid.

The moderate and strong interaction types resuspended BBL material. Rapid resuspension was coupled with a strong vortex formed during the filamentary extraction of core

fluid in the strong interaction case. Moderate interactions contained weaker, yet persistent vorticity which overtime pumped BBL material into the water column. It is hard to over-emphasize the ease in which vorticity is produced and it's role in resuspending material.

The greatest surface stress coincided with the generation of vorticity. In strong interactions this occurred just prior to the formation of the filament. The loss of core material in strong interactions led to a readjustment of the wave, while inducing mixing above the hill.

The wave-hill interaction was quick (approximately a second) in all cases. At most, the mode-2 ISW lost approximately 24% of core material in the formation of the filament. Although that interaction was strong, minimal generation of trailing mode-1 waves occurred. A long wavelength, short amplitude mode-1 wavetrain formed in both moderate and strong interactions. The numerical simulations showed the generation of a leading long mode-1 ISW that was not detected in the experiments because of the small amplitude.

While the primary mechanism for vortex generation in the strong breaking cases was the same for a variety of Reynolds numbers, the fine-scale structure increased with Reynolds number. Since observations of mode-2 ISWs typically have higher Reynolds numbers than those used here-within, the vortex generation and wave breaking might be more effective at inducing turbulent mixing.

With the clarity of resuspension associated with wave breaking in both mode-1 and mode-2 ISWs, it is now important that field scale observations be made to accurately measure the applicability of these idealized studies to a more dynamic and chaotic natural environment.

Numerically, future work could scale up the research into a larger environment more similar to that experienced by mode-2 waves in the Heng-Chun Ridge area [Ramp et al., 2015]. Some form of settling velocity or Shields criteria for resuspension would also add to the applicability of particle resuspension and distribution due to mode-2 ISWs.

Chapter 6

Conclusions

A variety of numerical and laboratory experiments have been conducted on the structure and stability of mode–2 internal solitary-like waves (ISWs). Three primary studies were conducted on mode-2 ISWs: mass transport, modification by rotation, and shoaling.

The first shows that mass transport is most efficient when a trapped (or nearly trapped) core exists. This in itself is not surprising, but the mechanism that degrades the trapped core is. Vorticity, of opposite sign to the baroclinic vorticity of the wave, which initially trails the wave impinges into the interior of the wave and supplants the low vorticity region associated with the trapped core. The precise origins of the impinging vorticity is still an open question, but it is hypothesized to be related to the generation mechanism of the mode-2 ISW (i.e. the lock release). The interior vortex structure causes what has become known as the 'Pac-Man' wave and is fairly common in numerical and experimental studies on mode-2 ISWs. The most efficient transport was found with a double pycnocline structure, with some stratification between the two main pycnoclines, which maintained the trapped core for the greatest duration. Lastly, the Schmidt number is positively correlated to the mass transport since the increased incidence of small scale structures acts to reduce the coherence of the interior vortex, and hence its ability to break up the core.

Mode-2 ISWs do not entrain fluid effectively. Though some fluid gets trapped by the wave, this fluid does not remain in the wave interior very long, as the wave core itself is not robust. The easiest way to break the wave core is to shift the location of the pycnocline away from the mid-depth. This breaks the symmetry of the mode-2 wave causing a radiation of energy into a trailing packet of mode-1 waves.

In a rotation-modified channel the mode-2 ISW is found to change into a leading internal Kelvin wave and trailing Poincaré waves. For a Northern-Hemisphere rotation we find that

mass and energy is advected towards the right-most wall which causes the wave amplitude to grow at this location and shrink elsewhere. Kelvin-Helmholtz billows result on the upper and lower edges of the deformed pycnocline within a narrow band near the focusing wall. With a fixed initial volume of fluid, the magnitude of the billows grows with increasing rotation rate. Three types of secondary waves form behind the leading Kelvin wave: the Poincaré waves, and two separate Kelvin waves, one of which forms from a resonance with the Poincaré waves while the other results from the remnants of the mixing caused by the Kelvin-Helmholtz billows.

A shoaling mode-2 ISW interacts with a submarine ridge in one of three ways: a weak, moderate, or strong interaction. The last of these dramatically removes fluid from the core of the mode-2 ISW while producing strong vorticity in the boundary layer. Both the moderate and strong interactions were seen to transport material out of the boundary layer. Experiments matched the results of the numerical simulations.

SPINS, the numerical model used throughout this work, has been improved by implementing the calculation of the full energy budget. While this has multiple physical applications, the primary benefit of this from a model construction point of view is the ability to directly measure the influence of the numerical filter. This subsequently informs decisions on grid refinement and de-refinement. The use of diagnostics is key in providing confidence in the accuracy of a numerical simulation.

Further work has been done to increase the functionality and ease of use of SPINS. These include safety writes when the simulation reaches the end of the allocated clock time in an HPC setting. Case files have been cleaned up so that repetitive, case independent sections of code have been removed. A case file was written for computing derivatives of primary variable fields and constructing secondary variable fields (vorticity, viscous dissipation, etc.), and the calculation of the surface stress is also now available.

6.1 Future work

A few clear avenues exist as future projects, some of which have simulations completed and just need analysis. This work showed that the interaction of a mode-2 ISW with a narrow isolated ridge has minimal impact on the wave, even with the loss of core fluid in the strong interaction case. However, the interaction of the ridge and wave will be more pronounced if the ridge is substantially wider. The longer interaction time will likely break the symmetry of the mode-2 wave across the pycnocline causing the creation of mode-1 ISWs with which the mode-2 wave can radiate energy into.

Though the studies reported in this thesis have focused solely on mode-2 internal solitary waves, much of what has been done can be applied to mode-1 ISWs. Much has already been done in the literature, especially with trapped cores and shoaling [Luzzatto-Fegiz and Helfrich, 2014, Lamb and Wilkie, 2004, Maderich et al., 2017], but the literature is more sparse when it comes to coastally trapped rotation modified mode-1 ISWs.

On the numerical methods side of things, the theory for Chebyshev refinement and derefinement has been presented but not yet implemented. This should be a simple enough project for most of it. The main difficulty will be in refinement along the grid-dependent dimension.

Should there be a desire for the challenge of complicated algebra, the calculation of the energy budget for salt-temperature stratifications could be completed. Specifically the rate of change of potential energy will require some care since the equation of state is nonlinear and depends on both heat and salt.

References

A. M. Abdilghanie and P. J. Diamessis. On the generation and evolution of numerically simulated large-amplitude internal gravity wave packets. *Theor. Comput. Fluid Dyn.*, 26(1-4):205–224, Feb 2011. ISSN 1432-2250. doi: 10.1007/s00162-011-0222-1.

N. A. Adams and S. Hickel. Implicit large-eddy simulation: Theory and application. In B. Eckhardt, editor, *Advances in Turbulence XII*, pages 743–750, Berlin, Heidelberg, 2009. Springer Berlin Heidelberg. ISBN 978-3-642-03085-7.

T. R. Akylas and R. H. J. Grimshaw. Solitary internal waves with oscillatory tails. *J. Fluid Mech.*, 242:279, Sep 1992. ISSN 1469-7645. doi: 10.1017/s0022112092002374.

G. K. Batchelor. Small-scale variation of convected quantities like temperature in turbulent fluid part 1. general discussion and the case of small conductivity. *Journal of Fluid Mechanics*, 5(01):113, Jan 1959. doi: 10.1017/s002211205900009x.

A. S. Belogortsev, S. A. Rybak, and A. N. Serebryanyi. Second-mode nonlinear internal waves over a sloping bottom. *Acoustical Physics*, 59(1):62–67, Jan 2013. doi: 10.1134/s1063771013010041.

T. B. Benjamin. Internal waves of permanent form in fluids of great depth. *J. Fluid Mech.*, 29(03):559–592, Sep 1967. ISSN 1469-7645. doi: 10.1017/s002211206700103x.

D. J. Bogucki, L. G. Redekopp, and J. Barth. Internal solitary waves in the coastal mixing and optics 1996 experiment: Multimodal structure and resuspension. *J. Geophys. Res.*, 110(C2), 2005. ISSN 2156-2202. doi: 10.1029/2003jc002253.

D. Bourgault, M. Morsilli, C. Richards, U. Neumeier, and D. Kelley. Sediment resuspension and nepheloid layers induced by long internal solitary waves shoaling orthogonally on uniform slopes. *Continental Shelf Research*, 72:21–33, Jan 2014. doi: 10.1016/j.csr.2013.10.019.

D. Bourgault, P. S. Galbraith, and C. Chavanne. Generation of internal solitary waves by frontally forced intrusions in geophysical flows. *Nature Communications*, 7:13606, 12 2016.

J. P. Boyd. *Chebyshev and Fourier Spectral Methods*. Dover Publications, Inc., 2nd edition, 2001.

A. Brandt and K. R. Shipley. Laboratory experiments on mass transport by large amplitude mode-2 internal solitary waves. *Physics of Fluids*, 26(4):046601, Apr 2014. doi: 10.1063/1.4869101.

D. Brydon, S. Sun, and R. Bleck. A new approximation of the equation of state for seawater, suitable for numerical ocean models. *Journal of Geophysical Research: Oceans*, 104(C1): 1537–1540, Jan 1999. doi: 10.1029/1998jc900059.

M. Carr, S. E. King, and D. G. Dritschel. Instability in internal solitary waves with trapped cores. *Physics of Fluids*, 24(1):016601, 2012. doi: 10.1063/1.3673612.

M. Carr, P. A. Davies, and R. P. Hoebers. Experiments on the structure and stability of mode-2 internal solitary-like waves propagating on an offset pycnocline. *Physics of Fluids*, 27(4):046602, Apr 2015. doi: 10.1063/1.4916881.

M.-H. Cheng, J. R.-C. Hsu, and C.-Y. Chen. Laboratory experiments on waveform inversion of an internal solitary wave over a slope-shelf. *Environmental Fluid Mechanics*, 11 (4):353–384, Jan 2011. doi: 10.1007/s10652-010-9204-x.

D. R. Corbett. Resuspension and estuarine nutrient cycling: insights from the Neuse River Estuary. *Biogeosciences*, 7(10):3289–3300, Oct 2010. doi: 10.5194/bg-7-3289-2010.

A. Coutino and M. Stastna. The fully nonlinear stratified geostrophic adjustment problem. *Nonlinear Processes in Geophysics*, 24(1):61, 2017. doi: 10.5194/npg-24-61-2017.

J. da Silva, A. New, and J. Magalhaes. On the structure and propagation of internal solitary waves generated at the Mascarene Plateau in the Indian Ocean. *Deep Sea Research Part I: Oceanographic Research Papers*, 58(3):229–240, Mar 2011. ISSN 0967-0637. doi: 10.1016/j.dsr.2010.12.003.

J. da Silva, M. Buijsman, and J. Magalhaes. Internal waves on the upstream side of a large sill of the Mascarene Ridge: a comprehensive view of their generation mechanisms and evolution. *Deep Sea Research Part I: Oceanographic Research Papers*, 99:87–104, May 2015. doi: 10.1016/j.dsr.2015.01.002.

S. B. Dalziel, M. Carr, J. K. Sveen, and P. A. Davies. Simultaneous synthetic schlieren and PIV measurements for internal solitary waves. *Measurement Science and Technology*, 18 (3):533, Jan 2007. doi: 10.1088/0957-0233/18/3/001.

P. A. Davidson. *Turbulence*. Oxford University Press, 1st edition, 2006.

P. A. Davies. Aspects of flow visualisation and density field monitoring of stratified flows. *Optics and Lasers in Engineering*, 16(4-5):311–335, Jan 1992. doi: 10.1016/0143-8166(92)90095-o.

R. E. Davis and A. Acrivos. Solitary internal waves in deep water. *J. Fluid Mech.*, 29(03): 593–607, Sep 1967. doi: 10.1017/s0022112067001041.

D. Deepwell and M. Stastna. Mass transport by mode-2 internal solitary-like waves. *Physics of Fluids*, 28(5):056606, May 2016. doi: 10.1063/1.4948544.

D. Deepwell, M. Stastna, M. Carr, and P. A. Davies. Interaction of a mode-2 internal solitary wave with narrow isolated topography. *Physics of Fluids*, 29(7):076601, Jul 2017. doi: 10.1063/1.4994590.

D. Deepwell, M. Stastna, and A. Coutino. Multi-scale phenomena of rotation-modified mode-2 internal waves. *Nonlinear Processes in Geophysics*, 25(1):217–231, Mar 2018. doi: 10.5194/npg-25-217-2018.

O. G. Derzho and R. Grimshaw. Solitary waves with a vortex core in a shallow layer of stratified fluid. *Physics of Fluids*, 9(11):3378, Nov 1997. doi: 10.1063/1.869450.

K. Dohan and B. Sutherland. Numerical and laboratory generation of internal waves from turbulence. *Dynamics of Atmospheres and Oceans*, 40(1-2):43–56, Jun 2005. ISSN 0377-0265. doi: 10.1016/j.dynatmoce.2004.10.004. Topics in Rotating and Stratified Fluids.

D. Dong, X. Yang, X. Li, and Z. Li. SAR observation of eddy-induced mode-2 internal solitary waves in the South China Sea. *IEEE Transactions on Geoscience and Remote Sensing*, 54(11):6674–6686, Nov 2016. doi: 10.1109/tgrs.2016.2587752.

D. Farmer, Q. Li, and J.-H. Park. Internal wave observations in the South China Sea: The role of rotation and non-linearity. *Atmosphere-Ocean*, 47(4):267–280, Dec 2009. doi: 10.3137/oc313.2009.

D. M. Farmer and J. D. Smith. Tidal interaction of stratified flow with a sill in Knight Inlet. *Deep Sea Research Part A. Oceanographic Research Papers*, 27(3-4):239–254, Apr 1980. ISSN 0198-0149. doi: 10.1016/0198-0149(80)90015-1.

A. V. Fedorov and W. K. Melville. Propagation and breaking of nonlinear Kelvin waves. *Journal of physical oceanography*, 25(11):2518–2531, 1995. doi: 10.1175/1520-0485(1995)025⟨2518:pabonk⟩2.0.co;2.

Global Ocean Associates. An atlas of internal solitary-like waves and their properties, 2004. URL http://www.internalwaveatlas.com/.

M. Gregg, E. D'Asaro, J. Riley, and E. Kunze. Mixing efficiency in the ocean. *Annual Review of Marine Science*, 10(1):443–473, Jan 2018. doi: 10.1146/annurev-marine-121916-063643.

R. Grimshaw. Evolution equations for weakly nonlinear, long internal waves in a rotating fluid. *Studies in Applied Mathematics*, 73(1):1–33, 1985. doi: 10.1002/sapm19857311.

R. H. J. Grimshaw, K. R. Helfrich, and E. R. Johnson. Experimental study of the effect of rotation on nonlinear internal waves. *Physics of Fluids*, 25(5):056602, 2013. doi: 10.1063/1.4805092.

Y. Guo, J. K. Sveen, P. A. Davies, J. Grue, and P. Dong. Modelling the motion of an internal solitary wave over a bottom ridge in a stratified fluid. *Environmental Fluid Mechanics*, 4(4):415–441, Jan 2004. doi: 10.1007/s10652-005-0485-4.

S. Harnanan, N. Soontiens, and M. Stastna. Internal wave boundary layer interaction: A novel instability over broad topography. *Physics of Fluids*, 27(1):016605, Jan 2015. doi: 10.1063/1.4906299.

K. R. Helfrich and W. K. Melville. Long nonlinear internal waves. *Annual Review of Fluid Mechanics*, 38(1):395–425, Jan 2006. doi: 10.1146/annurev.fluid.38.050304.092129.

P. Hosegood and H. van Haren. Near-bed solibores over the continental slope in the Faeroe-Shetland Channel. *Deep Sea Research Part II: Topical Studies in Oceanography*, 51(25):2943–2971, 2004. ISSN 0967-0645. doi: 10.1016/j.dsr2.2004.09.016. Small and mesoscale processes and their impact on the large scale.

E. L. Hult, C. D. Troy, and J. R. Koseff. The breaking of interfacial waves at a submerged bathymetric ridge. *Journal of Fluid Mechanics*, 637:45, Sep 2009. doi: 10.1017/s0022112009008040.

E. L. Hult, C. D. Troy, and J. R. Koseff. The mixing efficiency of interfacial waves breaking at a ridge: 1. Overall mixing efficiency. *Journal of Geophysical Research*, 116(C2), Feb 2011a. doi: 10.1029/2010jc006485. C02003.

E. L. Hult, C. D. Troy, and J. R. Koseff. The mixing efficiency of interfacial waves breaking at a ridge: 2. Local mixing processes. *Journal of Geophysical Research*, 116(C2), Feb 2011b. doi: 10.1029/2010jc006488. C02004.

J. C. R. Hunt, A. A. Wray, and P. Moin. Eddies, streams, and convergence zones in turbulent flows. page 193, Dec 1988.

L. Iapichino, J. Adamek, W. Schmidt, and J. C. Niemeyer. Hydrodynamical adaptive mesh refinement simulations of turbulent flows I. substructure in a wind. *Monthly Notices of the Royal Astronomical Society*, 388(3):1079–1088, 2008. doi: 10.1111/j.1365-2966.2008.13137.x.

C. Katsis and T. R. Akylas. Solitary internal waves in a rotating channel: A numerical study. *Physics of Fluids*, 30(2):297–301, 1987. doi: 10.1063/1.866377.

J. M. Klymak and M. C. Gregg. Three-dimensional nature of flow near a sill. *Journal of Geophysical Research: Oceans*, 106(C10):22295–22311, Oct 2001. doi: 10.1029/2001jc000933.

A. N. Kolmogorov. The local structure of turbulence in incompressible viscous fluid for very large Reynolds numbers. *Proceedings of the Royal Society A: Mathematical, Physical and Engineering Sciences*, 434(1890):9–13, Jul 1941. doi: 10.1098/rspa.1991.0075.

K. Konyaev, K. Sabinin, and A. Serebryany. Large-amplitude internal waves at the Mascarene Ridge in the Indian Ocean. *Deep Sea Research Part I: Oceanographic Research Papers*, 42(11-12):2075–2091, Nov 1995. ISSN 0967-0637. doi: 10.1016/0967-0637(95)00067-4.

P. K. Kundu, I. M. Cohen, and D. R. Dowling. *Fluid Mechanics*. Academic Press, 5th edition, 2012.

A. C. Kuo and L. M. Polvani. Time-dependent fully nonlinear geostrophic adjustment. *Journal of Physical Oceanography*, 27(8):1614–1634, 1997. doi: 10.1175/1520-0485(1997)027⟨1614:tdfnga⟩2.0.co;2.

K. G. Lamb. A numerical investigation of solitary internal waves with trapped cores formed via shoaling. *Journal of Fluid Mechanics*, 451:109–144, Jan 2002. doi: 10.1017/s002211200100636x.

K. G. Lamb. On boundary-layer separation and internal wave generation at the Knight Inlet sill. *Proceedings of the Royal Society A: Mathematical, Physical and Engineering Sciences*, 460(2048):2305–2337, Aug 2004. doi: 10.1098/rspa.2003.1276.

K. G. Lamb. Internal wave breaking and dissipation mechanisms on the continental slope/shelf. *Annual Review of Fluid Mechanics*, 46:231–254, 2014. doi: 10.1146/annurev-fluid-011212-140701.

K. G. Lamb and K. P. Wilkie. Conjugate flows for waves with trapped cores. *Physics of Fluids*, 16(12):4685–4695, Dec 2004. doi: 10.1063/1.1811551.

K. G. Lamb and W. Xiao. Internal solitary waves shoaling onto a shelf: Comparisons of weakly-nonlinear and fully nonlinear models for hyperbolic-tangent stratifications. *Ocean Modelling*, 78:17–34, Jun 2014. doi: 10.1016/j.ocemod.2014.02.005.

R. Löhner. An adaptive finite element scheme for transient problems in CFD. *Computer Methods in Applied Mechanics and Engineering*, 61(3):323–338, Apr 1987. doi: 10.1016/0045-7825(87)90098-3.

R. Löhner. *Applied CFD Techniques: An Introduction based on Finite Element Methods*. John Wiley & Sons, 2nd edition, 2008.

P. Luzzatto-Fegiz and K. R. Helfrich. Laboratory experiments and simulations for solitary internal waves with trapped cores. *Journal of Fluid Mechanics*, 757:354–380, 10 2014. ISSN 1469-7645. doi: 10.1017/jfm.2014.501.

V. Maderich, T. Talipova, R. Grimshaw, K. Terletska, I. Brovchenko, E. Pelinovsky, and B. H. Choi. Interaction of a large amplitude interfacial solitary wave of depression with a bottom step. *Physics of Fluids*, 22(7):076602, Jul 2010. doi: 10.1063/1.3455984.

V. Maderich, K. T. Jung, K. Terletska, and K. O. Kim. Head-on collision of internal waves with trapped cores. *Nonlinear Processes in Geophysics*, 24(4):751–762, Dec 2017. doi: 10.5194/npg-24-751-2017.

J. M. Magalhaes and J. C. B. da Silva. Internal solitary waves in the Andaman Sea: New insights from SAR imagery. *Remote Sensing*, 10(6), 2018.

T. Maxworthy. On the formation of nonlinear internal waves from the gravitational collapse of mixed regions in two and three dimensions. *Journal of Fluid Mechanics*, 96:47–64, 1 1980. ISSN 1469-7645. doi: 10.1017/S0022112080002017.

T. Maxworthy. Experiments on solitary internal Kelvin waves. *Journal of Fluid Mechanics*, 129:365–383, 1983. doi: 10.1017/s0022112083000816.

A. P. Mehta, B. R. Sutherland, and P. J. Kyba. Interfacial gravity currents. II. Wave excitation. *Physics of Fluids*, 14(10):3558–3569, 2002. doi: http://dx.doi.org/10.1063/1.1503355.

G. Mertz and Y. Gratton. *Topographic Waves and Topographically Induced Motions in the St Lawrence Estuary*, pages 94–108. Springer-Verlag, 1990. ISBN 9781118663783. doi: 10.1007/978-1-4615-7534-4_5.

J. Olsthoorn and M. Stastna. Numerical investigation of internal wave-induced sediment motion: Resuspension versus entrainment. *Geophysical Research Letters*, 41(8):2876–2882, Apr 2014. doi: 10.1002/2014gl059826.

J. Olsthoorn, A. Baglaenko, and M. Stastna. Analysis of asymmetries in propagating mode-2 waves. *Nonlinear Processes in Geophysics*, 20(1):59–69, 2013. doi: 10.5194/npg-20-59-2013.

L. A. Ostrovsky and Y. A. Stepanyants. Do internal solitions exist in the ocean? *Reviews of Geophysics*, 27(3):293–310, 1989. ISSN 1944-9208. doi: 10.1029/RG027i003p00293.

S. B. Pope. *Turbulent Flows*. Cambridge University Press, 1st edition, 2000.

S. R. Ramp, Y. J. Yang, D. B. Reeder, and F. L. Bahr. Observations of a mode-2 nonlinear internal wave on the northern Heng-Chun Ridge south of Taiwan. *Journal of Geophysical Research: Oceans*, 117(C3), 2012. ISSN 2156-2202. doi: 10.1029/2011jc007662. C03043.

S. R. Ramp, Y. J. Yang, D. B. Reeder, M. C. Buijsman, and F. L. Bahr. The evolution of mode-2 nonlinear internal waves over the northern Heng-Chun Ridge south of Taiwan. *Nonlinear Processes in Geophysics Discussions*, 2(1):243–296, 2015. doi: 10.5194/npgd-2-243-2015.

D. P. Renouard, G. C. D'Hières, and X. Zhang. An experimental study of strongly nonlinear waves in a rotating system. *Journal of Fluid Mechanics*, 177:381–394, 1987. doi: 10.1017/s0022112087001009.

C. Richards, D. Bourgault, P. S. Galbraith, A. Hay, and D. E. Kelley. Measurements of shoaling internal waves and turbulence in an estuary. *Journal of Geophysical Research: Oceans*, 118(1):273–286, 2013.

M. Salloum, O. M. Knio, and A. Brandt. Numerical simulation of mass transport in internal solitary waves. *Physics of Fluids*, 24(1):016602, Jan 2012. doi: 10.1063/1.3676771.

J. C. Sánchez-Garrido and V. Vlasenko. Long-term evolution of strongly nonlinear internal solitary waves in a rotating channel. *Nonlinear Processes in Geophysics*, 16(5):587–598, 2009. doi: 10.5194/npg-16-587-2009.

N. P. Schmidt. *Generation, Propagation and Dissipation of Second Mode Internal Solitary Waves*. PhD thesis, University of Canterbury, 1998. URL http://hdl.handle.net/10092/7811.

A. Scotti and J. Pineda. Observation of very large and steep internal waves of elevation near the Massachusetts coast. *Geophysical Research Letters*, 31(22):L22307, 2004. ISSN 1944-8007. doi: 10.1029/2004gl021052.

E. L. Shroyer, J. N. Moum, and J. D. Nash. Mode 2 waves on the continental shelf: Ephemeral components of the nonlinear internal wavefield. *Journal of Geophysical Research*, 115(C7), Jul 2010. ISSN 2156-2202. doi: 10.1029/2009jc005605. C07001.

A. P. Stamp and M. Jacka. Deep-water internal solitary waves. *Journal of Fluid Mechanics*, 305(-1):347–371, Dec 1995. doi: 10.1017/s0022112095004654.

M. Stastna and K. G. Lamb. Sediment resuspension mechanisms associated with internal waves in coastal waters. *Journal of Geophysical Research: Oceans*, 113(C10), 2008. ISSN 2156-2202. doi: 10.1029/2007JC004711.

M. Stastna, J. Olsthoorn, A. Baglaenko, and A. Coutino. Strong mode-mode interactions in internal solitary-like waves. *Physics of Fluids*, 27(4):046604, Apr 2015. doi: 10.1063/1.4919115.

P. Stevick, L. Incze, S. Kraus, S. Rosen, N. Wolff, and A. Baukus. Trophic relationships and oceanography on and around a small offshore bank. *Marine Ecology Progress Series*, 363:15–28, Jul 2008. doi: 10.3354/meps07475.

C. J. Subich, K. G. Lamb, and M. Stastna. Simulation of the Navier-Stokes equations in three dimensions with a spectral collocation method. *Int. J. Num. Meth. Fluids*, 73(2):103–129, 2013. ISSN 1097-0363. doi: 10.1002/fld.3788.

B. R. Sutherland. Interfacial gravity currents. I. Mixing and entrainment. *Physics of Fluids*, 14(7):2244–2254, 2002. doi: http://dx.doi.org/10.1063/1.1483303.

J. K. Sveen, Y. Guo, P. A. Davies, and J. Grue. On the breaking of internal solitary waves at a ridge. *Journal of Fluid Mechanics*, 469:161–188, Oct 2002. doi: 10.1017/s0022112002001556.

T. Talipova, K. Terletska, V. Maderich, I. Brovchenko, K. T. Jung, E. Pelinovsky, and R. Grimshaw. Internal solitary wave transformation over a bottom step: Loss of energy. *Physics of Fluids*, 25(3):032110, Mar 2013. doi: 10.1063/1.4797455.

D. E. Terez and O. M. Knio. Numerical simulations of large-amplitude internal solitary waves. *Journal of Fluid Mechanics*, 362:53–82, 5 1998. ISSN 1469-7645. doi: 10.1017/S0022112098008799.

K. Terletska, K. T. Jung, T. Talipova, V. Maderich, I. Brovchenko, and R. Grimshaw. Internal breather-like wave generation by the second mode solitary wave interaction with a step. *Physics of Fluids*, 28(11):116602, Nov 2016. doi: 10.1063/1.4967203.

K. M. Thyng, C. A. Greene, R. D. Hetland, H. M. Zimmerle, and S. F. DiMarco. True colors of oceanography: Guidelines for effective and accurate colormap selection. *Oceanography*, 29(3):9–13, 2016. doi: 10.5670/oceanog.2016.66.

V. G. W. Tomasz Plewa, Timur Linde. *Adaptive Mesh Refinement - Theory and Applications*. Springer, 1st edition, 2005.

H. N. Ulloa, A. de la Fuente, and Y. Niño. An experimental study of the free evolution of rotating, nonlinear internal gravity waves in a two-layer stratified fluid. *Journal of Fluid Mechanics*, 742:308–339, 2014. doi: 10.1017/jfm.2014.10.

H. N. Ulloa, K. B. Winters, A. de la Fuente, and Y. Niño. Degeneration of internal kelvin waves in a continuous two-layer stratification. *Journal of Fluid Mechanics*, 777:68–96, Jul 2015. doi: 10.1017/jfm.2015.311.

K. B. Winters and J. J. Riley. Instability of internal waves near a critical level. *Dynamics of Atmospheres and Oceans*, 16(3):249 – 278, 1992. ISSN 0377-0265. doi: 10.1016/0377-0265(92)90009-I.

K. B. Winters, P. N. Lombard, J. J. Riley, and E. A. D'Asaro. Available potential energy and mixing in density-stratified fluids. *Journal of Fluid Mechanics*, 289(-1):115–128, Apr 1995. doi: 10.1017/s002211209500125x.

C. Xu. Numerical simulations of shoaling internal solitary waves of elevation. Master's thesis, 2015. URL http://hdl.handle.net/10012/9232.

Y. J. Yang, Y. C. Fang, T. Y. Tang, and S. R. Ramp. Convex and concave types of second baroclinic mode internal solitary waves. *Nonlinear Processes in Geophysics*, 17 (6):605–614, 2010. doi: 10.5194/npg-17-605-2010.

H. Zhu, L. Wang, E. Avital, H. Tang, and J. Williams. Numerical simulation of interaction between internal solitary waves and submerged ridges. *Applied Ocean Research*, 58: 118–134, Jun 2016. doi: 10.1016/j.apor.2016.03.017.

APPENDICES

Appendix A

SPINS scaling

A.1 Parallel efficiency

In 2014, a collection of simulations were run on the high-performance supercomputing cluster called Orca (www.sharcnet.ca) to see the efficiency of SPINS. A variety of case files have been used to run 2D, 3D, mapped, and unmapped configurations with an assortment of resolutions in each spatial component. The efficiency of an n processor job was calculated as

$$S_n = \frac{t_1}{nt_n} \tag{A.1}$$

where t_1 and t_n are the wall clock times for the serial and n processor jobs, respectively.

Figure A.1 plots the efficiency of all scaling tests. Black points and lines represent large (50% of 512^3, and 512^3) 3D simulations, blue are smaller 3D runs (9.4% of 512^3), red are for a mapped grid, green is for a 2D unmapped case, cyan are Christopher Subich's scaling analysis from Subich et al. [2013], and purple are from Ben Storer's 3D unmapped simulations. Jobs not listed as Subich or Storer were conducted by David. All jobs run on as few nodes as possible (ie. a 16 processor jobs and smaller will be on 1 node, and a 32 processor job will be on 2).

Most case files used grids with equispaced points, while the two mapped cases used Chebyshev grids. All non-mapped runs conducted by David were free-slip in all spatial dimensions. All of Storer's runs were doubly periodic in the horizontal and free-slip in the vertical. The boundary conditions used by Subich are unknown.

All unmapped, 3D jobs above 10% of 512^3 are plotted in figure A.2. It is clear that the best efficiency is Subich's original scaling analysis, but we are unaware of the reason

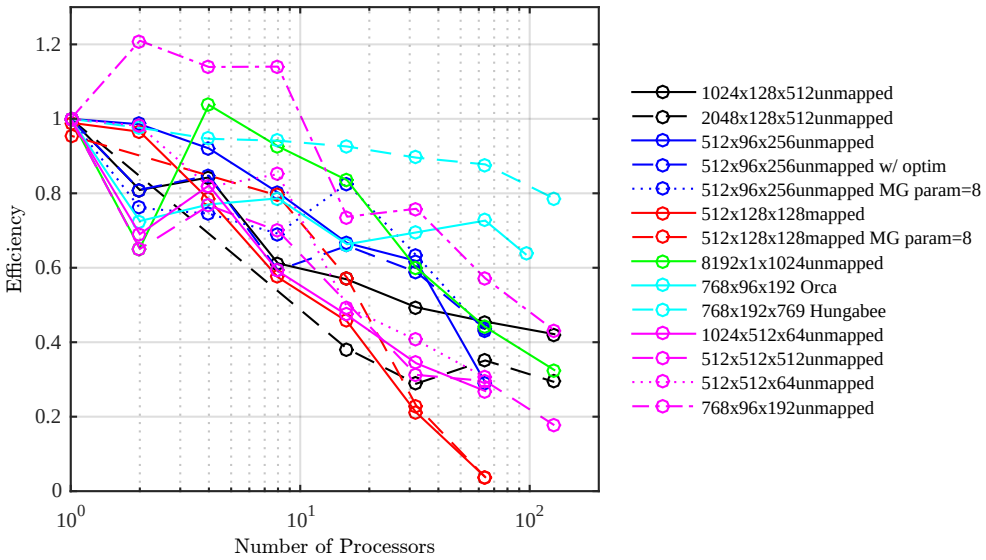

Figure A.1: Efficiency of parallel simulations.

for the discrepancy between his scaling and the rest of the cases. One of these cases ran on a different system than the rest and this could impact the comparisons made. Another possibility is that our scaling simulations have included the time for input/output (I/O) and do not accurately represent the computation time of each time-step. Initially the naive assumption was made that the I/O time is small, but as we will see below, this is not true for many of the cases used in this analysis (section A.4). This is due solely to the large number of writes and not the inefficiency of the write time. The two 512^3 jobs (dashed black and dashed purple) are similar in their efficiency at larger processors, having efficiency values around 30%.

Most of the other cases have similar trends to the 512^3 cases except for the $769\times96\times192$ case. This case has the odd behaviour where the 2, 4, and 8 processors are more efficient than the single processor and are more efficient than any other non-Subich case. This case was conducted with a different spins file from all the rest and may contain less computation, but this seems unlikely since all cases contain the computationally heavy components of SPINS. It is more likely that the difference is due to some hardware variability.

Smaller simulations (below 10% of 512^3) are plotted in figure A.3. The most inefficiently parallel simulations are the mapped cases in which the 32 processor jobs take longer clock time than with 16 processors. Changing the coarse grid size in the multigrid solver increased

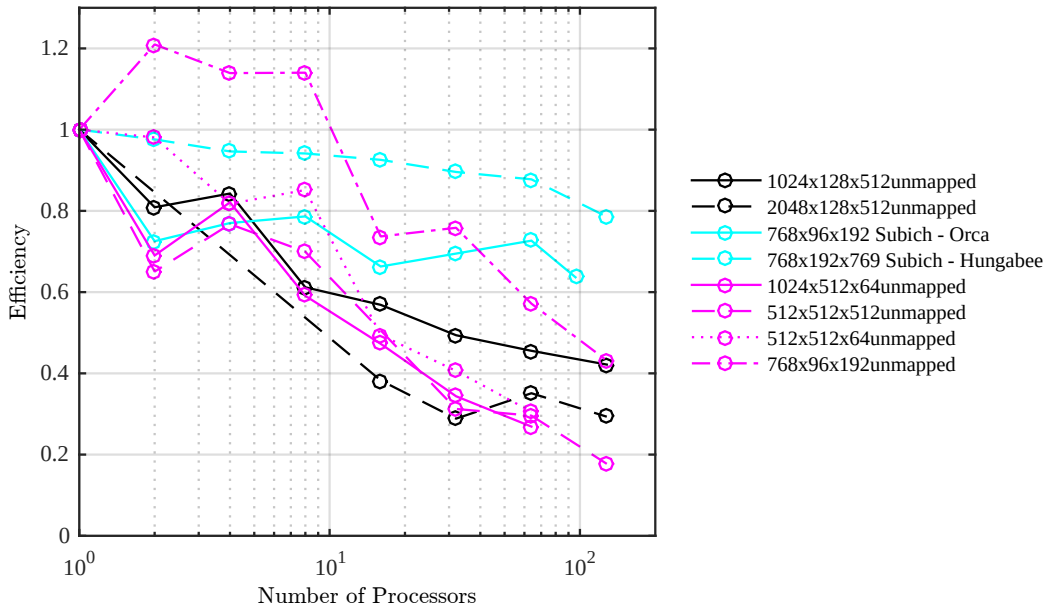

Figure A.2: Efficiency of large simulations (above 10% of 512^3).

the efficiency of the 4, 8, and 16 processor jobs, but had no impact above that. Rerunning an unmapped case (the dotted blue line is a repeat of solid blue) with this parameter change results in quite different efficiencies. This variance cannot be attributed to the multigrid parameter since it is not called in an unmapped situation. Rather it is likely due to the variance in the load on the HPC cluster. The interconnect between processors is dependent on the busyness of the file system and this is the likely culprit.

In the Makefile in SPINS there are two optimization flags available. The first is always set to true, while the other has it's default to false. The dashed blue line is the same as solid blue but with both optimizations utilized. For all but the 64 processor point, the single optimization case is more efficient than when both optimizations were used. Therefore, it appears as if this added optimization may only be advantageous at large processor numbers. The 2D (green line) has reasonable scaleability compared to the other jobs, but also drops below 40% at 128 processors.

As a conclusion to the current efficiency of SPINS, it is suggested that

- mapped grids should use at most **16** processors when the resolution is small. **32** can be used for resolution of $\frac{1}{8}512^3$ and greater

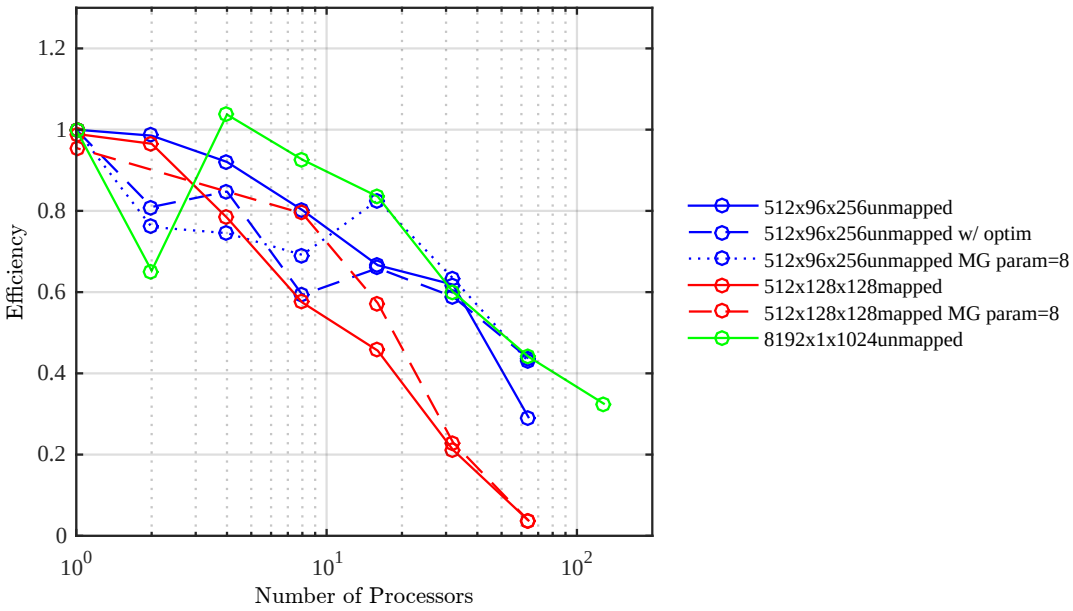

Figure A.3: Efficiency of small simulations (below 10% of 512^3).

- unmapped grids should use at most **32** processors for smaller cases, but may use more when the resolution warrants it. Resolution of 512^3 and greater can use **128** processors

A.2 CPU time

The cpu time per time-step (that is, clock time multiplied by the number of processors) for each series is plotted in figure A.4. All cases grow with the number of processors. The 2D simulation took the shortest time, but this is because of it's small size compared to the other 3D runs. The two 512^3 simulations took similar durations. The mapped cases have the worst growth and clearly show how inefficient they become.

These simulations also show the wide range in the duration of a typical time step due to the nature of the grid resolution. Scaling by the number of grid points collapses most of the lines into similar neighbourhoods (figure A.5). The only outliers are the unmapped cases and the simulations conducted by Subich. It is not surprising that the unmapped grid exhibit different temporal scales, but Subich's runs only add to their perplexity. The

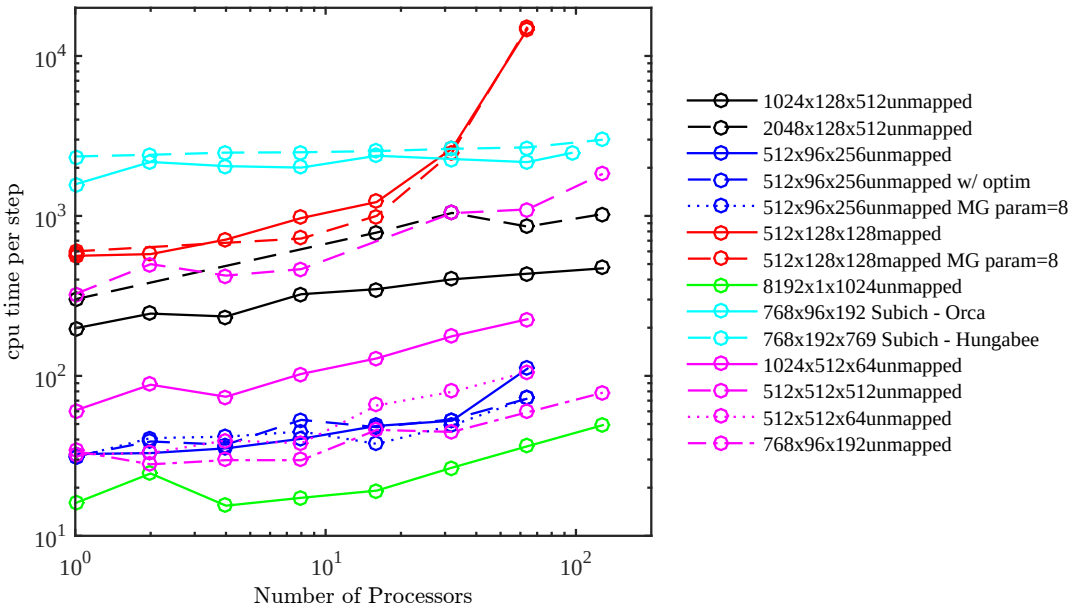

Figure A.4: CPU time per time step.

runs conducted by Subich are more efficient, and yet much slower than the other SPINS runs conducted separately.

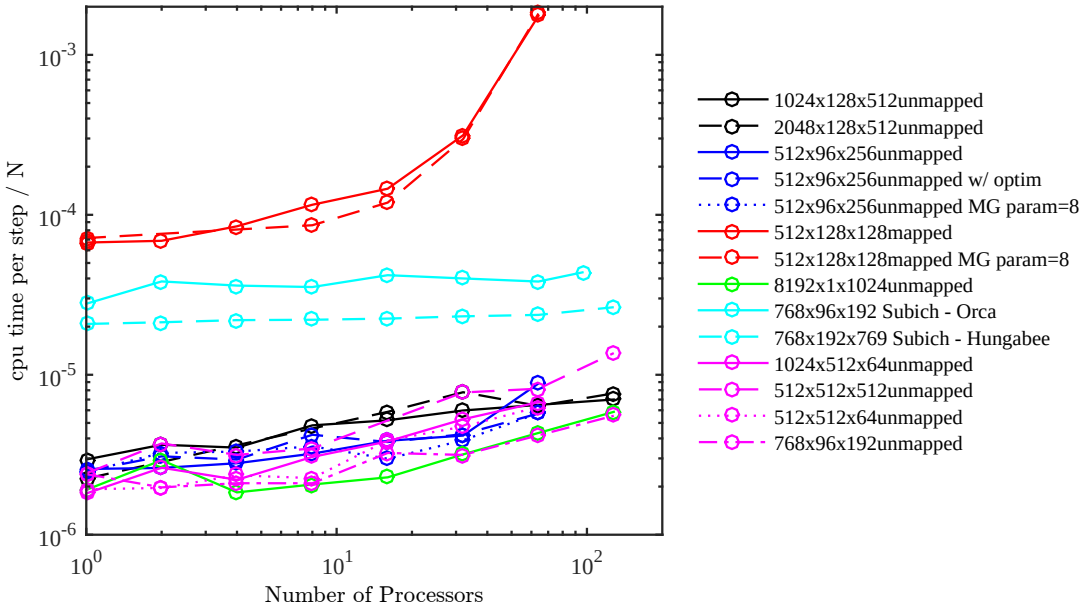

Figure A.5: CPU time per time step scaled by number of points.

A.3 Memory requirements

Running SPINS on any high performance computing cluster has two primary constraints: the number of processors and the memory. The first was discussed in the previous section, while the memory efficiency will be discussed here.

Figure A.6 displays the required memory for a collection of serial jobs with different grid resolutions. SPINS requires memory proportional to the grid size. The linear relationship has a slope of approximately 58 (no fitting was completed, just a rough eyeball of the general trend). 28 of the kglamb nodes on Sharcnet have 64 G of memory available for the 16 processors. 4 nodes are contain higher memory and have 128 G available. A serial 512^3 job will therefore take almost the entirety of the memory on one of the lower memory nodes.

One point, Storer's 512^3 case, is significantly off from this trend. No clear reason exists for this variation since the same case file was used for other resolutions which follow the above trend.

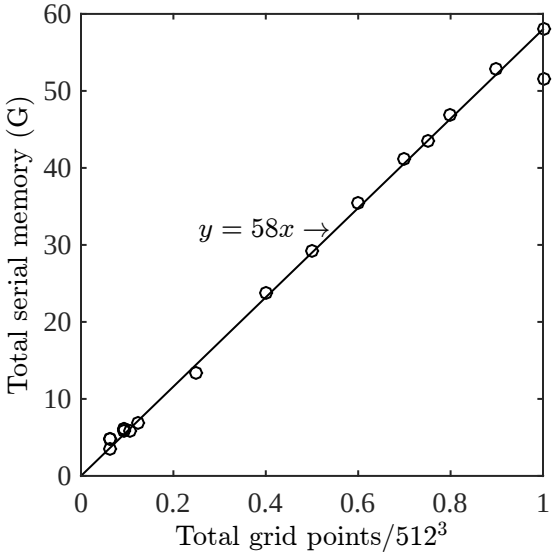

Figure A.6: Serial memory vs. total grid size. The memory grows linearly with the grid resolution.

The additional memory required for parallel jobs above 4 processors is roughly 0.3 G per additional processor (figure A.7). A few jobs deviate slightly from this trend: the two

black, large unmapped cases. This is likely due to the large number of points in a single (x) dimension, in conjunction with a large total number of points.

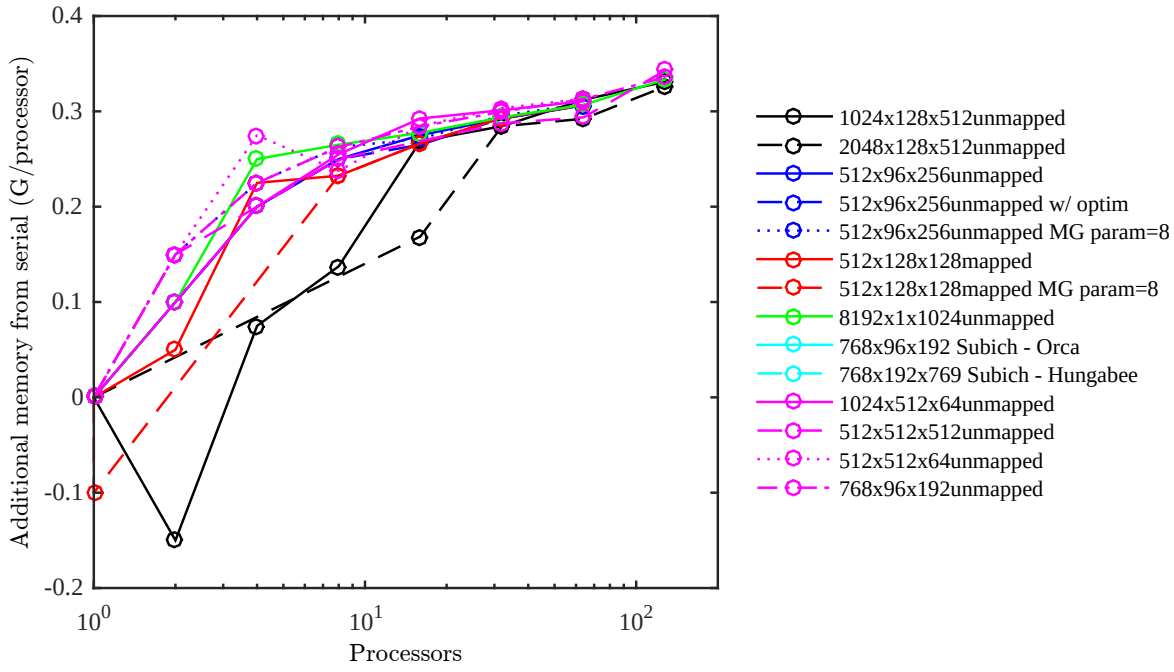

Figure A.7: Additional memory per processor.

Let M_p be the memory per processor, N_p be the number of processors, M_1 be the memory of serial jobs. Figure A.7 then shows that

$$\frac{M_p N_p - M_1}{N_p} \approx 0.3$$

for reasonably large number of processors. Using the serial memory from figure A.6, the memory per processor is

$$M_p \approx \frac{58\widetilde{N}}{N_p} + 0.3 \tag{A.2}$$

where $\widetilde{N} = N_x N_y N_z / 512^3$. This now allows simple calculations for the approximate memory needed for a job of a particular size an with a particular number of nodes.

Equation A.2 now allows us to find a way to efficiently use the memory available on each node. For large memory intensive jobs, there are two ways to get the required memory:

ask for many processors with low memory per processor, or the opposite, few processors with high memory per processor. The first uses the resources more efficiently since a jobs using 90% of memory and 10% of processors on a node leaves many processors unused. This was how our large serial jobs were completed. Fortunately, they did not need to be run for very long. To reiterate, this should never be done in practice!

Rather, the memory on a node should be evenly distributed between the processors. The kglamb nodes have either 64 G or 128 G of memory available. These are nominal values and the real memory will be slightly less. To calculate efficient memory sharing let M^* be the memory per processor accessible on a given system. We now need

$$M_p <= M^*$$

using equation A.2 we get

$$N_p >\approx \frac{58\widetilde{N}}{M^* - 0.3}$$

For the majority of the kglamb nodes ($M^* = 3.9$) this sets

$$N_p >\approx 16\widetilde{N}$$

For the high memory nodes ($M^* = 7.9$) this gives

$$N_p >\approx 7.5\widetilde{N}$$

These are only ballpark type values and should be used as a guide in calculating the minimum number of processors necessary to run a job without taking more memory than one should.

A.4 Efficiency without I/O

A few scaling cases were re-run with one second accuracy on individual time-steps. This enables the output write time and the initialization time to be calculated.

The unmapped $512 \times 96 \times 256$ job was resubmitted as the case with the multi-grid parameter changed to 8 (dotted blue line in previous figures). As previously stated, the multi-grid parameter should have no impact on the numerics. The I/O has a clear and drastic impact on the efficiency of this run (figure A.8). This however, is not showing that

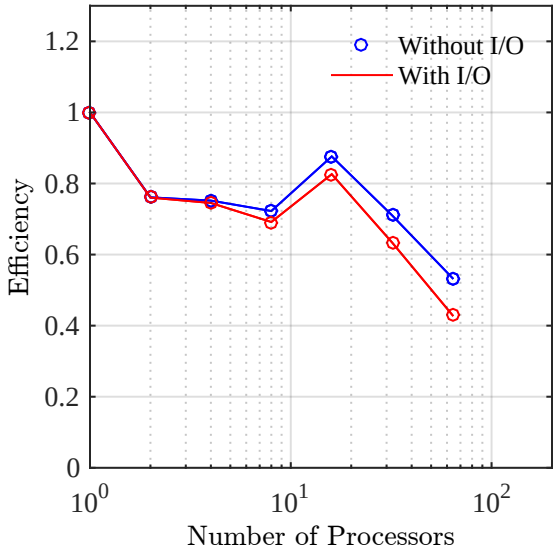

Figure A.8: Comparison of efficiency with and without I/O. Due to the large number of writes compared to total steps, the efficiency is better without I/O.

the I/O is inefficient in all cases, but only in this one where the number of writes was large compared to the total number of steps.

The average write time (over 8 writes) is much more reassuring (table A.1). For this grid size ($\approx 10\%512^3$) the output write time is approximately 4 s. Having looked at other simulations we are fairly confident that this is on the correct order of magnitude for most jobs. For example, a 0.25×512^3 job had a write time around 10 s.

Due to the extremely large time steps for the mapped grid case we were unable to distinguish a time-step containing a write from one that does not. We are thus very confident that the output time is not something to be worried about in SPINS at the current moment. One must only be careful if they want to save very frequently. This is a difficult thing to quantify prior to running the script because it is the number of writes to number of time-step between writes which is the important ratio and one cannot know a priori how many steps their simulation will take.

The start-up time was found to be quite small for this run (table A.1). This small time is mostly due to the fields being initialized within SPINS. The longest startup time is for the wave-reader case (which reads in the initial fields from disk), which takes between 10 and 13 minutes for a 0.25×512^3 run.

Table A.1: Input and output times for each processor size of an $\approx 10\%$ of 512^3 job.

Processors	Avg. write time (s)	Start-up time (s)
1	3.3482	80
2	3.2679	48
4	2.8909	31
8	2.6200	51
16	3.0098	12
32	3.0701	17
64	4.0065	18

:wq

git push